Politecnico di Torino

Master's Degree in Aerospace Engineering



Master's Degree Thesis

Development, Integration and Manufacturing of a Stratospheric Glider Prototype

Supervisor:

Prof. Angelo Lerro

Candidate:

Jacopo Sartori s326558

Thales Alenia Space Tutors :

Ing. Luca Simonini
Ing. Alberto Congedi

Academic Year 2025/2026

Abstract

Space Dart is a 70 cm wingspan remotely piloted glider developed within the SpArks Open Innovation initiative of Thales Alenia Space. The long-term objective is to deploy the glider from approximately 20 km altitude, carried by a stratospheric balloon, for future applications.

This thesis starts from a previously developed and aerodynamically optimized configuration of the vehicle. Building on this configuration, my work focused on developing the physical prototype, with particular attention to its CAD design, internal architecture and manufacturability.

This involved the CAD and mechanical redesign of the glider, together with the redesign of its internal architecture to integrate and reposition the existing avionics within the very limited internal space available. The structure was substantially reworked to accommodate these constraints, while the avionics themselves required only limited modifications, mainly related to component positioning and integration. The design was also adapted to the requirements of the manufacturing process, defining how the structure should be segmented into printable parts, addressing the limitations of FDM 3D printing, and selecting materials according to the structural and functional requirements of the different components.

Manufacturing and assembly of the final prototype were carried out as part of this work, resulting in a complete, flight-ready configuration.

To validate the theoretical dynamic behaviour predicted in previous analyses, a flight-test methodology is proposed.

The motorless glider would be carried to altitude by a second drone and released through a dedicated release mechanism, after which specific manoeuvres would be performed to excite the Phugoid and Dutch-roll modes. The resulting flight data would then be compared with the theoretical predictions to assess how closely the experimental dynamic behaviour agrees with the expected behaviour and, if needed, identify correction parameters to improve the theoretical model.

List of Tables

2.1 Main avionics components of the previous prototype. 7
2.2 Main geometric differences between the inherited V1 configuration and the final V1_4 aerodynamic configuration. 10
2.3 Main dynamic modes of the final V1_4 configuration at sea level. . . . 11
2.4 Selected aerodynamic and dynamic properties of V1_4 at 20 km altitude. 12

3.1 Location and main purpose of the parting planes in the final CAD configuration. 25
3.2 Comparison of the mass properties of the structure and the final integrated CAD configuration. 32

4.1 Bambu Lab PLA Basic vs Bambu Lab PLA Aero. 49

6.1 Proposed comparison between theoretical and experimental dynamic properties. 91

A.1 Geometric parameters of the inherited V1 configuration and the final V1_4 aerodynamic configuration. Bold values indicate parameters modified with respect to V1. 100

B.1 Additional slicer settings used for the wings 102
B.2 Main slicer settings used for the wings 103
B.3 Main slicer settings used for the fuselage top back 104
B.4 Main slicer settings used for the fuselage top front 105
B.5 Main slicer settings used for the fuselage bottom back 106
B.6 Main slicer settings used for the fuselage bottom left and right 107
B.7 Main slicer settings used for the elevons and rudder 108

List of Figures

2.1 Previous Space Dart prototype used as the physical starting configuration. 6
2.2 Previous avionics configuration of the Space Dart prototype. 7
2.3 Subdivision of the previous Space Dart prototype. 8
2.4 Subdivision of top panel and Pitot panel. 8
2.5 Final aerodynamic reference configuration V1_4. 9

3.1 Evolution of the elevon servo integration: (a) intermediate in-fuselage configuration; (b) final wing-mounted configuration. 15
3.2 Previous hinges' weak point. 15
3.3 Previous Pitot housing. 16
3.4 Intermediate configuration with the Pitot tube integrated inside the vertical fin. 17
3.5 Final Pitot configuration solution on the 3D printed model. 18
3.6 Final VTX Antenna configuration CAD view. 19
3.7 Final FCC support structure and CG position for reference. 21
3.8 Early avionics-layout iteration including the parachute system: (a) parachute and forward ballast masses; (b) parachute and servo arrangement. 22
3.9 Final Avionics Configuration inside the Glider. 24
3.10 Final subdivision of the Space Dart CAD model and adopted reference frame. 26
3.11 Top and Bottom Fuselage Division. 27
3.12 Top Fuselage Division. 28
3.13 Back Bottom Fuselage Division. 29
3.14 Wing and Fuselage Division. 30
3.15 Wing Division. 31
3.16 2D view of the aircraft with CG position. 34

4.1 Schematic representation of the main components of an FDM 3D printer. 36
4.2 Bambu Lab X1E 3D printer used for manufacturing the prototype. . . 39
4.3 Orientation of the parts inside the build plate 41
4.4 Support Map of the Top Back piece 42
4.5 Sliced Back Top piece 43

4.6 Sliced Front Top piece 44
4.7 Orientation of the parts inside the build plate 45
4.8 Support Map and Sliced plate of the Back Bottom piece 46
4.9 Support Map and Sliced plate of the Left/Right Bottom piece 46
4.10 Elevons and Rudder pieces 47
4.11 Sliced Build Plate of Moving Control Surfaces 48
4.12 Central wing section positioned on the build plate before printing. . . . 51
4.13 Wing tip positioned on the build plate before printing. 52
4.14 Sliced central wing showing the internal printing structure and gyroid infill. 53
4.15 Wing-tip connector removal 54
4.16 Insertion of hinges inside the post processed wing 55

5.1 Connection between the central wing section and the wing tip. 58
5.2 Connection between the wing and the lower fuselage section. 60
5.3 Final assembly of wing and fuselage connection. 60
5.4 Left and Right lower fuselage before bonding. 62
5.5 Rear bottom fuselage showing the two rear openings and screw connection. 63
5.6 Front/back top fuselage connection. 64
5.7 Top/bottom fuselage connection. 65
5.8 Elevons and Rudder hinges system 66
5.9 Mounted Elevons on Wings. 67
5.10 Elevons actuation system. 68
5.11 Rudder actuation system. 69
5.12 Elevated support for mounting the FCC highlighted in orange. 70
5.13 Battery cavity and its support highlighted in blue. 71
5.14 Pitot and AirSpeed assembled. 72
5.15 Camera downward angle. 73
5.16 VTX and its antenna mounted. 74
5.17 GNSS and ELRS CAD view. 75
5.18 Final Assembly of Avionics inside the Space Dart. 77
5.19 Space Dart prototype and its back-up shell. 78

6.1 Qualitative control input and expected response during the Phugoid manoeuvre. 84
6.2 Qualitative rudder doublet and expected coupled yaw–roll response. . . 86

Contents

Abstract i

List of Tables ii

List of Figures iii

1 Introduction 1

1.1 The SpArks Project . . . 1
1.2 Project Background and Previous Developments . . . 1
1.3 Starting Configuration . . . 2
1.4 Objectives and Scope of the Thesis . . . 3
1.5 Thesis Structure . . . 3

2 Project Background and Reference Configuration 5

2.1 Previous Prototype and Avionics Configuration . . . 5
2.2 Aerodynamic Reference Configuration . . . 9
2.2.1 Latest Aerodynamic Geometry . . . 9
2.2.2 Aerodynamic Properties . . . 10

3 CAD Redesign and System Integration 13

3.1 Redesign of the Avionics Configuration . . . 13
3.1.1 Servo Configuration . . . 14
3.1.2 Pitot Tube and AirSpeed System . . . 16
3.1.3 Video Transmission Antenna . . . 18
3.1.4 ELRS and Telemetry System . . . 19
3.1.5 Battery . . . 20
3.1.6 Flight Control Computer . . . 20
3.1.7 GNSS . . . 21
3.1.8 Camera . . . 21
3.2 Final Avionics Configuration . . . 23
3.3 Final Prototype Subdivision . . . 24
3.4 Prototype Subdivision Design Process . . . 26

3.5 Final Geometric and Mass Properties 32

4 Additive Manufacturing and Manufacturing Strategy 35
4.1 3D Printing Terminology, Process and Printer Overview 35
4.1.1 FDM/FFF Printing Process 36
4.1.2 Printer Components and Printing Parameters 37
4.1.3 Geometry-Related Printing Concepts 37
4.2 Printer and General Printing Strategy 38
4.3 Fuselage 40
4.3.1 Top Fuselage 40
4.3.1.1 Back top fuselage 41
4.3.1.2 Front top fuselage 43
4.3.2 Bottom Fuselage 44
4.3.2.1 Left and Right Bottom Fuselage 45
4.3.2.2 Back Bottom Fuselage 46
4.4 Moving Control Surfaces 46
4.5 Wings 48
4.5.1 Aero PLA: General Characteristics 48
4.5.2 Aero PLA printing strategy and iterations 50
4.6 Post-Processing of Printed Components 53

5 Prototype Assembly and Integration 57
5.1 Mechanical Assembly and Connection Strategy 57
5.1.1 Wing Assembly 58
5.1.2 Lower Fuselage Assembly 61
5.1.3 Upper Fuselage and Main Fuselage Closure 63
5.1.4 Control-Surface Installation and Linkages 65
5.2 Avionics Installation and Wiring 69
5.3 Final Prototype and Functional Checks 77

6 Proposed Flight-Test Methodology 79
6.1 Objectives of the Flight Tests 79
6.2 Flight-Test Setup and Procedure 80
6.3 Dynamic-Mode Excitation 82
6.4 Data Acquisition and Comparison 87
6.5 Limitations and Future Development 91

7 Conclusions and Future Developments 94
7.1 Main Results 94

7.2 Limitations of the Present Work 95
7.3 Future Developments 96

Bibliography **98**

A Appendix A: Geometry details **100**

B Appendix B: Slicer Settings **102**
B.1 Wings 102
B.2 Top Back Fuselage 104
B.3 Top Front Fuselage 105
B.4 Bottom Back Fuselage 106
B.5 Bottom Left/Right Fuselage 107
B.6 Moving Control Surfaces 108

Chapter 1

Introduction

1.1 The SpArks Project

The Space Dart project was developed within the SpArks initiative of Thales Alenia Space. SpArks is an internal Open Innovation venture created within the framework of the company's industrial accelerator, the Space Business Catalyst (SBC), an initiative aimed at supporting the development of new ideas, markets and applications related to the space sector. [1]

The objective of SpArks is to make technologies and knowledge coming from the space industry accessible to a wider audience. Within this framework, the concept of the *Playable Space Asset* (PSA) was introduced, referring to a platform that allows users on the ground to interact remotely with assets operating in unusual or space-related environments. The first activities of the project involved the use of stratospheric balloons, which provide access to the upper layers of the atmosphere without the complexity of an orbital mission.

As a further development of this concept, the possibility of using a remotely piloted flying vehicle was introduced. Such a vehicle could be transported to high altitude by a stratospheric balloon and then released, allowing users to interact with a controllable platform during its descent towards the ground. This idea led to the development of the Space Dart, a small motorless glider designed as an experimental platform for the project.

1.2 Project Background and Previous Developments

The development of the Space Dart was carried out progressively through different thesis activities, each one focusing on a different part of the project. The first complete development of the vehicle was carried out in the previous work by F.Ghinamo [2], where the initial aerodynamic configuration, onboard avionics and first physical prototype were defined. This work provided the first integrated version of the Space Dart and demonstrated the feasibility of producing the vehicle through additive manufacturing and integrating the required electronic components.

The following thesis work, carried out by M.Tesi [3], focused mainly on the aerodynamic development of the glider. Starting from the previous configuration, several

geometric modifications were introduced and evaluated through OpenVSP [4] and CFD analyses using STAR-CCM+ [5]. The objective was to improve the aerodynamic behaviour of the vehicle and obtain a configuration with suitable static and dynamic stability characteristics. This iterative process led to the final aerodynamic geometry used as the reference configuration for the present work.

The current thesis therefore represents the next step in the development of the Space Dart. While the aerodynamic configuration was already defined, the corresponding physical prototype still had to be redesigned and adapted to practical manufacturing and integration requirements. The work presented here starts from this final aerodynamic geometry and focuses on transforming it into a complete, manufacturable and flight-ready vehicle.

1.3 Starting Configuration

The starting point of this thesis is the final aerodynamic configuration obtained from the previous development activity. The external geometry had already been defined through aerodynamic analyses and CFD validation, and the main static and dynamic characteristics of the glider were therefore available before the beginning of the present work.

However, the optimized geometry did not directly correspond to a complete physical prototype. The change from the previous configuration affected the internal volume available for the avionics, the position of the control surfaces and the way in which the aircraft could be manufactured and assembled. For this reason, the existing CAD model could not simply be reproduced without further modifications.

The avionics architecture developed during the earlier stages of the project was largely retained, but the position and integration of several components had to be reconsidered. In particular, the arrangement of the servos, Pitot system, video equipment and other onboard devices had to be adapted to the new geometry and to the limited internal space of the vehicle.

The final aerodynamic geometry and the inherited avionics configuration represent the main inputs to the work presented in this thesis. A more detailed description of these elements, together with the relevant aerodynamic properties, is provided in Chapter 2.

1.4 Objectives and Scope of the Thesis

The main objective of this thesis is to transform the previously optimized aerodynamic configuration of the Space Dart into a complete and manufacturable prototype suitable for the following experimental development phase.

Starting from the available geometry and avionics, the work focuses on the practical development required to move from the theoretical configuration to a physical vehicle. The main objectives of the thesis are:

- redesign the CAD model to integrate the available avionics within the final aerodynamic geometry;
- reorganize the internal architecture and the control-surface actuation system according to the available space and assembly requirements;
- adapt the aircraft structure to the limitations and requirements of FDM additive manufacturing;
- define suitable materials and printing strategies for the different parts of the glider;
- manufacture, assemble and integrate the complete prototype;
- define a flight-test methodology for comparing the dynamic response of the manufactured glider with the theoretical predictions.

The work does not aim to repeat the aerodynamic optimization performed previously, nor to provide a complete structural qualification of the vehicle. The focus is instead placed on the practical design choices required to move from the theoretical configuration to a physical prototype and on the preparation of the following experimental phase.

The final outcome of the work is a complete and integrated Space Dart prototype that provides the basis for the following flight-test phase. Although the complete flight-test campaign could not be carried out within the time available for this thesis, a methodology for its first experimental evaluation is proposed and discussed.

1.5 Thesis Structure

The thesis is organized into seven chapters.

Chapter 2 introduces the previous Space Dart configuration and summarizes the final aerodynamic geometry and properties used as the starting point for the present work.

Chapter 3 describes the CAD redesign and system integration. The reorganization of the avionics, the control-surface actuation system, the subdivision of the aircraft into separate components and the final mass properties are presented.

Chapter 4 focuses on the additive manufacturing process used to produce the prototype. The selected materials, printing strategies and the main manufacturing difficulties encountered during the development are discussed.

Chapter 5 describes the assembly and integration of the manufactured components. Particular attention is given to the structural connections, control-surface installation, avionics mounting and final functional checks of the completed prototype.

Chapter 6 presents a proposed methodology for the first flight tests of the Space Dart. The test setup, release concept, manoeuvres for the excitation of the Phugoid and Dutch-roll modes, data acquisition and comparison with the theoretical predictions are discussed.

Finally, Chapter 7 summarizes the main results obtained during the thesis, discusses the main limitations of the work and presents possible future developments of the Space Dart project.

Chapter 2

Project Background and Reference Configuration

This chapter introduces the technical configuration from which the present work started. The previous physical prototype and its avionics architecture are first described, together with the main manufacturing and assembly choices adopted in the earlier development phase.

The final aerodynamic configuration obtained in the subsequent aerodynamic study is then presented as the reference geometry for the CAD redesign developed in this thesis. Only the main geometric changes and the aerodynamic and dynamic properties relevant to the present work are reported, while the detailed aerodynamic development and numerical methodology are available in the previous studies.

2.1 Previous Prototype and Avionics Configuration

The starting point for the present work was a previously developed physical prototype of Space Dart. This configuration included the main structural components, the complete avionics architecture, and the first manufacturing and assembly concept. The prototype was produced mainly in black carbon fiber reinforced PLA (PLA-CF), using additive manufacturing for the aircraft structure. The CAD project was produced using SOLIDWORKS software [6].

The prototype was not brought to a flight-ready configuration. In particular, the aerodynamic geometry still required further development before flight testing could be considered. The original configuration presented limitations in lateral stability and used relatively large control surfaces, which were subsequently modified during the aerodynamic redesign described in the following section. The detailed aerodynamic analysis of these limitations is not repeated here, since it belongs to the previous aerodynamic study. [3]

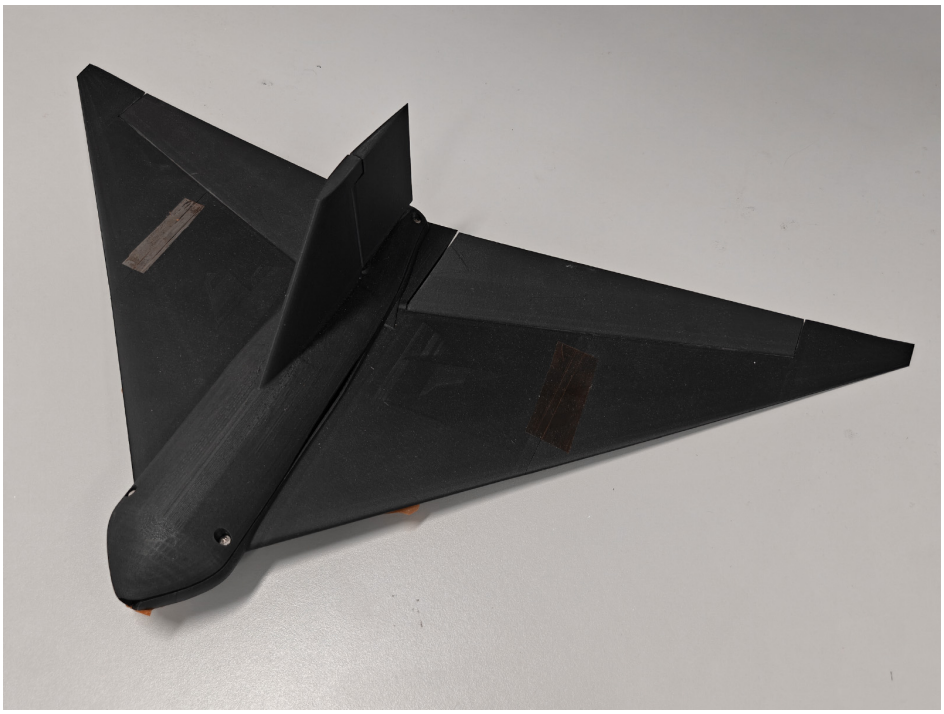


Figure 2.1: Previous Space Dart prototype used as the physical starting configuration.

The avionics system already included most of the components required for the operation of the glider. The flight control computer was a Matek F411-WTE, powered by a 4S battery with a nominal capacity of 1300 mAh. The video system included a CADDX ANT 1200TVL camera and a TBS Unify Pro 5G8 V3 video transmitter. Airspeed measurement was provided by a Matek ASPD-4525 system, while navigation and telemetry were based respectively on a Seeed Studio GNSS module and a Matek ELRS-R24-D telemetry receiver. [2]

The moving control surfaces were actuated by 9 g plastic-geared servos. Two servos were used for the elevons and one for the rudder. A fourth servo was also included in the previous avionics configuration for a possible parachute deployment system, although the parachute itself was not physically integrated into the prototype.

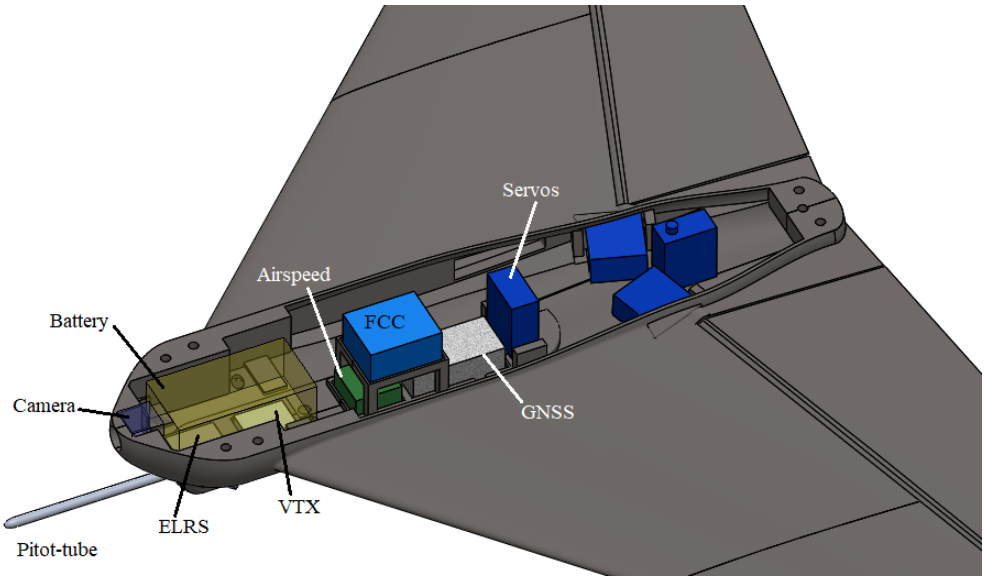


Figure 2.2: Previous avionics configuration of the Space Dart prototype.

A summary of the main onboard components is reported in Table 2.1. The table is intended only to identify the hardware inherited from the previous prototype, since the changes in component position and integration are discussed in Chapter 3.

Table 2.1: Main avionics components of the previous prototype.

Component	**Model / specification**	**Function**
Flight control computer	Matek F411-WTE	Flight control
Battery	4S, 1300 mAh, 130C	Power supply
Camera	CADDX ANT 1200TVL	Onboard video
Video transmitter	TBS Unify Pro 5G8 V3	Video transmission
AirSpeed system	Matek ASPD-4525	Airspeed measurement
GNSS	Seeed Studio 113020003	Position measurement
Telemetry system	Matek ELRS-R24-D	Telemetry communication
Control servos	9 g plastic-geared	Surface actuation

The prototype was divided into several printed components to allow manufacturing and assembly. The main structure consisted of an upper fuselage section, two lower fuselage halves and two outer wing sections. The elevons were manufactured separately, while a small removable lid was used for the Pitot installation. The assembly used a combination of alignment pins, screws and permanent glued connections depending on the component.

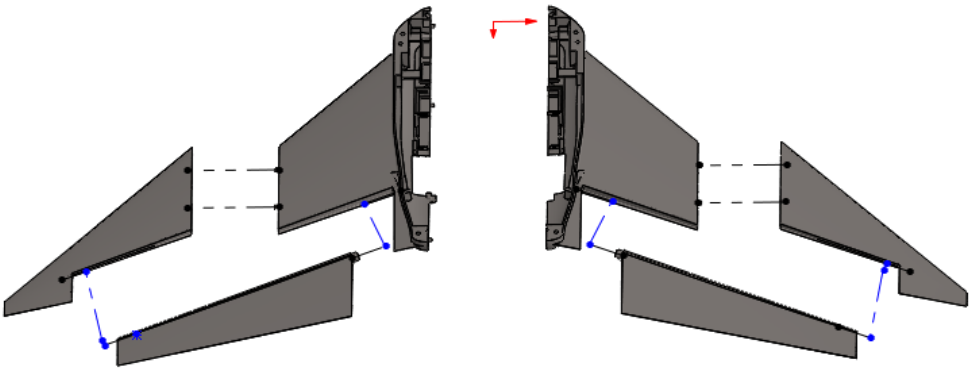


Figure 2.3: Subdivision of the previous Space Dart prototype.

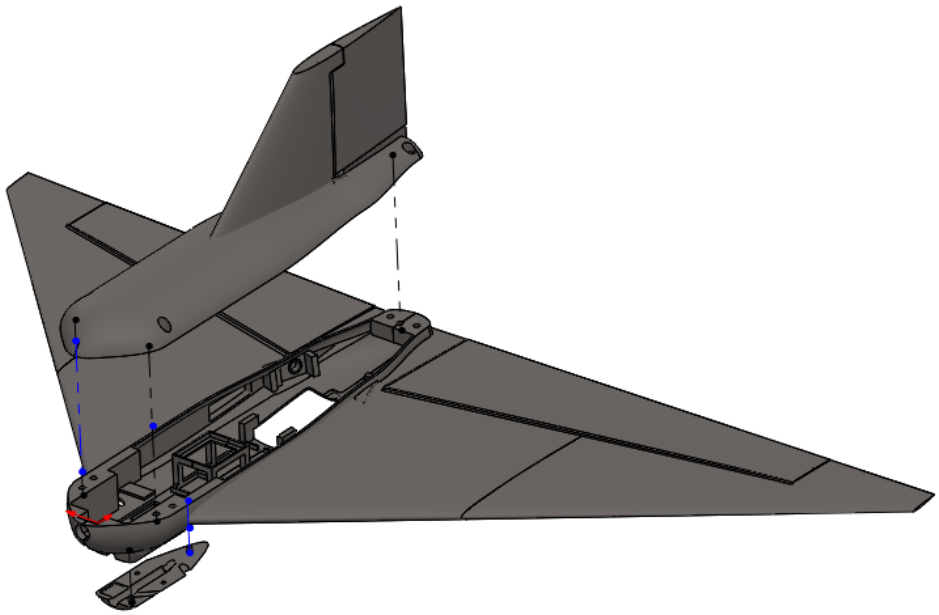


Figure 2.4: Subdivision of top panel and Pitot panel.

The ground equipment had also already been defined. A RadioMaster Pocket transmitter was used for command and telemetry communication, while video reception was based on a directional Yagi antenna. The system also allowed flight information to be recorded for later analysis, which is relevant to the flight-test methodology proposed later in this thesis. [2]

This previous prototype therefore provided the physical structure, avionics hardware and general assembly concept inherited at the beginning of the present work. The aerodynamic geometry, however, was subsequently modified before the development of the final CAD configuration using Autodesk Fusion software [7]. The final aerodynamic reference adopted in this thesis is introduced in Section 2.2.

2.2 Aerodynamic Reference Configuration

2.2.1 Latest Aerodynamic Geometry

The aerodynamic configuration used as the reference for the present CAD redesign was the final configuration obtained in the previous aerodynamic study, referred to as V1_4. This configuration was developed from the earlier V1 geometry after a sequence of modifications aimed mainly at improving the stability characteristics of the aircraft. The detailed aerodynamic design process is not repeated here and can be found in the previous study.

The final configuration maintained the same general delta-wing layout and overall size of the original concept, but several geometric parameters were modified. In particular, the wing dihedral was changed from a negative to a positive value, the trailing-edge sweep was reduced, the vertical stabilizer was resized, and both the rudder and elevons were reduced compared with the original configuration. The fuselage was also lengthened. The final wingspan remained approximately 0.688 m, while the fuselage length was approximately 0.345 m.

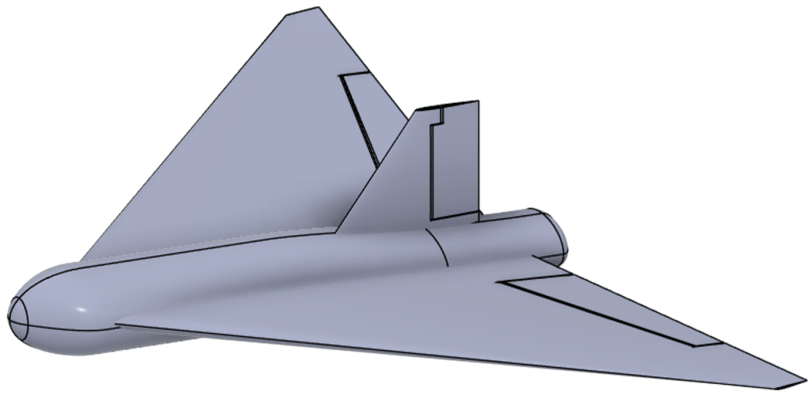


Figure 2.5: Final aerodynamic reference configuration V1_4.

The most relevant geometric differences between the inherited V1 configuration and the final V1_4 configuration are summarized in Table 2.2. Only the parameters that changed significantly and are useful for understanding the present redesign are reported here. A more complete geometric description can be included in the appendix.

Table 2.2: Main geometric differences between the inherited V1 configuration and the final V1_4 aerodynamic configuration.

Parameter	**V1**	**V1_4**
Wing leading-edge sweep	44.4°	42.3°
Wing trailing-edge sweep	10°	6°
Wing dihedral	−6°	+4°
Fuselage length	0.300 m	0.345 m
Fin height	0.090 m	0.080 m
Fin root chord	0.200 m	0.100 m
Fin tip chord	0.100 m	0.040 m
Rudder chord	0.070 m	0.030 m
Elevon root chord	0.080 m	0.047 m
Elevon tip chord	0.040 m	0.0192 m

[2] [3]

Some of the final geometric values were independently checked using the OpenVSP model and the CAD geometry developed during the previous aerodynamic study, since not all dimensions were explicitly or consistently reported in the corresponding thesis. These checks were used only to define the final reference geometry adopted in the present work.

The most important change for the overall aircraft configuration was the reversal of the wing dihedral from −6° to +4°, introduced during the aerodynamic development to obtain the required lateral stability. The final V1_4 configuration also used smaller control surfaces and a reduced vertical stabilizer compared with V1. These changes directly affected the available internal space and the position of several mechanical interfaces, and therefore became important constraints for the CAD redesign discussed in Chapter 3.

2.2.2 Aerodynamic Properties

The final V1_4 geometry was analysed and validated in the previous aerodynamic study using CFD at both sea-level and stratospheric conditions. In the present thesis, these results are treated as inherited reference data and are not recalculated. Only the main aerodynamic and dynamic properties relevant to the development of the prototype and to the proposed flight-test methodology are summarized here.

At sea level, the final CFD equilibrium condition was found at an angle of attack of approximately 2.79°, with an equilibrium velocity of 35.47 m/s and a glide angle of approximately 10.04°. The corresponding lift coefficient was $C_L = 0.094$.

The main static stability derivatives also showed that the final configuration satisfies

the basic longitudinal, lateral and directional stability conditions. In particular, the final CFD values gave

$$C_{m_\alpha} = -0.617, \qquad C_{l_\beta} = -0.060, \qquad C_{n_\beta} = 0.020.$$

The negative values of C_{m_α} and C_{l_β} indicate longitudinal and lateral static stability, while the positive value of C_{n_β} indicates directional stability. This represents an important improvement compared with the original V1 configuration, which presented an incorrect sign of C_{l_β} and was therefore laterally unstable.

The dynamic characteristics of the final configuration are particularly relevant for the flight-test methodology proposed later in this thesis. The main sea-level dynamic modes obtained from the CFD-based model are summarized in Table 2.3.

Table 2.3: Main dynamic modes of the final V1_4 configuration at sea level.

Mode	**Period / eigenvalue**	**Frequency**	**Damping / stability**
Short period	$T = 0.204$ s	$\omega = 32.085$ rad/s	$\zeta = 0.279$
Phugoid	$T = 12.405$ s	$\omega = 0.508$ rad/s	$\zeta = 0.098$
Roll	$\lambda = -28.471$	–	Stable
Dutch roll	$T = 3.180$ s	$\omega = 2.794$ rad/s	$\zeta = 0.707$
Spiral	$\lambda = -13.710$	–	Stable

All the main dynamic modes are stable at sea level. The short-period mode is fast and relatively well damped, while the Phugoid has a much longer period and lower damping. The Dutch-roll mode is also stable and considerably more damped than the Phugoid. The roll and spiral modes are aperiodic and both have negative eigenvalues.

Among these modes, the Phugoid and Dutch roll are of particular interest for the present work because they can be excited through dedicated flight manoeuvres and compared with the theoretical predictions. For this reason, their periods and damping characteristics will later be used as the main reference for the proposed experimental methodology.

The aerodynamic efficiency of the final configuration was also evaluated in the previous study. At sea level, the maximum ratio C_L/C_D was approximately 10 and occurred at an angle of attack close to 5°.

The same configuration was also analysed at an altitude of 20 km, corresponding to the long-term operational objective of Space Dart. The main results relevant to the present work are summarized in Table 2.4.

Table 2.4: Selected aerodynamic and dynamic properties of V1_4 at 20 km altitude.

Property	**Value**	**Comment**
Equilibrium velocity	138.323 m/s	$M \approx 0.47$
Phugoid	$T = 59.878$ s, $\zeta = 0.146$	Stable
Dutch roll	$T = 0.580$ s, $\zeta = 0.009$	Stable, poorly damped
Spiral mode	$\lambda = +0.003$	Slightly unstable
Maximum efficiency	$C_L/C_D \approx 8$	At $\alpha \approx 5°$

At 20 km, the longitudinal modes remain stable, although the Phugoid period becomes significantly longer than at sea level. The main differences appear in the lateral-directional behaviour. The Dutch-roll mode remains stable but becomes very lightly damped, while the spiral mode becomes slightly unstable. These aspects were identified in the previous aerodynamic study as open points for future development.

The natural equilibrium velocity at this altitude also corresponds to approximately Mach 0.47, exceeding the $M < 0.3$ design constraint considered in the previous study. It was noted that this condition could be modified through elevon trimming rather than operating at the natural zero-deflection equilibrium point. [3]

The aerodynamic results presented in this section therefore define the theoretical reference associated with the geometry physically implemented in the present thesis. The geometry and its main constraints provide the starting point for the CAD redesign described in Chapter 3, while the predicted dynamic modes will later be used as the reference for the proposed flight-test methodology.

Chapter 3

CAD Redesign and System Integration

The aerodynamic configuration introduced in the previous chapter provided the starting geometry for the development of the new Space Dart prototype. However, moving from the theoretical geometry to a complete physical model required a substantial redesign of the existing CAD configuration making use of the latest Autodesk Fusion software [7].

The change in geometry affected the space available for the avionics and, in particular, the integration of the control-surface actuation system. Several components also presented practical problems in their previous positions, such as the exposed Pitot tube and antennas. The internal architecture was therefore reorganized while keeping most of the existing avionics components.

At the same time, the external geometry had to be divided into separate components to make the prototype manufacturable and accessible during assembly. The final subdivision was developed considering the available internal space, assembly requirements, printing constraints and the connection between the different parts of the aircraft.

This chapter describes the main decisions and iterations that led to the final CAD model. First, the redesign of the avionics configuration is presented, followed by the resulting final internal layout. The final subdivision of the aircraft is then introduced and the reasoning behind the main splits is discussed. Finally, the geometric and mass properties of the completed configuration are summarized.

3.1 Redesign of the Avionics Configuration

The redesign of the internal configuration was carried out while retaining most of the avionics inherited from the previous prototype. The main objective was therefore not to select a new avionics system, but to adapt its integration to the new geometry and solve the practical limitations of the previous layout.

The process was developed through several CAD iterations, with the position of each component evaluated according to the available space, its functional requirements and its interaction with the surrounding systems. Since the internal volume is limited, changes to one component often influenced the possible position of others.

The following subsections present the main components that required modification.

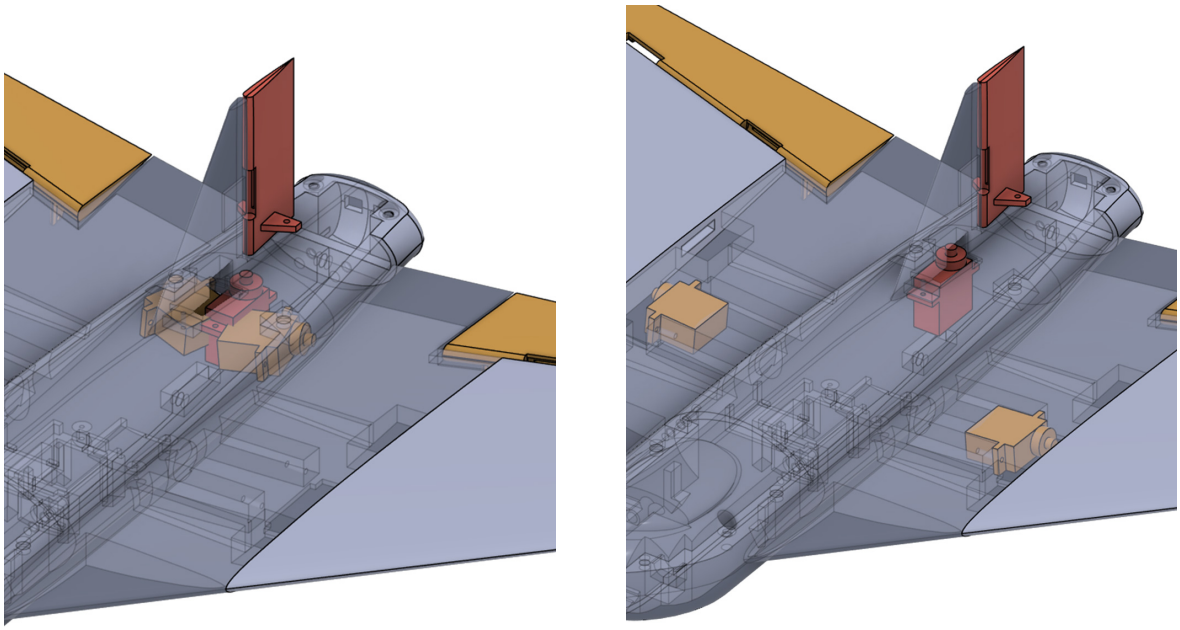
For each of them, the initial problem is introduced first, followed by the main design considerations and the solution adopted in the final configuration.

3.1.1 Servo Configuration

In the previous avionics configuration, the servos controlling the elevons were located inside the fuselage. Each servo was positioned so that its output shaft was aligned with the rotation axis of the corresponding control surface, allowing the servo to actuate the elevon directly.

With the new aerodynamic configuration, keeping the same solution became difficult. The elevons were reduced in size and their hinge line moved further towards the rear and away from the fuselage. As a consequence, the position required for the servos also moved towards a region where the available internal space was more limited. Several configurations were considered while trying to keep the servos inside the fuselage, but it was difficult to obtain enough space while maintaining a simple connection with the control surfaces.

The final solution was to move the two elevon servos inside the wings, closer to the front of the fuselage where space allowed them to fit. This configuration was also inspired by solutions commonly used in small RC aircraft. A small opening on the lower surface of each wing allows the servo arm to protrude outside and connect directly to the corresponding elevon through a 1.5 mm steel rod.



(a) Intermediate configuration with the elevon servos located inside the fuselage.

(b) Final configuration with the elevon servos integrated into the wings.

Figure 3.1: Evolution of the elevon servo integration: (a) intermediate in-fuselage configuration; (b) final wing-mounted configuration.

The hinge system was also changed. The previous prototype used 3D-printed pivots, which represented a possible weak point of the mechanism. These were replaced with flat nylon hinges commonly used in model aircraft. Two hinges are inserted between each elevon and the corresponding wing section, providing a simple rotation axis without relying on a printed pivot.

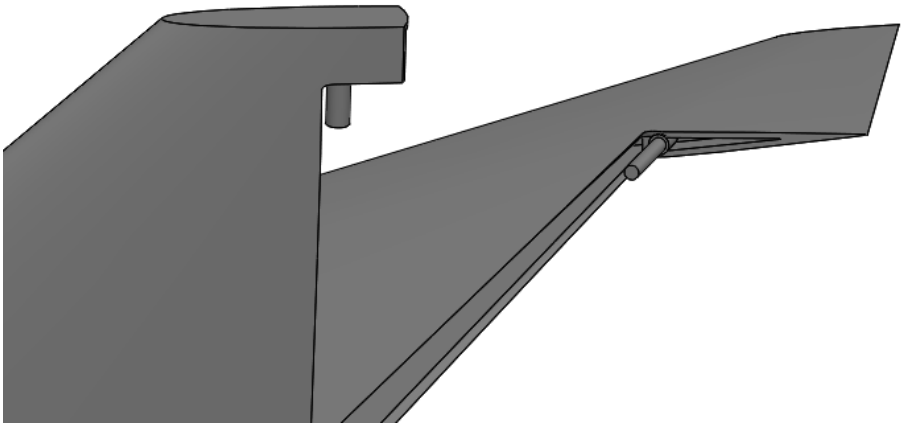


Figure 3.2: Previous hinges' weak point.

The two elevon servos were also changed from the previous 9 g plastic-geared servos to 13 g metal-geared servos. The new servos provide a stronger actuation system and are considered more suitable for the final configuration.

The rudder required fewer changes because its servo could still be positioned inside the fuselage. The servo is located close to the fin, with a symmetric arm protruding through the upper part of the fuselage. The arm is connected to the rudder through 1.5 mm steel rods, creating a push-pull mechanism. The previous 3D-printed pivot was also replaced in this case by a flat nylon hinge inserted between the fin and the rudder.

3.1.2 Pitot Tube and AirSpeed System

In the previous configuration, the Pitot tube was mounted on the lower part of the fuselage and protruded outside the aircraft. This position created two main problems. First, the Pitot represented a relatively large external element compared with the overall size of the glider. More importantly, its position made it particularly exposed during landing, where it could easily hit the ground and break.

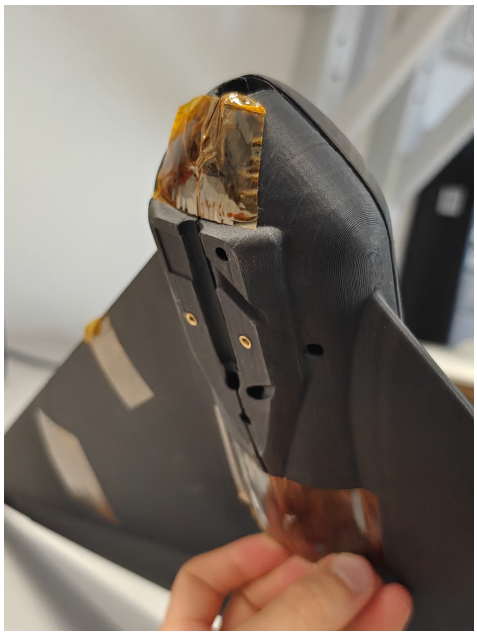


Figure 3.3: Previous Pitot housing.

One of the first alternatives considered was to move the Pitot inside the vertical fin. This solution would have removed the component from the lower part of the fuselage without requiring it to protrude from the front of the aircraft. In practice, the available space inside the fin was not sufficient to accommodate the Pitot correctly. The position of the AirSpeed unit also became difficult to manage, and the connection between the two components would have required the pressure lines to bend excessively.

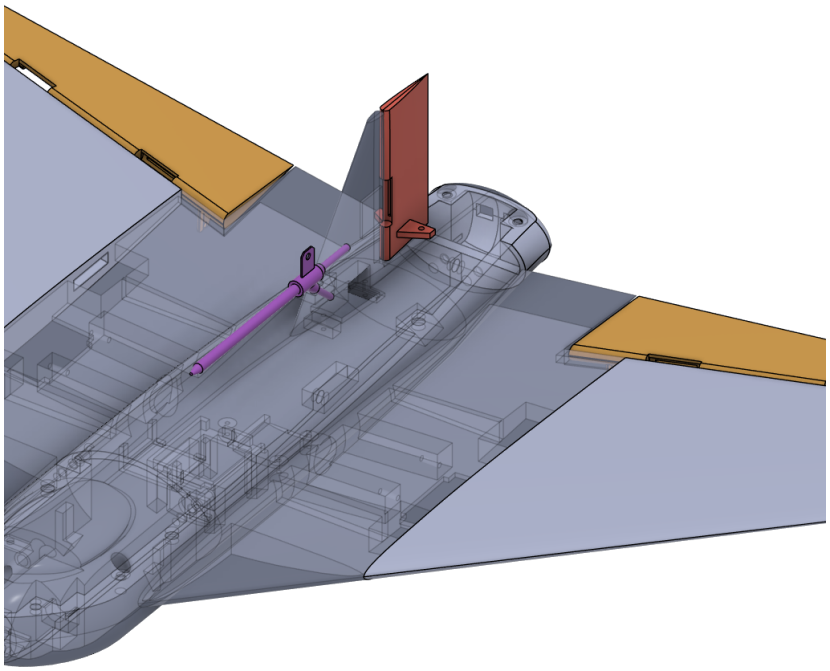


Figure 3.4: Intermediate configuration with the Pitot tube integrated inside the vertical fin.

The final solution was to move the Pitot to the upper front part of the fuselage. The top fuselage was slightly modified by adding a small bump around the component to provide the required clearance. The Pitot itself fits directly into a dedicated feature in the printed structure, avoiding the external panel and fastening system used in the previous configuration.

The relocation of the Pitot also required the AirSpeed unit to be moved. In the previous prototype, the AirSpeed unit was positioned below the flight control computer, which was convenient for the original lower Pitot installation. With the new configuration, it was moved above the FCC and placed on a small platform connected to the top fuselage. This position shortened and simplified the connection with the Pitot and made the complete system easier to integrate into the new geometry.

The final arrangement removed the most exposed component from the lower surface of the aircraft and provided a more compact integration of the Pitot and AirSpeed system within the fuselage.



Figure 3.5: Final Pitot configuration solution on the 3D printed model.

3.1.3 Video Transmission Antenna

In the previous prototype, the video transmission antenna was positioned outside the fuselage. Although this type of installation is common on RC aircraft and drones, the antenna was relatively large compared with the dimensions of Space Dart and represented another external component protruding from the aircraft.

For the redesigned prototype, the objective was to integrate the antenna inside the fuselage while still using the available internal volume efficiently. The final position was selected in the lower front part of the fuselage, below the battery and close to the camera. This location provides a favourable orientation towards the ground, where the directional Yagi antenna is used for video reception. A sufficient clearance was maintained between the antenna and the battery, while no metallic components or wiring are located in its immediate surroundings. The antenna is separated from the outside only by the approximately 2.5 mm thick PLA fuselage wall, which is not expected to significantly affect the video signal. The final installation should nevertheless be verified through a ground range test with the aircraft fully assembled.

The associated video transmission unit was placed underneath the flight control computer, taking advantage of the free volume created by the elevated FCC support.

This allowed both the antenna and the related electronics to be contained within the aircraft rather than requiring an external installation.

The final configuration provided a cleaner integration of the video transmission system and reduced the number of components protruding from the fuselage.

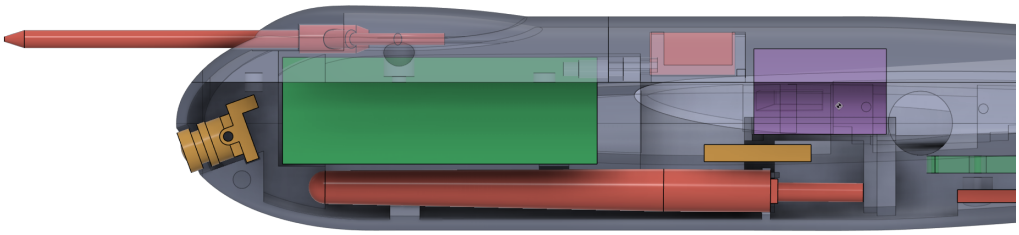


Figure 3.6: Final VTX Antenna configuration CAD view.

3.1.4 ELRS and Telemetry System

In the previous configuration, the telemetry transmitter was located in the front part of the fuselage, directly below the battery. Its antennas were routed outside the aircraft and fixed to the lower surface of the wings. Although this arrangement allowed the system to operate, the position of the transmitter close to the battery was considered undesirable because the surrounding components could affect signal transmission through physical screening or electromagnetic effects.

The new configuration was designed to increase the separation between the telemetry system and the battery while also bringing the antennas inside the aircraft. The available space at the rear of the fuselage provided a suitable alternative and allowed the complete system to be moved away from the more crowded front section.

The ELRS transmitter was therefore relocated to the rear part of the fuselage, together with its antennas. In the final configuration, the complete telemetry system is contained inside the aircraft, removing the antennas previously attached to the lower surface of the wings.

This solution increased the separation between the telemetry system and the battery while also providing a cleaner integration of the antennas within the final CAD

configuration.

3.1.5 Battery

The battery used in the previous prototype has a capacity of 1300 mAh and a discharge rating of 130C. Such a high discharge capability is not particularly useful for Space Dart, since the aircraft is an unpowered glider and does not have the high current demand normally associated with an electric propulsion system.

For the intended application, battery capacity is a more relevant parameter, as the avionics must remain powered throughout the flight. Replacing the battery with a higher capacity alternative was therefore considered. The main limitation is the available space inside the fuselage, since an increase in capacity generally also results in a larger battery, particularly in length.

For the current prototype, the original battery was retained. Its position was also kept approximately unchanged, directly behind the camera in the front part of the fuselage. The available volume accommodates the battery well and its position provides a useful contribution to the required center of gravity location.

A different battery can therefore be considered in a future configuration, while the current component was considered sufficient for the development and planned flight testing activities.

3.1.6 Flight Control Computer

Unlike several of the other avionics components, the flight control computer (FCC) did not require a significant change in position. It was already located close to the center of gravity of the aircraft, making its original position suitable for the redesigned configuration.

The FCC module is now mounted on an elevated rectangular support rather than directly occupying the lower internal volume of the fuselage, similarly to how it was mounted on the previous prototype. This arrangement creates additional usable space underneath the board, which is used to accommodate other components of the avionics system.

The FCC therefore remained approximately in its original position, while the surrounding CAD geometry was redesigned to use the limited internal volume more efficiently.

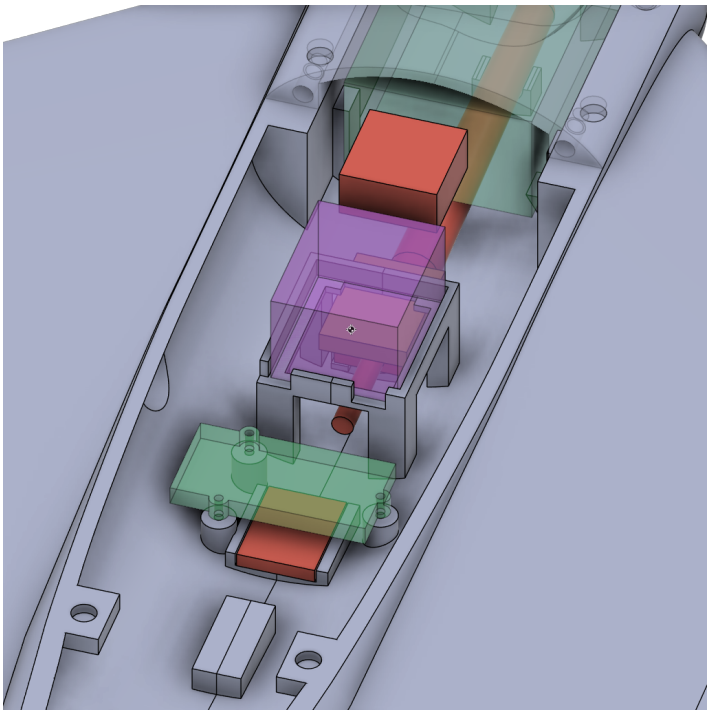


Figure 3.7: Final FCC support structure and CG position for reference.

3.1.7 GNSS

The GNSS system had fewer geometric constraints than other components because its position was not directly linked to a control surface or external measurement device. The position of its antenna was instead considered more important, since keeping it separated from the other avionics components can reduce possible signal screening.

The available space in the rear part of the fuselage allowed both the GNSS unit and its antenna to be moved away from the more crowded front section of the aircraft. The GNSS was therefore positioned towards the rear of the fuselage, close to the telemetry system.

Its antenna was placed at the very rear of the aircraft, where it could remain more isolated from the other internal components. This arrangement also made use of a region of the fuselage that became available after reorganizing the overall avionics layout.

3.1.8 Camera

The camera was already positioned at the front of the previous prototype and this location was maintained in the redesigned configuration. The front of the fuselage provides a direct view outside the aircraft and there was no reason to relocate the component.

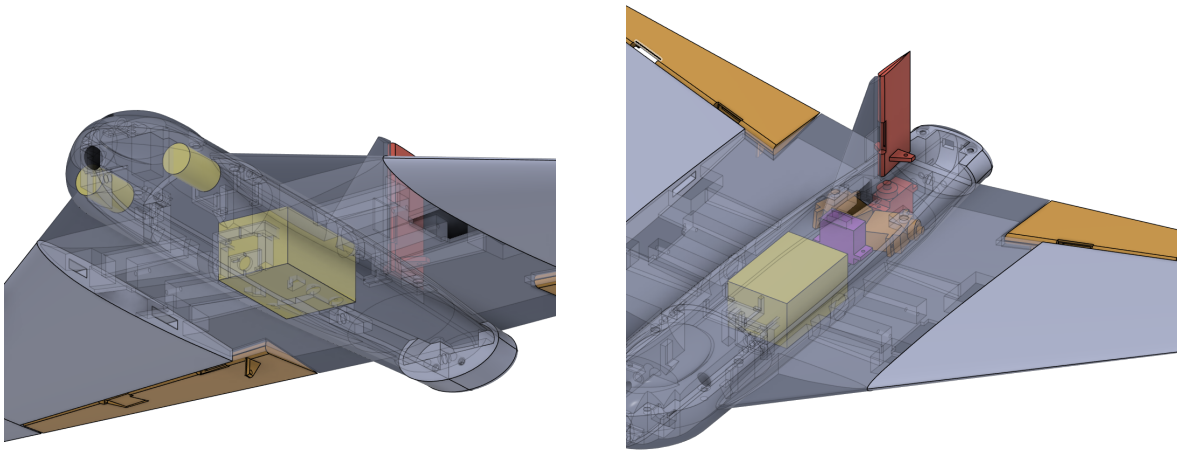
A small change was made to its orientation. The camera was angled slightly downward by 20° to provide a better view during flight. This modification became easier after relocating the Pitot tube, since the previous lower Pitot installation occupied part of the area in front of the camera and could enter its field of view.

The camera therefore required only a minor modification compared with the other avionics components, with its original position retained and only its orientation adjusted in the final CAD configuration.

Parachute Integration

The previous prototype included the possibility of using a parachute as an additional recovery system. Although the parachute itself had not been physically installed, a fourth servo was already included in the avionics configuration to actuate its opening mechanism.

The parachute was initially maintained during the first iterations of the new internal architecture. One of the configurations placed it in the central region of the fuselage, together with the additional space required for its deployment mechanism. Its position also affected the mass distribution of the aircraft, requiring two cylindrical ballast masses of approximately 50 g each towards the front of the fuselage to maintain the required center of gravity position.



(a) Early configuration showing the parachute and the two forward ballast masses.

(b) Early configuration showing the parachute and servo arrangement.

Figure 3.8: Early avionics-layout iteration including the parachute system: (a) parachute and forward ballast masses; (b) parachute and servo arrangement.

As the internal configuration developed, the limited available volume made the

integration of the complete system increasingly difficult. In addition to the parachute itself, enough space had to be reserved for a reliable deployment mechanism. For this reason, the parachute was removed from the current prototype, together with the fourth servo dedicated to its actuation.

The parachute remains a possible future development of Space Dart, but its integration was not considered necessary for the manufacturing and flight-testing objectives of the current prototype.

3.2 Final Avionics Configuration

The redesign process described in Section 3.1 resulted in the final avionics configuration shown in Figure 3.9. Most of the original components were retained, while their positions and the surrounding CAD geometry were modified to better use the available internal volume.

At the front of the aircraft, the camera is located at the nose, followed by the battery. The Pitot tube is integrated into the upper part of the fuselage, while the video transmission antenna is contained in the lower front region.

The central part of the fuselage is organized around the flight control computer (FCC), which remains close to the center of gravity of the aircraft. The AirSpeed unit is positioned above the FCC, while the VTX is located underneath it. The GNSS unit is placed immediately behind the FCC, with the ELRS transmitter positioned below it.

Towards the rear of the aircraft, the GPS antenna is located behind the rudder servo to provide greater separation from the other avionics. The two telemetry antennas are positioned below this region and oriented approximately 45° towards the front and outside of the aircraft. The rudder servo remains close to the vertical fin, while the two elevon servos are integrated directly inside the wings.

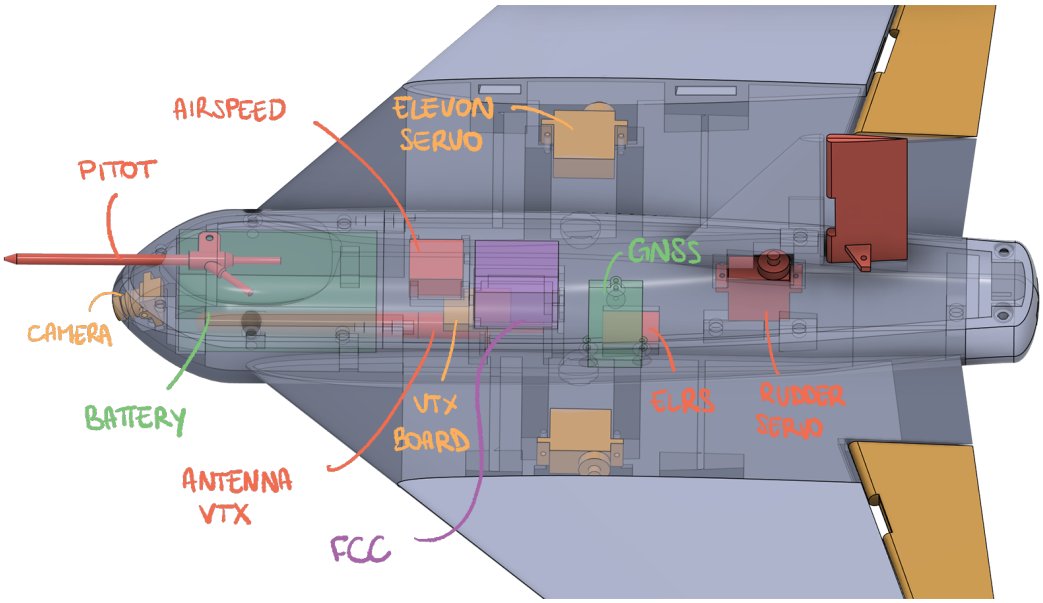


Figure 3.9: Final Avionics Configuration inside the Glider.

The final arrangement represents the configuration used for the manufactured prototype. Compared with the previous architecture presented in Section 2.1, the main changes concern the integration of the control-surface servos, the Pitot and AirSpeed system, and the relocation of the communication and navigation systems. The resulting CAD configuration also provided the starting point for defining the final subdivision of the aircraft, presented in the following section.

3.3 Final Prototype Subdivision

The final CAD model was divided into several components to satisfy different manufacturing, assembly and integration requirements. Some divisions were required by the build volume of the 3D printer, while others were introduced to improve printing orientation, provide access to the internal components or simplify the assembly of the prototype. The development process that led to these choices is discussed in Section 3.4; this section only presents the final subdivision and the position of each parting plane.

To define the position of the different splits, the reference frame used in the Fusion 360 model is adopted throughout this chapter. The origin of this reference frame, referred to as the *CAD reference frame*, is located 0.016 m behind the tip of the fuselage. The x-axis is aligned with the longitudinal direction of the aircraft and is positive

towards the rear, while the y-axis follows the spanwise direction and is positive towards the left wing. The z-axis is oriented vertically. The $y = 0$ and $z = 0$ planes are located along the symmetry axes of the fuselage.

The locations of the final parting planes are summarized in Table 3.1. Symmetric divisions on the left and right sides of the aircraft are reported together, since they represent the same design choice.

Table 3.1: Location and main purpose of the parting planes in the final CAD configuration.

Division	**Plane**	**Coordinate [m]**	**Main reason**
Top / bottom fuselage	XY	$z = 0.00961$	Assembly / access
Front / back top fuselage	YZ	$x = 0.085$	Printer size / orientation
Back bottom fuselage	YZ	$x = 0.302$	Printer size / adaptability
Wing / fuselage	XZ	$y = \pm 0.100$	Assembly / connection
Left / right bottom fuselage	XZ	$y = 0$	Printing orientation
Central wing / wing tip	XZ	$y = \pm 0.2492$	Printing / supports

The first division separates the upper and lower regions of the fuselage at $z = 0.00961$ m. The top fuselage is further divided at $x = 0.085$ m, while the rear section of the bottom fuselage starts at $x = 0.302$ m. Along the spanwise direction, the outer wings are separated from the central structure at $y = \pm 0.100$ m, while the remaining bottom fuselage is divided along the aircraft symmetry plane at $y = 0$.

Finally, each wing is divided into a central wing section and a wing tip at $y = \pm 0.2492$ m. This last division is symmetric on the two sides of the aircraft and corresponds to the same geometric feature on both wings.

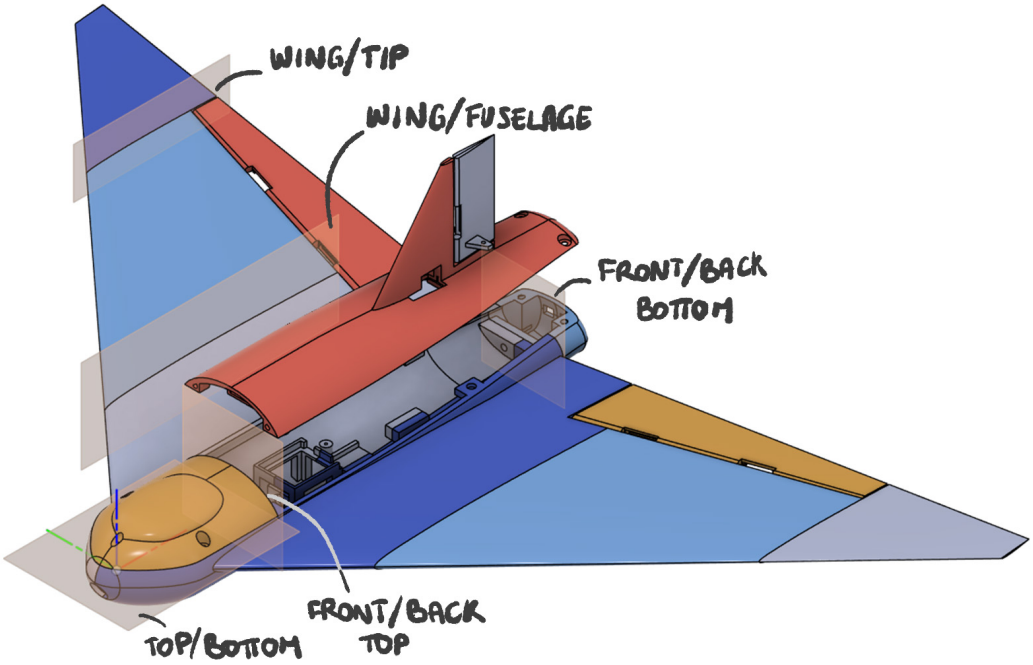


Figure 3.10: Final subdivision of the Space Dart CAD model and adopted reference frame.

The reasons behind these locations cannot be attributed to a single constraint. In several cases, manufacturing limitations were considered together with assembly and integration requirements. For this reason, the development of each division and the alternatives considered before reaching the final configuration are discussed separately in the following section.

3.4 Prototype Subdivision Design Process

The final subdivision presented in Section 3.3 was not defined only by the build volume of the 3D printer. The position of each split was selected while developing the CAD model, considering the accessibility of the internal components, printing orientation, assembly and the need to maintain suitable connections between the different parts of the aircraft.

The subdivision was developed progressively. The fuselage was first separated into upper and lower sections to provide access to the avionics. These sections were then divided further according to their individual manufacturing and assembly requirements. Finally, the wings were separated from the central structure and divided again to account for their specific manufacturing strategy.

The following subsections describe this process in the same order in which the main divisions of the aircraft were defined.

Top and Bottom Fuselage Division

The first main division separates the fuselage into an upper and a lower section along most of its length. A similar concept was already present in the previous prototype, as opening the fuselage from the top provides direct access to the internal avionics during installation and assembly.

The position of the split had to be modified for the new geometry. The previous configuration had a negative wing dihedral of $\Gamma = -6°$, while the new configuration uses a positive dihedral of $\Gamma = +4°$. As a result, the highest point where the wings connect to the fuselage moved upward.

The separation plane was therefore positioned slightly above the highest point of the wing-fuselage connection. This allowed the top fuselage to be removed without interfering with the wings while maintaining access to the internal components.

The resulting upper component is referred to throughout this work as the *Top fuselage*, while the remaining central structure forms the basis of the *Bottom fuselage*.

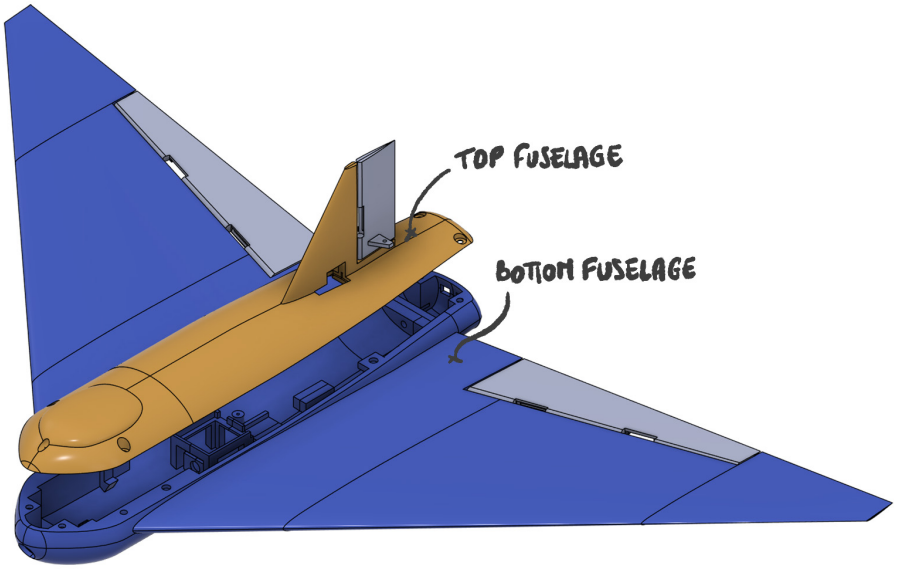


Figure 3.11: Top and Bottom Fuselage Division.

Top Fuselage Division

The top fuselage could not be manufactured as a single component because its length exceeded the available printer build volume. It therefore required an additional transverse division.

The position of this split was not selected only according to the printer dimensions. During the first printing trials, it became clear that the front and rear regions of the top fuselage benefited from different printing orientations. The rear section includes the vertical fin, while the front section contains the geometry introduced to accommodate the Pitot tube.

The split was consequently positioned slightly behind the Pitot installation, approximately 10 cm from the nose of the aircraft. This produced two components referred to as the *Front Top fuselage* and *Back Top fuselage*.

Although manufactured separately, the two parts have no independent functional purpose and are generally referred to together as the top fuselage. Their specific printing orientations and settings are discussed in Section 4.3.1 of Chapter 4.

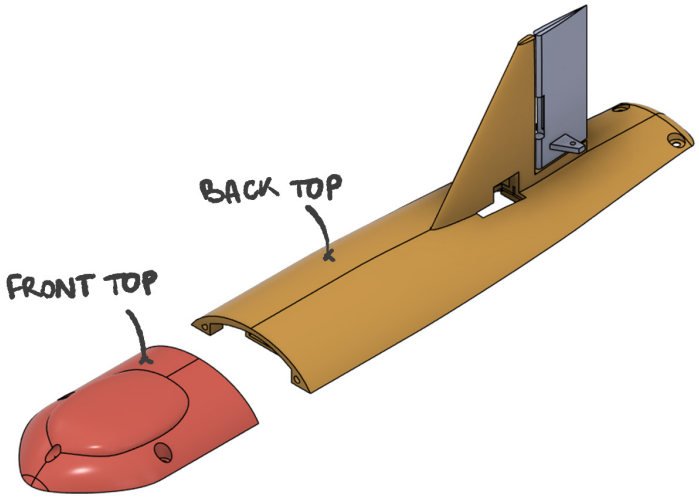


Figure 3.12: Top Fuselage Division.

Back Bottom Fuselage Division

The lower part of the fuselage also exceeded the printer build volume and could not be manufactured as a single component. A separate rear section was therefore introduced, creating the component referred to as the *Back Bottom fuselage*.

Keeping this region as a separate component also provided additional flexibility for the integration of the release mechanism. At this stage of the design, the final release solution had not yet been defined, and modifications to the rear part of the aircraft were still expected.

Separating this section meant that the rear geometry could be modified and reprinted without requiring the complete lower fuselage to be manufactured again. This possibility was later used when a modified rear component was produced for the second prototype to accommodate an initial release-system configuration.

The back bottom fuselage therefore originated from a printing constraint, while also providing a practical way of keeping the rear geometry adaptable during the development of the release mechanism.

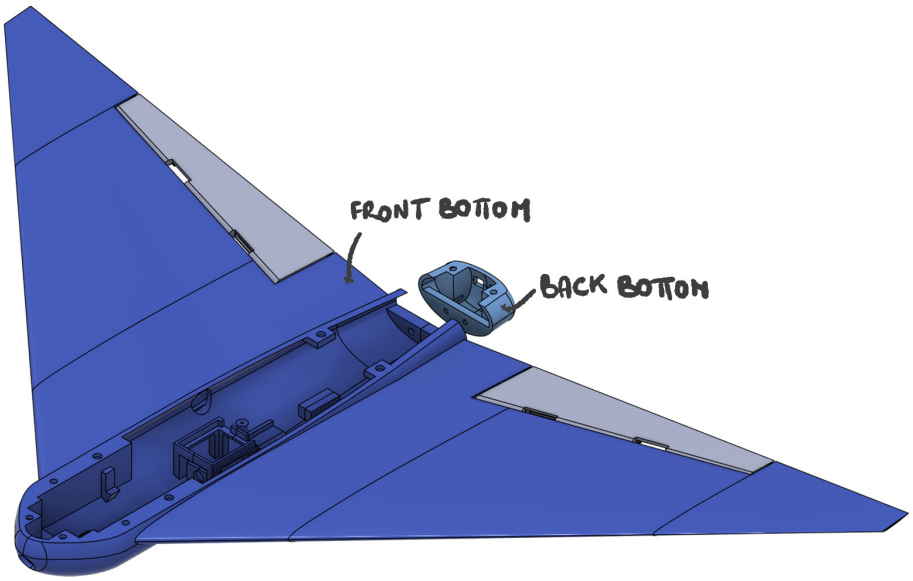


Figure 3.13: Back Bottom Fuselage Division.

Wing and Fuselage Division

The next step was to define the separation between the wings and the central fuselage structure. A division directly at the wing root was initially avoided because this region represents the main connection between the wings and the fuselage. Keeping part of the wing integrated with the central structure provided a larger connection region for the removable outer wing sections.

An alternative similar to that used in some model aircraft, where the two wings form a continuous component passing through the fuselage, was also considered. This

solution was discarded because the wing structure would occupy a significant part of the internal fuselage volume and interfere with the installation of the avionics.

The initial concept was therefore to place the split a short distance away from the fuselage. As the internal architecture developed, the position of the elevon servos became another important constraint. Since the servos were moved inside the wings, the final split was positioned further outboard, slightly beyond their location.

This allowed the servos to be installed in the inner wing region before attaching the remaining wing sections. The final division is located symmetrically on the two sides of the aircraft and leaves the wing-root region integrated with the bottom fuselage.

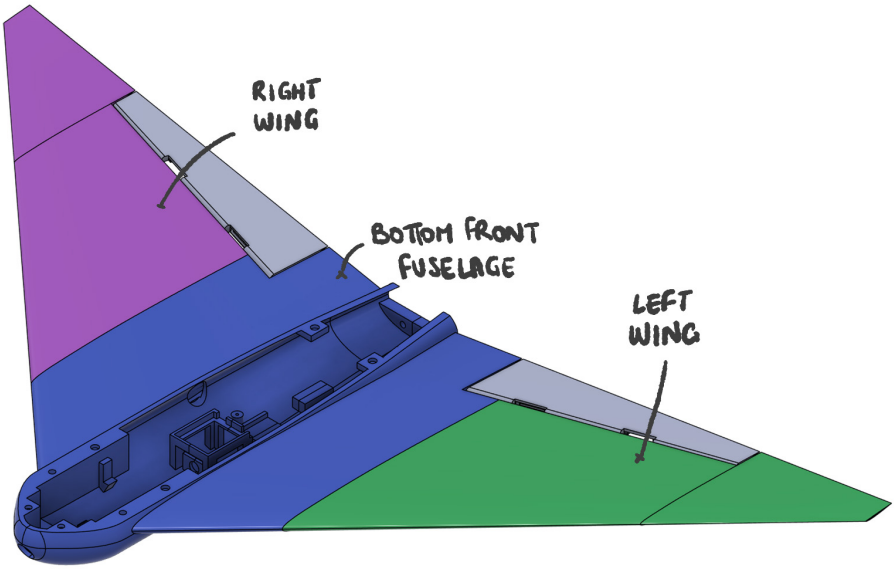


Figure 3.14: Wing and Fuselage Division.

Left and Right Bottom Fuselage Division

After separating the outer wings and the rear fuselage, the remaining lower central structure still presented difficulties when considered as a single printed component. In particular, the geometry of the wing-root regions required a suitable printing orientation to obtain an acceptable result.

The remaining bottom fuselage was therefore divided along the aircraft symmetry plane, producing two mirrored components referred to as the *Left Bottom fuselage* and *Right Bottom fuselage*.

This division allowed the two symmetric parts to be oriented individually during printing while maintaining the wing-root sections as part of the central fuselage structure.

Once assembled, the two components form the main lower section of the aircraft.

The printing strategy associated with this division is discussed separately in Section 4.3.2.1 of Chapter 4.

Wing Division

Ideally, each outer wing would have been manufactured as a single component. An additional division became necessary because of the decision to manufacture the wings using Aero PLA.

As discussed in Chapter 4, Aero PLA presented significant difficulties when support structures were required. The travel of the print head between the wing and the supports produced considerable stringing and reduced the quality and reliability of the print. Printing the complete wing as a single component would therefore have required a support configuration that was not considered suitable for this material.

Each wing was consequently divided into a central wing section and a wing tip. The position of the division was selected close to the end of the elevon cut, where the local geometry already provided a convenient transition between the two sections.

This final split was therefore introduced mainly as a consequence of the manufacturing strategy. The two components are treated as a single wing after assembly, while their printing process and the specific behaviour of Aero PLA are discussed in Section 4.5

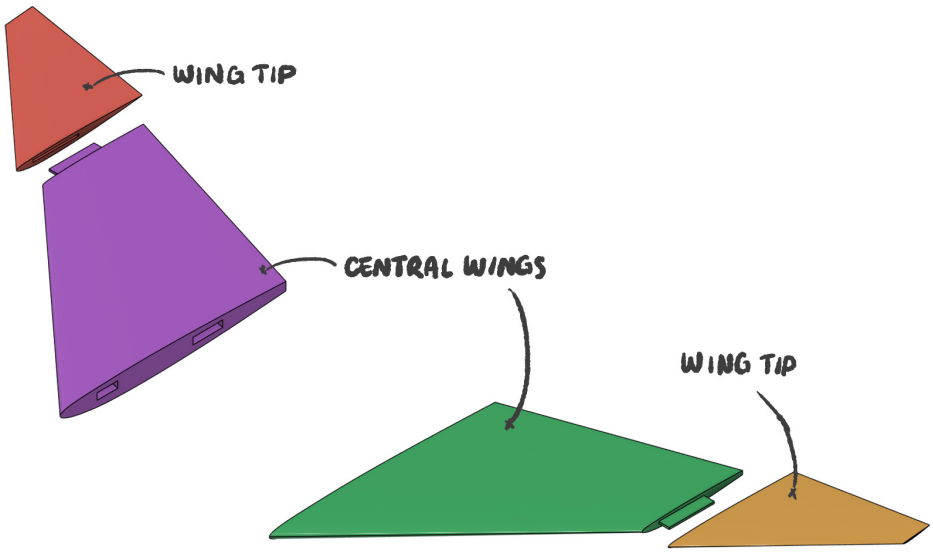


Figure 3.15: Wing Division.

3.5 Final Geometric and Mass Properties

The mass properties of the final CAD configuration were evaluated after completing the structural and avionics integration described in the previous sections. For comparison, the same properties were also obtained for the structure alone, with all avionics components and screws/magnets removed.

The reference frame is the same as that previously adopted for the CAD model, with the X axis directed longitudinally towards the rear of the aircraft, the Y axis along the wingspan and the Z axis in the vertical direction.

The main mass properties of the two configurations are compared in Table 3.2.

Table 3.2: Comparison of the mass properties of the structure and the final integrated CAD configuration.

Property	**Structure only**	**Final CAD**
Mass [kg]	0.5016	0.7201
X_{CG} [mm]	166.308	138.843
Y_{CG} [mm]	0.073	0.044
Z_{CG} [mm]	4.652	3.995
I_{xx} [kg m^2]	0.00463088	0.00481810
I_{yy} [kg m^2]	0.00394011	0.00591633
I_{zz} [kg m^2]	0.00838264	0.01051356

The structural mass obtained from the CAD model is approximately 0.502 kg, while the complete configuration has a mass of approximately 0.720 kg. The avionics and the other components represented in the complete assembly therefore account for approximately 0.219 kg, corresponding to about 30.4% of the total CAD mass.

The integration of these components also has a significant effect on the longitudinal position of the centre of gravity. For the structure alone, the centre of gravity is located at approximately

$$\mathbf{r}_{CG,\text{structure}} \simeq \begin{bmatrix} 166.31 \\ 0 \\ 4.65 \end{bmatrix} \text{mm}, \tag{3.1}$$

while for the complete configuration it becomes

$$\mathbf{r}_{CG,\text{final}} \simeq \begin{bmatrix} 138.84 \\ 0 \\ 4.00 \end{bmatrix} \text{mm}. \tag{3.2}$$

Since the X axis is directed towards the rear of the aircraft, the integration of the avionics moves the centre of gravity forward by approximately 27.5 mm. The lateral coordinate remains effectively zero in both configurations, as expected from the symmetry of the aircraft about the XZ plane.

The addition and distribution of the internal components also modify the moments of inertia. The change in I_{xx} is relatively small, from 0.00463 to 0.00482 kg m^2, while larger increases are obtained for I_{yy} and I_{zz}. These variations result from both the additional mass and its distribution within the aircraft.

For completeness, the moments and products of inertia of the final integrated configuration, calculated about its centre of gravity, are

$$\mathbf{I}_{CG} = \begin{bmatrix} 0.00481810 & 0.0000000527 & -0.00018558 \\ 0.0000000527 & 0.00591633 & -0.000000452 \\ -0.00018558 & -0.000000452 & 0.01051356 \end{bmatrix} \text{kg m}^2. \tag{3.3}$$

The corresponding principal moments of inertia are

$$I_1 = 0.0048121 \text{ kg m}^2, \qquad I_2 = 0.0059163 \text{ kg m}^2, \qquad I_3 = 0.0105196 \text{ kg m}^2. \tag{3.4}$$

As expected from the symmetry about the XZ plane, the products of inertia I_{xy} and I_{yz} are very close to zero. The product I_{xz} remains non-zero, since symmetry about this plane does not require this term to vanish.

After manufacturing and complete assembly, the prototype was also weighed directly. The measured mass was approximately 0.740 kg, compared with the 0.720 kg predicted by the complete CAD model. The difference of approximately 20 g is associated with elements that were not fully represented in the CAD mass model, including wiring, magnets, adhesive and other small assembly components. For this reason, the measured value is more representative of the actual total mass of the prototype, while the CAD model provides the reference values for the centre of gravity and moments of inertia.

With the final geometry, internal configuration and mass properties defined, the next chapter describes the manufacturing process used to produce the individual components of the Space Dart prototype.

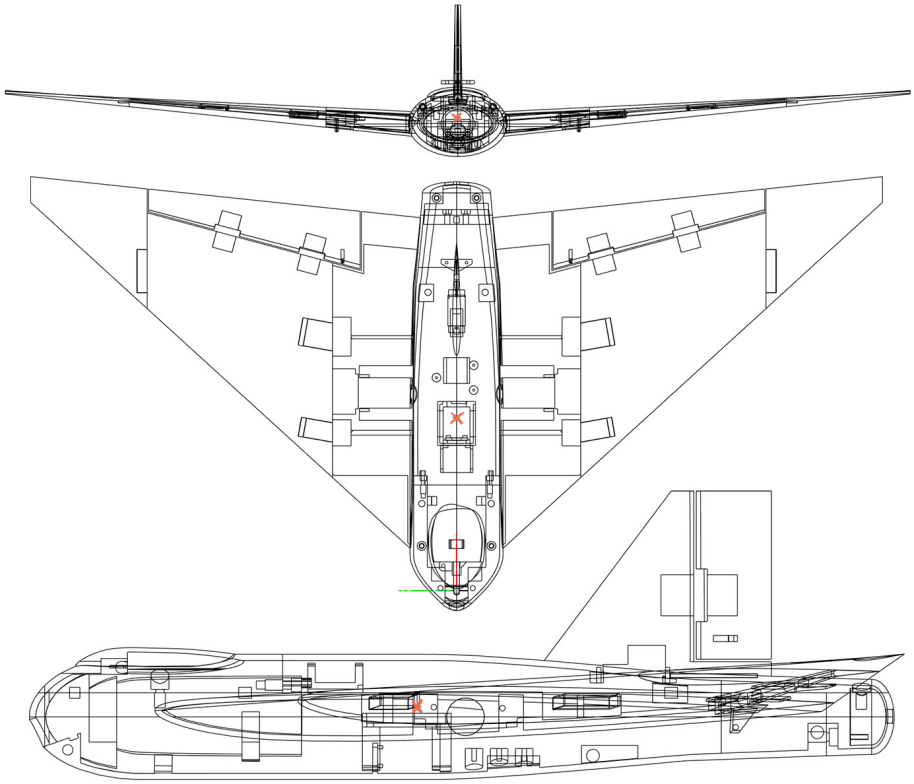


Figure 3.16: 2D view of the aircraft with CG position.

Chapter 4

Additive Manufacturing and Manufacturing Strategy

The CAD configuration developed in the previous chapter defined the geometry, subdivision and internal arrangement of the Space Dart prototype. The next step was to manufacture the resulting components, which required adapting the printing process to the geometry and function of each part.

This chapter describes the additive manufacturing strategy adopted for the prototype. After a brief introduction to the FDM process and the printer used, the manufacturing of the fuselage, control surfaces and wings is presented. Particular attention is given to printing orientation, material selection, support requirements and the practical iterations required to obtain usable components.

4.1 3D Printing Terminology, Process and Printer Overview

This section introduces the terminology and manufacturing concepts that are used throughout the rest of the chapter. The intention is not to give a complete overview of 3D printing, but only to define the terms needed to understand the manufacturing decisions, the printing problems encountered, and the parameter choices discussed in the following sections.

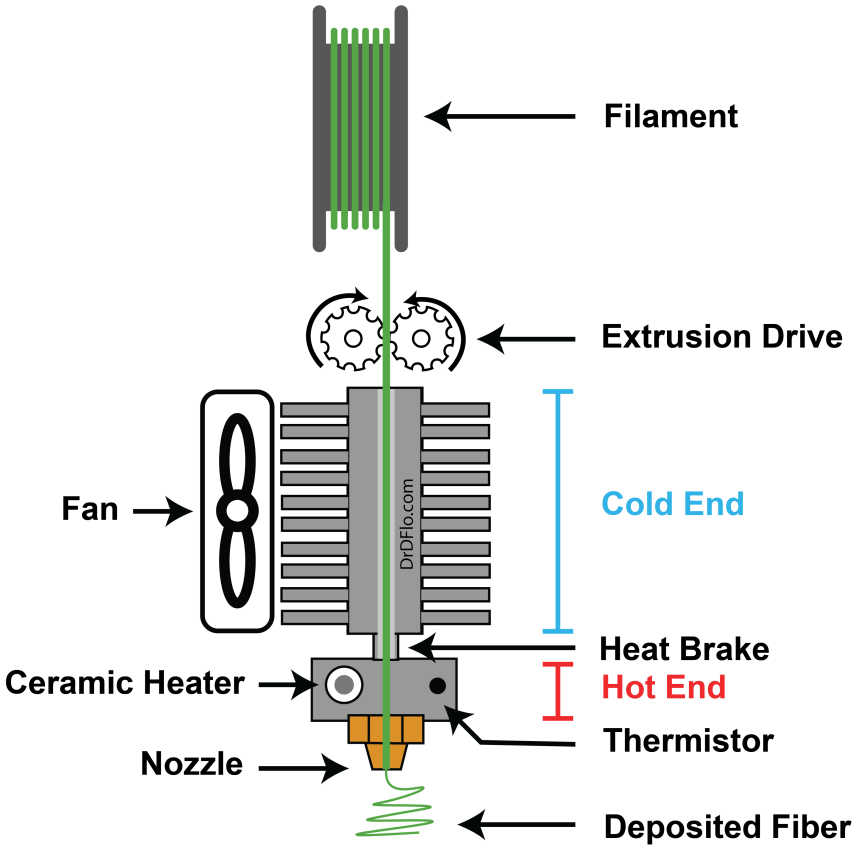


Figure 4.1: Schematic representation of the main components of an FDM 3D printer.

4.1.1 FDM/FFF Printing Process

Fused Deposition Modelling (FDM), also referred to as Fused Filament Fabrication (FFF), is an additive manufacturing process in which a 3D model is built by depositing successive layers of molten thermoplastic material. A solid filament is fed into a heated nozzle, where it is melted and extruded onto a build plate following a predefined path. Once a layer is completed, the nozzle (or the build plate, depending on the printer kinematics) moves upward by a small increment, and the next layer is deposited on top of the previous one. As each layer cools, it bonds to the one below, eventually creating the full 3D print. [8]

As shown in Figure 4.1, the main components involved in this process are the extruder, which pushes the filament forward, the hotend, which melts it, the nozzle, through which the molten material is extruded, and the build plate, on which the part is printed. These components are moved relative to one another by the printer's motion system according to the geometry to be printed.

4.1.2 Printer Components and Printing Parameters

- **Nozzle:** The nozzle is a brass or steel tip with a hole through which the molten filament is extruded. Nozzles are available in different diameters (usually 0.4 mm), and larger nozzles allow a higher material flow rate and therefore faster printing, at the cost of reduced resolution on small or detailed features. [9]
- **Layer height:** The layer height is the vertical thickness of each deposited layer. It controls the vertical resolution of the print: lower layer heights produce smoother surfaces and better resolution on curved geometries, but increase the total printing time, since more layers are needed to complete the same part.
- **Wall loops:** The wall loops are the outer contours of each layer, They refer to the outer layers of a printed object. The number of wall loops affects both the surface finish and the local strength of the printed part, since the walls are typically the most solid region of the cross-section.
- **Infill:** The infill is the internal structure that fills the volume enclosed by the wall loops. Rather than printing a fully solid part, the interior is usually filled with a repeating pattern at a chosen density, set to a percentage of the enclosed volume. The infill pattern (e.g., grid, honeycomb, gyroid) and density are chosen as a compromise between mechanical strength, weight, material usage, and printing time.
- **Printing speed:** The printing speed defines how fast the nozzle moves while extruding material and is generally different for various features (walls, infill, supports) to balance surface quality and printing time.
- **Travel:** Travel refers to the movement of the nozzle between two points without extruding material, for example, when moving from one printed feature to another. To avoid leaving thin strings of molten plastic behind during these movements, retraction is used: the filament is briefly pulled back into the nozzle before a travel move and pushed forward again once printing resumes, reducing unwanted material leakage.

4.1.3 Geometry-Related Printing Concepts

- **Printing orientation:** The printing orientation is the way a part is positioned on the build plate before slicing. Since FDM is an inherently layer-based process, the chosen orientation affects the surface finish, the need for support structures, the mechanical properties along different directions, and, in this project, whether a part fits within the printer's build volume.

- **Overhangs:** Overhangs are regions of a part that extend outward without sufficient material directly underneath them from the previous layer. Beyond a certain overhang angle, the printer cannot reliably deposit material in mid-air, and supports become necessary. These are temporary structures printed alongside the part to hold up these regions during printing and are removed afterwards.
- **Brim:** The brim is a thin, single-layer flat area printed around the base of a part, connected to it but not part of the final geometry. It increases the contact area between the part and the build plate, improving adhesion and helping to prevent the corners of a print from lifting during printing.
- **Seam:** The seam is the point, within a single layer, where the nozzle finishes tracing a wall loop and moves on to the next feature. Since the extrusion pressure changes slightly whenever the nozzle stops or starts a loop, this point can leave a small bump or dent on the surface. If the printer places the seam in the same location on every layer, these small imperfections stack up and become visible as a thin vertical line on the finished part. [10]

4.2 Printer and General Printing Strategy

The prototype was manufactured using a Bambu Lab X1E 3D printer, which has a build volume of $256 \times 256 \times 256$ mm. The printer was selected primarily because it was the machine available in the FabLab where the work was carried out, and because its capabilities were suitable for the dimensions and level of detail required by the prototype.

Additive manufacturing was selected mainly for practical reasons. In particular, the accessibility of the equipment and the possibility of rapidly producing modified components made 3D printing particularly suitable. Once a modification was introduced in the CAD model, a new physical version could generally be produced within approximately 24 hours. This allowed the design to be quickly evaluated with physical components, testing true clearances and subsequently modifying the model without requiring a new manufacturing process or long lead times. This aspect was particularly useful during the development of the internal avionics architecture and actuation systems, where several alternative configurations were considered.



Figure 4.2: Bambu Lab X1E 3D printer used for manufacturing the prototype.

The dimensions of the printer represented one of the main constraints of the manufacturing process. Since the overall dimensions of the glider exceeded the available build volume, several components could not be manufactured as single pieces and required subdivision. The subdivision of the aircraft was not determined exclusively by the maximum printable dimensions. In several cases, a component could have been contained within the build volume, but printing it as a single piece would have resulted in an unsuitable orientation, excessive support material, reduced surface quality, or difficulties during assembly.

Based on these considerations, the manufacturing strategy was developed by evaluating the geometry of each component together with the constraints related to the printing process and the final integration into the aircraft. The main factors considered during the design and subdivision of each component were:

- available printer build volume;
- printing orientation;
- resulting surface quality;
- amount and accessibility of support material;
- structural integrity of the printed component;
- accessibility required for the installation of avionics and servos;

- ease of assembly and disassembly;
- compatibility between the printed components and their interfaces.

These constraints were taken into account from the early stages of the CAD design, rather than being addressed only after the geometry had been finalised. In some cases, achieving a suitable print orientation required modifications to the geometry or the subdivision of a component. In others, the main reason for splitting a part was to simplify access to the internal components during assembly. As a result, the final subdivision of the aircraft components represents a compromise between manufacturing, structural, and assembly requirements.

The reasons behind the subdivision of the fuselage, wings, and control surfaces are presented in the following sections. For each group of components, the selected print orientation and printing parameters are also described, together with the main manufacturing challenges encountered and the design iterations that were required.

Most of the structural components were manufactured using Basic White PLA (Polylactic Acid), a very commonly used material in 3D printing. The moving control surfaces were instead printed using coloured Basic PLA, mainly to make them easier to spot during flight. The wings were manufactured using Aero PLA, a foaming PLA chosen to reduce their overall weight. Since this material behaves differently during printing and requires a dedicated manufacturing strategy, its properties and the adopted printing approach are discussed separately in Section 4.5.1.

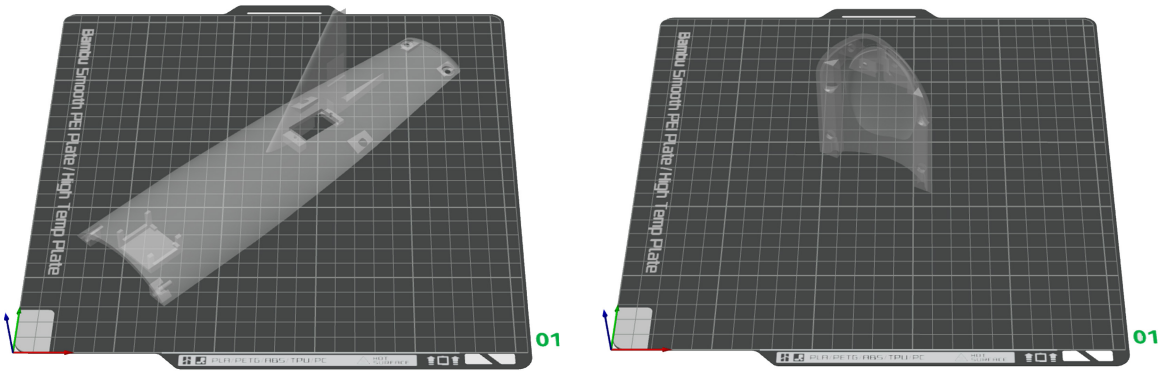
4.3 Fuselage

4.3.1 Top Fuselage

The upper part of the fuselage could not be printed as a single component because its overall dimensions exceeded the printer's build volume. For this reason it was then divided into two components approximately 10 cm from the nose of the fuselage. The position of this division was also selected according to the printing orientation required by the two sections.

The rear section contains the fin and was found to achieve significantly better print quality when printed vertically. The front section, however, was difficult to print correctly in the same orientation because of the geometry surrounding the Pitot tube. The division allowed the two components to be printed using different orientations and settings, as discussed in the following subsections.

The two resulting components in Figure 4.3 are referred to as *Back Top Fuselage* and *Front Top Fuselage* but they are generally referred to collectively as the *Top Fuselage*, since the two pieces do not have an independent functional purpose when separated.



(a) Back Top Piece (b) Front Top Piece

Figure 4.3: Orientation of the parts inside the build plate

4.3.1.1 Back top fuselage

The back top fuselage was printed using a standard layer height. Since the fuselage walls are relatively thin, with a thickness of approximately 2.5 mm, three wall loops and a 30% grid infill were selected to provide sufficient structural rigidity.

The printing speed of both the inner and outer walls was reduced by 50 mm/s to improve the overall print quality. The *slow down by height* function was also enabled. This was particularly useful for the thin fin, as the component required approximately six hours of printing. Slowing down the printing process in the upper portions reduced the probability of defects developing during the final stages of the print.

Supports were manually painted only in the most critical overhang areas(See Figure 4.4). This approach was used to minimise the amount of support material, since removing supports from the finished part is not always easy and can leave surface defects.

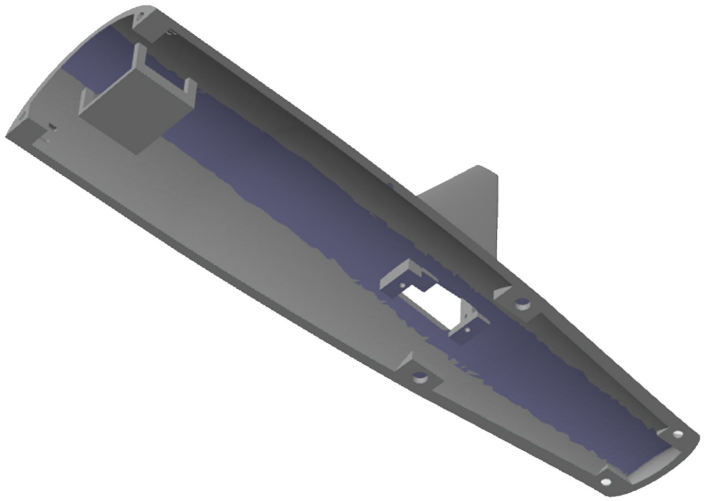


Figure 4.4: Support Map of the Top Back piece

The *top Z distance* was adjusted to make support removal easier. This resulted in a small reduction in the quality of the internal surface, which was considered acceptable since the affected surface is not externally visible.

Several printing tests were carried out to determine a suitable configuration for the tree supports. Increasing the distance between individual support branches made them easier to remove and also reduced material consumption. A branch distance of 10 mm was selected based on these observations.

The first printing test also showed insufficient adhesion of the first layer to the build plate. This was mainly related to the thin geometry of the fuselage. A 10 mm brim was introduced to improve adhesion, and the gap between the brim and the object was reduced from 0.10 mm to 0.07 mm.

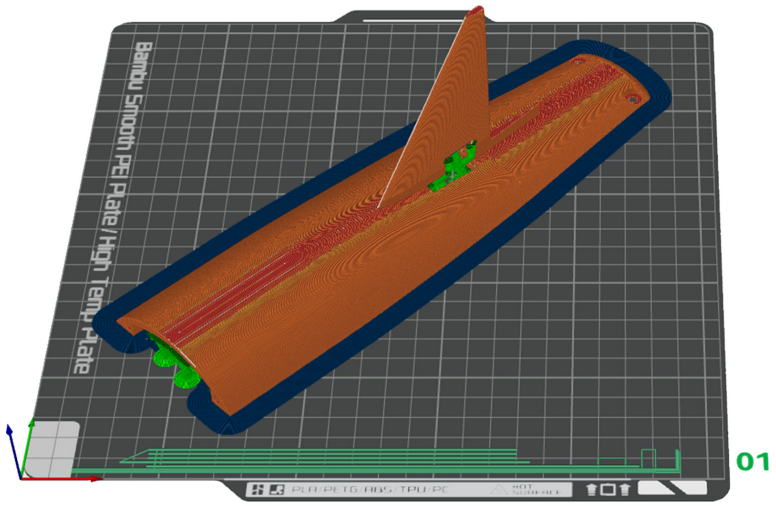


Figure 4.5: Sliced Back Top piece

4.3.1.2 Front top fuselage

The front top fuselage was initially tested using the same printing orientation as the back top fuselage. This configuration resulted in an unsuccessful print of the support structure around the Pitot tube. As you can see from Figure 4.3b the component was reoriented vertically, which significantly reduced the amount of required support material.

The vertical orientation introduced another problem. Since the component was tall and relatively thin, the first layers could lift from the build plate and the part was more susceptible to being knocked over during printing.

A larger brim of approximately 15 mm was tested to improve adhesion. Although this improved the adhesion to the build plate, one of the tests showed defects associated with the larger brim.

The infill pattern was then changed to gyroid. Grid infill is generally faster to print, but gyroid provided a more suitable result for this particular geometry.

The *slow down by height* function was also enabled to reduce the risk of defects during the upper portions of the print.

Supports were kept close to the default configuration, with a reduced *top Z distance* to facilitate their removal.

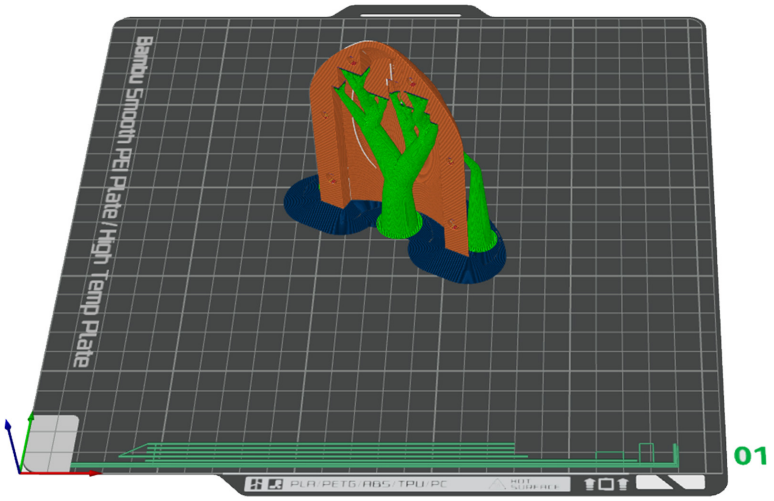


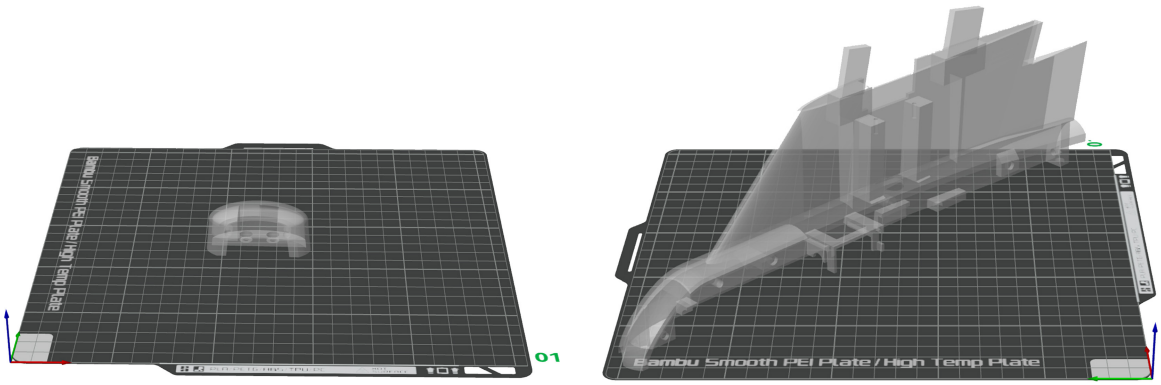
Figure 4.6: Sliced Front Top piece

4.3.2 Bottom Fuselage

The lower part of the fuselage was separated from the wings to satisfy both structural and assembly requirements discussed in Chapter 3. The connection between the fuselage and the wings was kept as close as possible to the wing root to preserve a solid structural connection, while the final position of the split also allowed the servos to be installed more easily before assembling the remaining wing sections.

The bottom fuselage was then divided into three components for manufacturing. Two of these components are symmetric and are referred to as the left and right bottom fuselage, while the rear section is referred to as the back bottom fuselage. The rear section was separated mainly because the complete bottom fuselage could not be printed within the available build volume. The split also provided some flexibility during the development of the rear connection and possible release mechanism.

The three components use essentially the same printing strategy and are therefore treated together in this section, with the specific differences in printing orientation and support configuration discussed in the following subsections.



(a) Back Bottom Piece (b) Left/Right Bottom Piece

Figure 4.7: Orientation of the parts inside the build plate

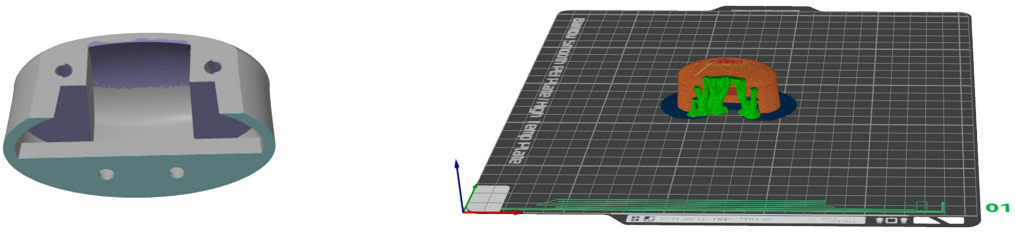
4.3.2.1 Left and Right Bottom Fuselage

The selected printing orientation was chosen primarily to obtain better print quality in the region where the wing connects to the fuselage.

The printing strategy was based on the successful results obtained with the back top fuselage. The same general settings were retained where applicable.

Supports were manually painted only in the most critical areas. The *On build plate only* support option was disabled because supports were also intentionally placed on internal regions of the wings. These supports could be removed using pliers and did not need to originate from the build plate.

During the initial printing tests, deformation of the first layer was observed at the rear region of the fuselage because the available brim was insufficient in that area. A larger brim, similar to the one used for the front top fuselage, was introduced to improve adhesion and prevent deformation.



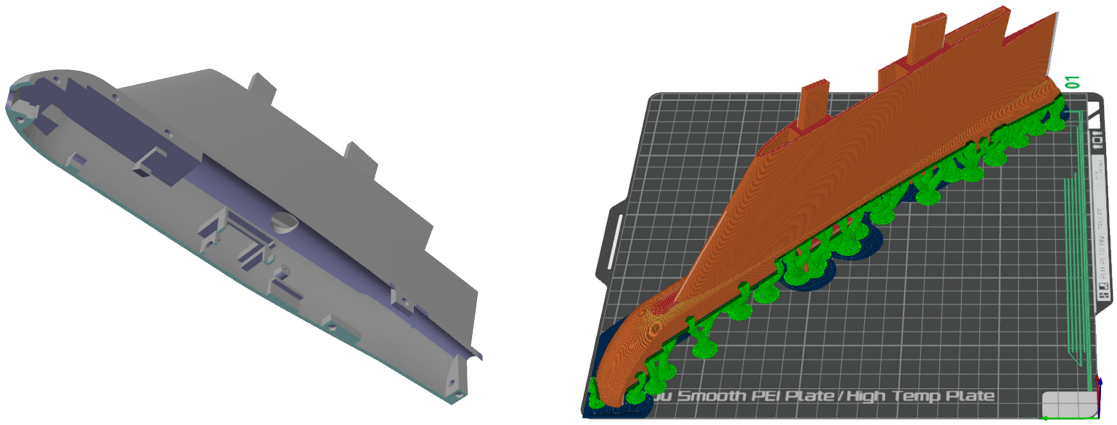
(a) Support Map (b) Left/Right Bottom Piece

Figure 4.8: Support Map and Sliced plate of the Back Bottom piece

4.3.2.2 Back Bottom Fuselage

The back bottom fuselage was printed using a different orientation from the left and right bottom fuselage sections. This orientation was selected to reduce the amount of required support material while maintaining suitable print quality.

Supports were also manually painted in the most critical areas, following the same approach used for the other fuselage components.



(a) Support Map (b) Left/Right Bottom Piece

Figure 4.9: Support Map and Sliced plate of the Left/Right Bottom piece

4.4 Moving Control Surfaces

The three moving control surfaces, consisting of two elevons and one rudder, were printed separately from the main aircraft structure. All three components were printed using coloured Basic PLA to make them easier to identify during assembly and subsequent

ground checks.

The components were printed vertically because this orientation provided better overall print quality. Their thin geometry made them particularly challenging to manufacture. During the initial printing tests, the parts could easily be knocked over once they reached a height of approximately 4.5 cm.

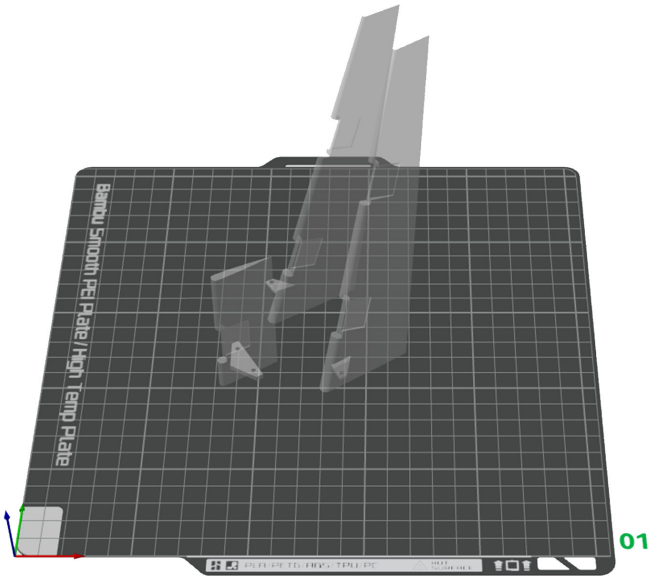


Figure 4.10: Elevons and Rudder pieces

Several configurations were tested to improve the stability of the prints. These included a brim larger than 10 mm, a reduction of the printing speed from approximately 80 mm/s to 40 mm/s at greater heights, and different printing configurations. None of these approaches provided a sufficiently reliable result.

The configuration that consistently produced successful prints used a gyroid infill with a density of 10% and two wall loops. This combination provided sufficient structural integrity while reducing the probability of failure during the printing of the thin components.

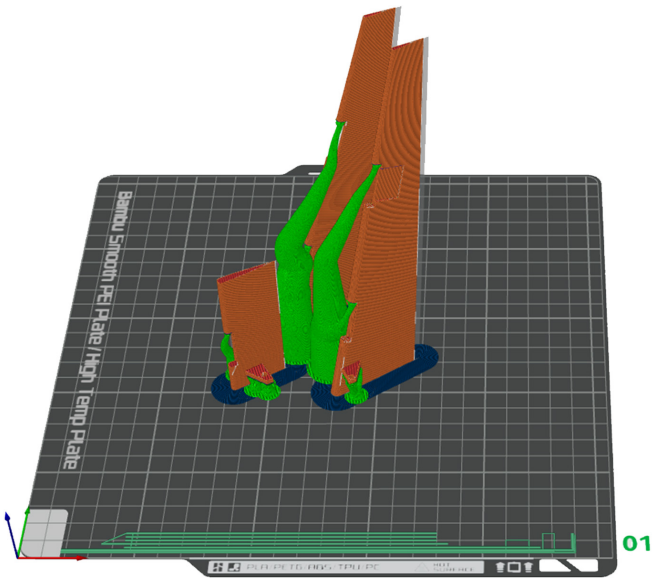


Figure 4.11: Sliced Build Plate of Moving Control Surfaces

4.5 Wings

4.5.1 Aero PLA: General Characteristics

For the aircraft prototype, Bambu Lab PLA Aero was selected because it can produce lightweight printed parts. Unlike standard PLA, PLA Aero is designed to foam in a controlled way during extrusion. As the material passes through the heated nozzle, it expands, so the printed part ends up with a much lower density than the filament itself. According to Bambu Lab, the filament has a density of about 1.21 g/cm^3, while the printed material can range from 0.55 to 1.05 g/cm^3, depending on the printing parameters used. [11]

The reduction in density is controlled mainly by the printing temperature and the flow rate ratio. A higher nozzle temperature generates more foaming, so the extruded material expands more. In the same way, lowering the flow rate ratio limits how much filament enters the nozzle, which also allows the material to expand. Bambu Lab reports foaming rates of up to about 120%.

This behaviour makes PLA Aero optimal for lightweight structures. Since the aircraft prototype includes a fairly large printed volume, lowering the material density gives a real reduction in mass without changing the external shape of the parts.

The final density of a PLA Aero part does not depend only on temperature and flow rate. Bambu Lab lists other factors that play a role, such as printing speed, wall thickness, model size, and infill density. This means the material properties are tied

closely to the chosen printing parameters, which makes process tuning an important part of the manufacturing strategy. Luckily, Bambu Lab also proposes a set of instructions specific for printing RC models. These were used as a base model for the following prints. [12]

Moisture sensitivity is another point to consider. Bambu Lab recommends drying PLA Aero at 55 °C for 8 hours before use, and storing it in an environment below 20% relative humidity. Moisture absorbed by the filament can affect both the stability of extrusion and the foaming behaviour, making the printed parts less consistent.

These characteristics make PLA Aero quite different from standard PLA. Rather than simply swapping one filament for another, the printing parameters need to be adjusted to reach a good balance between weight reduction, dimensional accuracy, surface quality, and repeatability. For this reason, material choice and parameter choice cannot really be treated separately for this prototype, but form part of the same manufacturing strategy.

PLA Basic and PLA Aero Comparison

The main printing parameters that separate PLA Aero from Bambu Lab PLA Basic are summarised in Table 4.1. The comparison is based on the ranges given by Bambu Lab and is meant to show the different processing needs of the two materials, rather than to define a single fixed printing profile.

Table 4.1: Bambu Lab PLA Basic vs Bambu Lab PLA Aero.

Parameter	**PLA Basic**	**PLA Aero**	**Relevance**
Printing temperature	190–230 °C	220–260 °C	Higher temperature means more foaming in PLA Aero
Recommended printing speed	< 300 mm/s	< 180 mm/s	PLA Aero needs more controlled extrusion
Flow rate ratio	0.96–1.00	0.50–0.80	Lower flow allows expansion and density reduction
Filament density	1.24 g/cm^3	1.21 g/cm^3	Similar before printing
Printed density	$\sim$1.21 g/cm^3	0.55–1.05 g/cm^3	Main source of mass reduction
Foaming rate	–	0–120%	Determines volumetric expansion during printing
Recommended drying	–	55 °C, 8 h	PLA Aero needs more drying

[11]

The main difference between the two materials is how they behave during extrusion, rather than the density of the filament itself. PLA Basic is meant to keep a nearly constant extrusion volume, with a flow rate ratio close to one. PLA Aero, instead, is printed with a lower flow rate and a higher nozzle temperature, which lets the material expand after leaving the nozzle. Because of this, the same external shape can be printed

using noticeably less material, but the expansion can compromise printing accuracy.

Temperature and flow rate are the main parameters controlling how much the material foams. Raising the nozzle temperature generally increases expansion and lowers the density of the printed part, and lowering the flow rate ratio has a similar effect. That said, the final mass of a component also depends on its wall thickness and infill density: increasing either one adds more solid material and therefore increases the mass of the part.

Printing speed also needs to be considered together with these parameters. Compared with PLA Basic, PLA Aero requires lower printing speeds to keep extrusion stable and foaming consistent. Since printing speed affects the thermal conditions the material goes through, it should not be changed on its own without also considering nozzle temperature and flow rate. These parameters work together to determine the final density and quality of the print. [11]

For the aircraft prototype, choosing PLA Aero meant more than just replacing one filament with another. It required a different printing strategy, where the process parameters directly affect the density and mass of the finished part. Reaching the intended weight reduction meant balancing material expansion against dimensional accuracy, surface quality, structural performance, and repeatability of the process.

The printing parameters selected for the manufactured prototype are discussed in the following sections, where the effect of temperature, flow rate, and printing speed on the final component mass is examined in more detail.

The slicer parameters used for the fabrication of the wings are summarised in Appendix B.1.

4.5.2 Aero PLA printing strategy and iterations

The wings were printed using a material called Aero PLA, a foaming type of PLA that expands when extruded. This allows a less dense print and can result in a printed part with approximately 50% of the weight of an equivalent part printed in Basic PLA, depending on the nozzle temperature and extrusion flow rate. Compared to Basic PLA, Aero PLA is less rigid and more flexible. This also gives the printed parts better resistance to impacts, allowing them to deform more easily without breaking.

The reduction in wing mass also affected the mass distribution of the aircraft. In particular, it changed the position of the centre of gravity (CG) and reduced the mass moment of inertia around the aircraft axes. The effect is particularly relevant for

the I_{xx} moment of inertia, which depends on the distribution of mass with respect to the longitudinal axis. Removing mass from the wings has a larger effect on I_{xx} than removing the same amount of mass from the fuselage, since the mass is located further from the roll axis. A lower I_{xx} results in a faster roll response for the same control authority. The use of Aero PLA therefore provided a useful reduction in wing mass, in addition to the manufacturing advantages discussed in Section 4.5.1.

However, printing Aero PLA was more difficult than printing Basic PLA and required several changes to the printing strategy.

One limitation that could not be avoided was the need to split each wing into two major parts. With Basic PLA, the complete wing could have been printed using supports without major issues. Aero PLA, instead, produced a large amount of stringing when printing between the wing and the support structures. This was caused by the additional travel of the extruder between the printed part and the supports. As a result, printing the complete wing in a single piece was not considered suitable. The wing was therefore divided into a central section and a wing tip. The exact position and design of this division are discussed in Chapter 3.

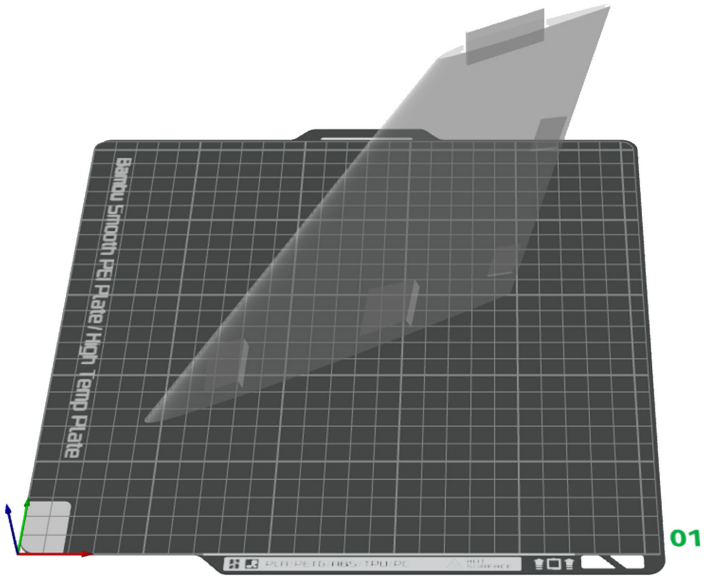


Figure 4.12: Central wing section positioned on the build plate before printing.

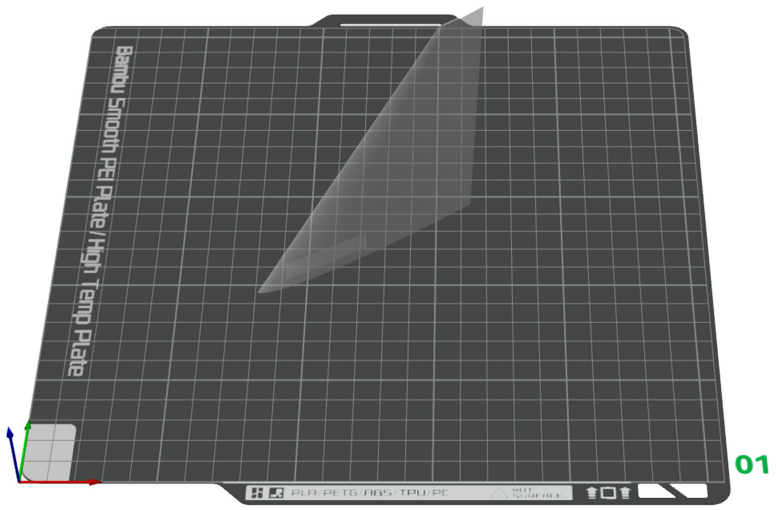


Figure 4.13: Wing tip positioned on the build plate before printing.

As already mentioned in Section 4.5.1, Bambu Lab provides recommended settings as a starting point for printing Aero PLA. These settings were used as a reference, but further modifications were required to obtain a reliable print.

One of the first problems concerned the position of the seam. The original seam position created visible bumps at different locations on the surface of the wing. Setting the seam position to “nearest” did not remove the bumps, but it moved them all to the leading edge of the wing. This made the problem easier to solve because the seams could be removed in a single operation with light sanding.

Another important setting was the “avoid crossing walls” option. This was enabled to reduce unnecessary travel of the extruder head inside the model. This was particularly useful around the connecting holes in the wing, which accommodate the connector pieces located in the left and right bottom fuselage sections. Reducing the amount of travel in these areas also helped to limit the amount of stringing produced by the Aero PLA.

The internal structure of the wing was also investigated through several printing tests. The first tests used a hollow configuration, but the resulting structure was too flexible and showed noticeable deformation. A gyroid infill was therefore selected as a better compromise between weight and rigidity. The final configuration used two wall loops and a gyroid infill with a density of 10%.

The choice of the gyroid pattern was also influenced by the behaviour of Aero PLA during printing. Compared with the initial configuration, it reduced the amount of

internal travel of the extruder and resulted in a more consistent printing process. After several tests, the 10% gyroid configuration provided the best result without adding unnecessary weight to the wings.

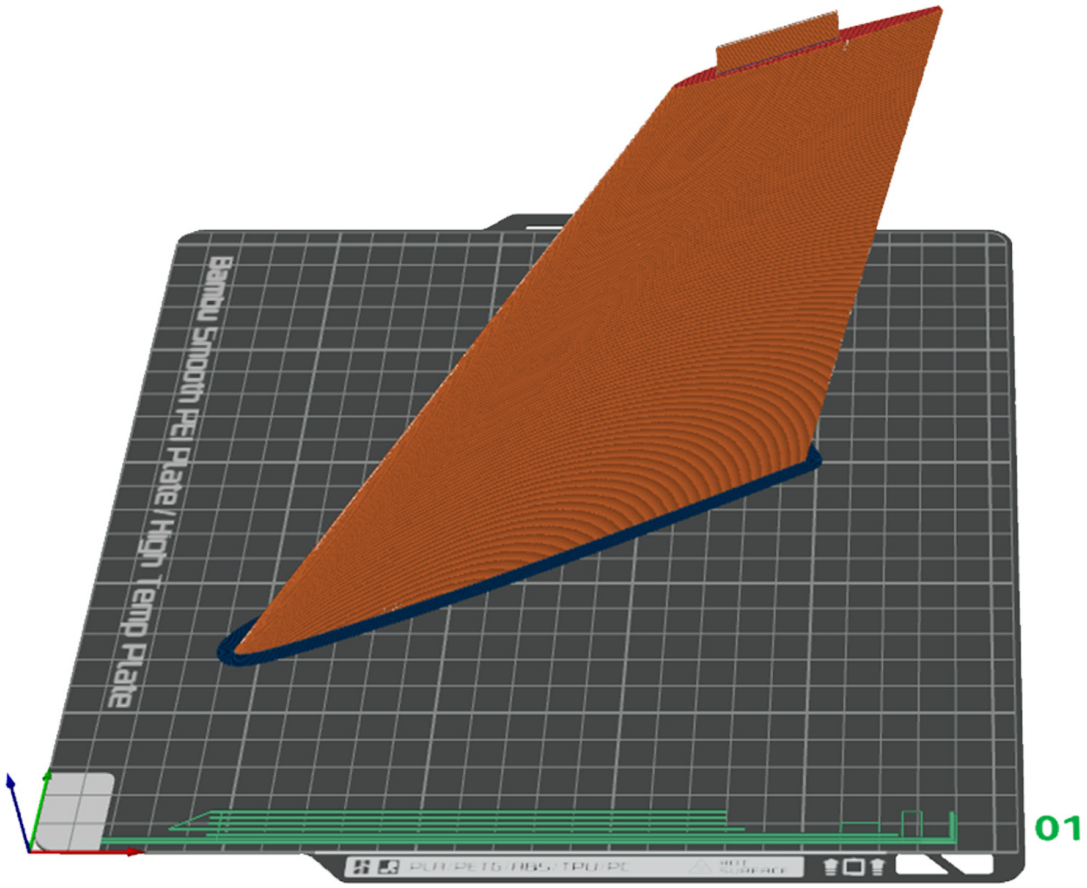


Figure 4.14: Sliced central wing showing the internal printing structure and gyroid infill.

The final printing configuration was therefore the result of several iterations rather than a direct application of the manufacturer's recommended profile. The main changes were made to reduce stringing, improve the surface finish and obtain sufficient rigidity while keeping the weight of the wings low. The complete set of printing parameters can be reported in the appendix and referenced here when required.

4.6 Post-Processing of Printed Components

Once removed from the build plate, some of the printed components required additional manual work before they could be used for assembly. Most of these operations were limited to support and brim removal, light sanding, and small dimensional adjustments. The amount of post-processing depended mainly on the material and geometry of each

component, with the Aero PLA parts requiring more attention due to the expansion of the material during printing.

The purpose of these operations was not to modify the final geometry of the components, but to clean the printed parts and prepare the connection interfaces for the assembly process described in Chapter 5.

Aero PLA Components

The wing tips required very little post-processing after printing. The brim was removed and the edges and visible seams were cleaned using light sanding, generally with 200–400 grit sandpaper.

The central wing sections required some additional work, particularly inside the cavities used for their connection to the fuselage. As discussed in Section 4.5.1, the expansion of Aero PLA made the removal of supports more difficult than with Basic PLA. In some areas, the walls of the supports partially fused with the surrounding printed surfaces. Despite this, the softness and higher flexibility of the material allowed the supports to be removed without damaging the wing structure.



Figure 4.15: Wing-tip connector removal

Two narrow slots were also included along the edge of each central wing to accommodate the nylon hinges used for the elevons. These slits were intentionally designed with a tight fit. Before assembly, they were progressively opened using a precision cutter until the hinges could be inserted. Small relief cuts were also introduced where necessary to facilitate insertion while maintaining a sufficiently tight fit.

A similar procedure was required at the interface between the central wing and the wing tip. In this case, the connector slot was printed with a thin layer of material closing the opening. This layer was manually removed after printing to expose the internal slot. This solution was preferred to printing the opening directly, as it reduced the expansion of Aero PLA in this region.



Figure 4.16: Insertion of hinges inside the post processed wing

Basic PLA Components

Components manufactured from Basic PLA generally required less post-processing. Brims and supports were removed where present, followed by light sanding of the surfaces and interfaces when necessary.

A more significant adjustment was required in the regions of the left and right bottom

fuselage designed to accommodate the elevon servos. These cavities were designed to provide a tight fit around the servo body. Their internal surfaces were progressively sanded until the servos could be inserted while maintaining a firm fit inside the wing.

Other Basic PLA components required only minor dimensional corrections resulting from the printing process. These adjustments were performed during preparation for assembly and mainly involved cleaning edges, removing residual support material, and lightly sanding interfaces where required.

At the end of this process, the printed components were ready for mechanical connection and avionics installation. The assembly methods used to join the different sections of the prototype are described in the following chapter.

Chapter 5

Prototype Assembly and Integration

This chapter describes the assembly and integration of the printed components presented in Chapter 4. Once the parts had been manufactured and post-processed, they had to be connected to form the complete prototype and the avionics had to be installed in their final positions.

The assembly process was considered during the CAD design from the beginning, since the different parts of the aircraft did not all require the same type of connection. Some parts were intended to remain permanently joined, while others had to be removable to provide access to the internal components, simplify transportation, or allow future modifications. That is why the connection method was selected according to the function of each joined interface rather than using the same solution throughout the aircraft.

This chapter first describes the mechanical assembly of the main structure and the installation of the control surfaces. The installation and wiring of the avionics are then presented, followed by the final assembly and the functional checks performed on the completed prototype.

5.1 Mechanical Assembly and Connection Strategy

Three main connection methods were used throughout the prototype. Components that did not need to be separated after assembly were permanently joined using cyanoacrylate (CA) glue. Removable structural connections were generally obtained using M3 screws together with metal threaded inserts, while direct screw connections into the printed PLA were used for components that were not expected to be removed frequently.

The threaded inserts used for the removable connections have a diameter of 4.25 mm and a height of 4.73 mm. They were mechanically press-fitted into the corresponding holes using pliers. The same type of insert was used for the main screwed connections of the aircraft, with the exception of the servo mounts and the GNSS installation, where the screws are inserted directly into the PLA.

The choice between permanent and removable connections depended mainly on the expected use of each interface. The connection between the central wing and the wing tip, for example, was intended to remain permanent after assembly, while the connection

between the wings and the fuselage had to remain removable. Similarly, the upper and lower fuselage sections had to be opened frequently to provide access to the avionics during installation and bench testing.

The following sections describe these connections in more detail, starting from the wing assembly and continuing with the lower and upper fuselage sections and the installation of the control surfaces.

5.1.1 Wing Assembly

Each wing is printed as two separate Aero PLA components: the central wing and the wing tip. As discussed in Chapter 4, this subdivision was mainly introduced because of the limitations of Aero PLA printing. Once the required post-processing operations were completed, the two parts were permanently joined before connecting the complete wing to the fuselage.

The connection between the central wing and the wing tip is obtained using a thin connector printed in Basic PLA. The connector is inserted into the corresponding slots present in both wing sections and bonded using cyanoacrylate (CA) glue. Basic PLA was selected for this element because it is more rigid than Aero PLA and therefore provides a stiffer connection between the two lightweight wing components.

Since there is no need to separate the central wing and wing tip after assembly, the connector and the contact surfaces between the two parts were glued permanently. The resulting assembly can now be treated as a single wing component from now on.

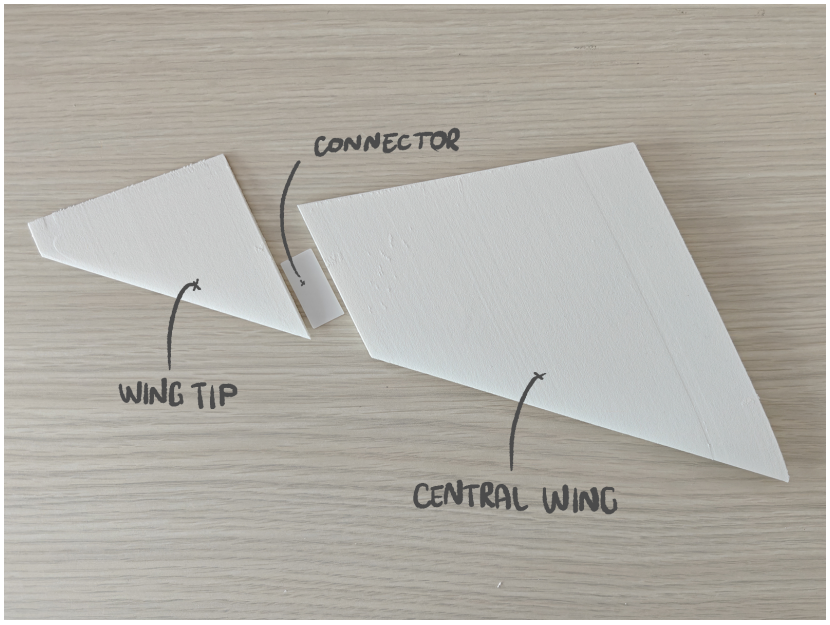


Figure 5.1: Connection between the central wing section and the wing tip.

The connection between the complete wing and the lower fuselage follows a different approach. In this case, a permanent joint was not desirable, since keeping the wings removable makes the prototype easier to access and transport. Two rectangular connectors were therefore included directly in the CAD geometry of each left and right lower fuselage section. These connectors extend inside the corresponding cavities of the Aero PLA wing and provide the main interface between the two parts.

Each connector was prepared to fit an M3 threaded insert. To maintain the alignment between the holes in the wing and the corresponding connectors, the wing was first positioned on the lower fuselage and the two parts were drilled together using a 2.8 mm drill bit.

The holes in the Basic PLA connectors were then enlarged to 4 mm before inserting the threaded inserts. Since the inserts have an external diameter of approximately 4.25 mm, the hole was intentionally kept slightly smaller to obtain a tight interference fit. The insert can accommodate this small difference during installation and was press-fitted into the PLA using pliers. This prevented the insert from moving or rotating once installed.

A corresponding opening on the bottom surface of the wing allows an M3 screw to pass through the Aero PLA and engage with the threaded insert without being visible from the top of the aircraft, as no hole is present in this surface. The screws sit flat on the surface of the wing. Two of these connections are used for each wing, one per connector.

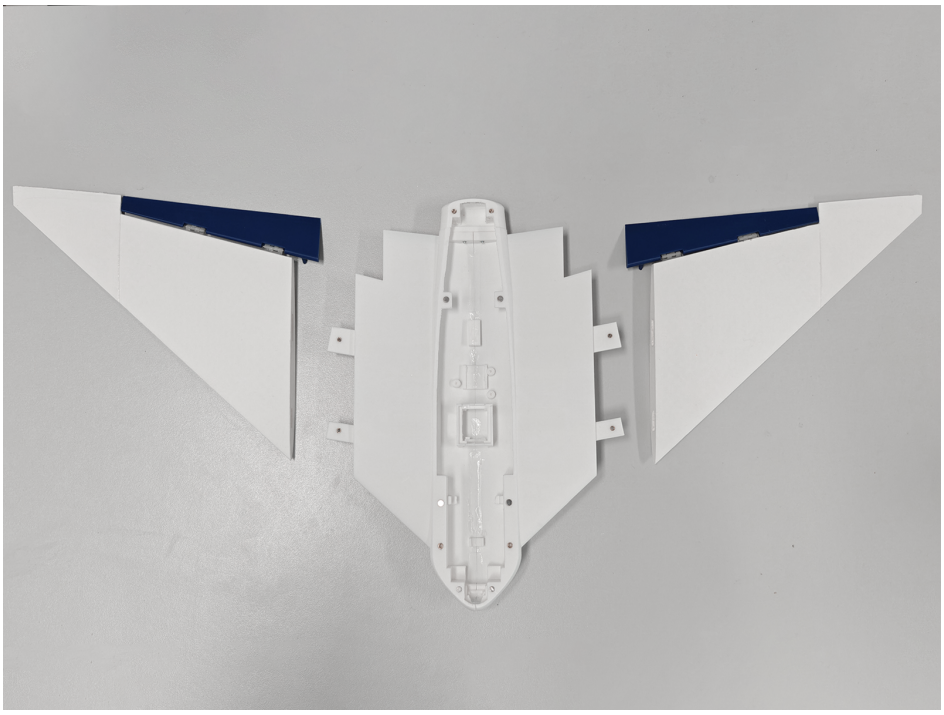


Figure 5.2: Connection between the wing and the lower fuselage section.



Figure 5.3: Final assembly of wing and fuselage connection.

This configuration provides a rigid connection during use while still allowing each

wing to be removed by unscrewing the two M3 screws. The connection also avoids relying on the Aero PLA alone for the threaded interface, since the metal inserts are instead installed in the more rigid Basic PLA structure of the lower fuselage.

The elevon servos are located in the same joining region of the lower fuselage, between the upper and lower surfaces of the wing. Although the servos were not introduced as structural components, their bodies occupy most of the local wing thickness once installed and provide some additional stiffness to this region. Their installation and connection to the control surfaces are discussed separately in Section 5.1.4.

5.1.2 Lower Fuselage Assembly

The lower fuselage is composed of three main parts: the symmetric left and right sections and the removable back bottom fuselage. The left and right sections form most of the lower structure and are permanently joined, while the rear section is connected using screws so that it can be removed if access to the release mechanism is required.

The left and right halves were joined along the aircraft centerline using CA glue. Since the direct contact area along some portions of the joining line was relatively small, additional rectangular surfaces were introduced in the CAD model to increase the available bonding area. Other structures that were already required to support internal components were also used where possible, avoiding the addition of unnecessary material only for assembly purposes.

Three alignment points were distributed along the connection, with one located toward the front, one approximately in the middle and one toward the rear. Each point uses a pair of neodymium magnets placed in matching cavities on the two fuselage halves, for a total of six magnets. The front pair makes use of the structure supporting the camera and battery, while the rear pair is integrated into the region used for the connection with the back bottom fuselage.

The magnets were mainly introduced as an assembly aid. Their attraction keeps the two halves aligned while the CA glue is applied and cured, reducing the possibility of relative movement between the parts. They remain enclosed inside the structure after bonding, although the adhesive joint itself provides the permanent connection between the two halves.

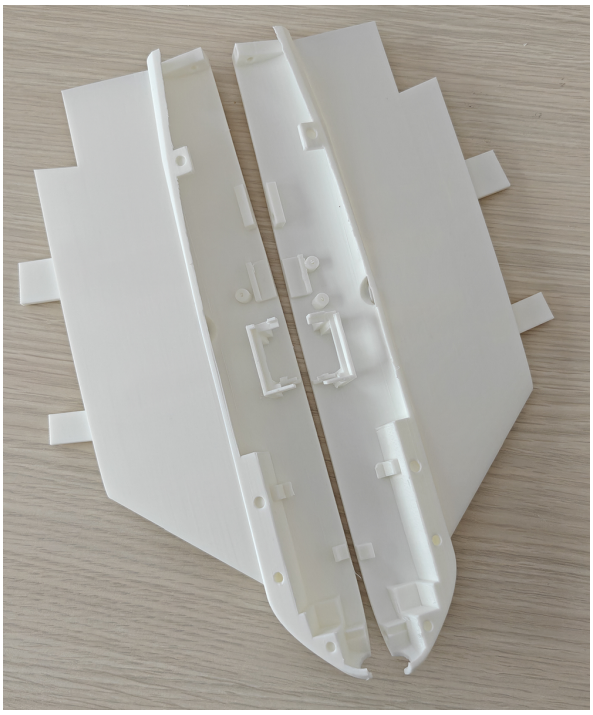


Figure 5.4: Left and Right lower fuselage before bonding.

Additional strips of Basic PLA were bonded along portions of the joining line on the internal side of the fuselage. These strips increased the surface available for the CA glue and also provided additional local stiffness after the two halves were joined. No structural testing was performed to quantify their contribution, but the assembled component was noticeably more rigid after their installation.

Once the left and right sections are joined, the back bottom fuselage can be installed. This component was intentionally kept removable because the final release mechanism was still under development and could require modifications or access to the rear section of the aircraft.

The back bottom fuselage is secured using two M3 screws. As for the wing connections described in Section 5.1.1, the screws engage with metal threaded inserts press-fitted into the corresponding Basic PLA structures. Although the rear component can be installed independently, joining the left and right fuselage sections first makes the operation easier by providing a single rigid structure to which the back section can be aligned and secured.

Two openings are also present at the rear of this component. Besides providing a possible passage for the cord associated with the release mechanism, these openings provide access to the screw connections during assembly and disassembly.



Figure 5.5: Rear bottom fuselage showing the two rear openings and screw connection.

The resulting lower fuselage can also be treated as a single structure during normal assembly, while the rear section remains accessible when required. The removable wing connections described in Section 5.1.1 are integrated directly into the left and right lower fuselage sections and are not repeated here.

5.1.3 Upper Fuselage and Main Fuselage Closure

The upper fuselage is manufactured as two separate components, the front and back top fuselage, for the printing reasons discussed in Chapter 4. Unlike the wing sections, these two parts were not permanently glued after printing. A removable connection was preferred to maintain easier access to the components installed in the upper part of the aircraft.

The two sections are connected using two M3 screws, one on each side of the fuselage. The screws are inserted from the back top fuselage towards the front where they engage with two threaded inserts that are press-fitted into the front top fuselage. The same type of threaded insert described in Section 5.1 is used for this connection.

Although the two top sections normally remain connected during assembly and operation, keeping this interface removable simplifies the installation of the Pitot tube. The Pitot is inserted longitudinally into its support from inside the front section and requires sufficient space to be correctly positioned. The nearby AirSpeed support limits the available access, so separating the front and back top fuselage provides additional

room when required. Once the Pitot is installed, the AirSpeed unit can be positioned and the two top sections can be joined again.



Figure 5.6: Front/back top fuselage connection.

The back top fuselage also contains the fin and provides the mounting region for the rudder servo and its actuation mechanism. Keeping the complete upper fuselage removable from the lower structure makes these components easier to install and access without interference from the rest of the internal avionics.

Once the front and back sections are connected, they are normally handled as a single top fuselage assembly. This complete assembly is joined to the lower fuselage using four M3 screws, with two connections located on each side of the aircraft. One connection is positioned toward the front and the other toward the rear. The corresponding threaded inserts are press-fitted directly into the lower fuselage sections.

In addition to the four screw connections, six pairs of neodymium magnets are distributed along the interface between the upper and lower fuselage. Two pairs of 4 mm magnets are located near the front of the aircraft, while the remaining four pairs use 5 mm magnets distributed further along the fuselage. Their exact position is better illustrated in Figure 5.7.

The magnets and screws serve two different purposes. During assembly and bench

testing, the magnetic connection is strong enough to keep the upper and lower fuselage correctly aligned and closed without installing the screws each time. This makes repeated access to the avionics considerably easier. The four M3 screws provide the final mechanical connection and are installed when the fuselage needs to remain securely closed, particularly for the final flight configuration.

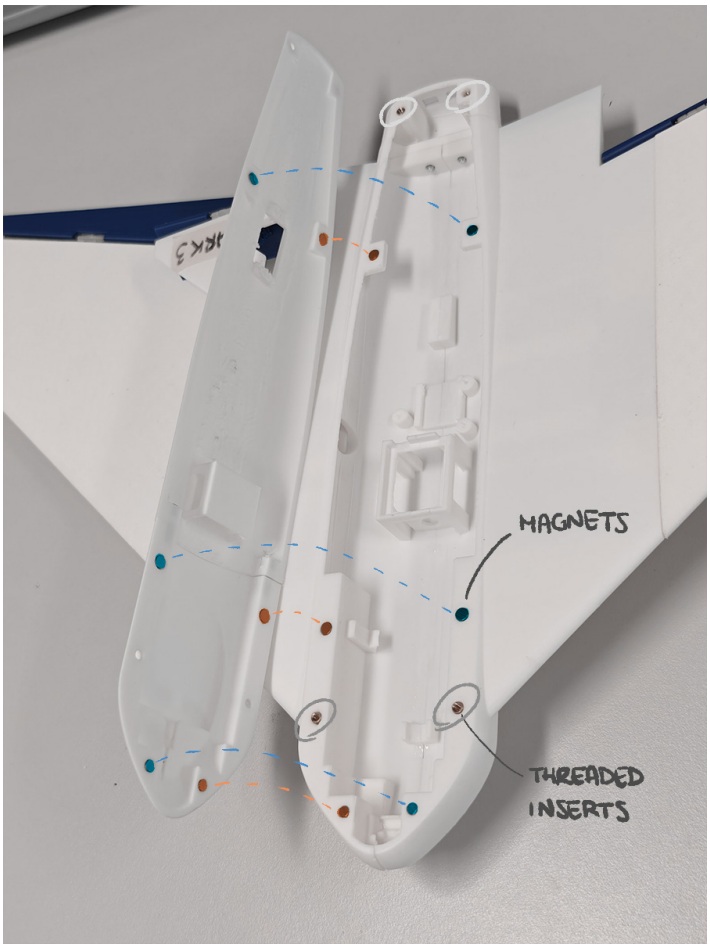


Figure 5.7: Top/bottom fuselage connection.

This combination provides a connection that is easy to open during prototype integration while still allowing the complete fuselage to be mechanically secured when required. It also avoids permanently bonding the main fuselage sections, preserving access to most of the internal avionics after the prototype has been assembled.

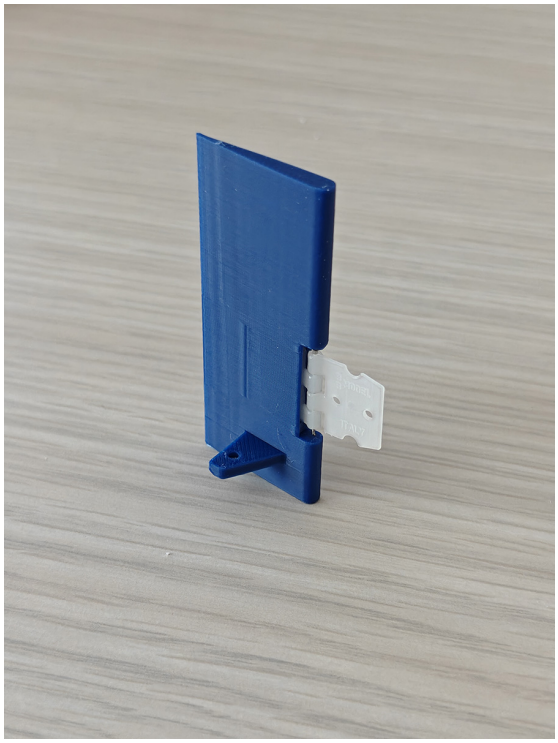
5.1.4 Control-Surface Installation and Linkages

The two elevons and the rudder are connected to the aircraft using flat nylon hinges. This solution replaced the 3D-printed pivoting mechanism used in the previous prototype and provides a simpler connection between the fixed and moving surfaces.

Each elevon uses two hinges. Both are inserted and glued with CA glue into the corresponding slots prepared in the central wing during post-processing. On the elevon side, the inner hinge is inserted into the control surface and secured with CA glue. The outer part of the elevon becomes too thin to accommodate the hinge internally, so the second hinge is instead bonded directly between its upper surface and the lower surface of the elevon.



(a) Printed Elevons without hinges.



(b) Printed Rudder with its hinge mounted.

Figure 5.8: Elevons and Rudder hinges system



Figure 5.9: Mounted Elevons on Wings.

The rudder uses the same type of nylon hinge but follows a simpler arrangement. In this case, the hinge is completely press-fitted between the rudder and the fin without additional adhesive. The fit was sufficiently tight to maintain the connection while still allowing the rudder to rotate freely.

The control surfaces are actuated using 1.5 mm stainless-steel rods connecting the servo arms to 3D-printed control horns. This type of linkage was selected because it provides a simple and rigid transmission of the servo movement, while the rod diameter was chosen to limit unwanted bending during operation.

For the elevons, one end of the rod is bent and inserted directly through the plastic servo arm. A small metal retaining element is added at this connection to prevent the rod from slipping out during movement. The opposite end passes through an adjustable connector installed on the 3D-printed control horn. An M3 screw on the connector can be loosened to move the rod before tightening it in the required position. This makes it possible to adjust the neutral position of the elevon mechanically without modifying the linkage itself.

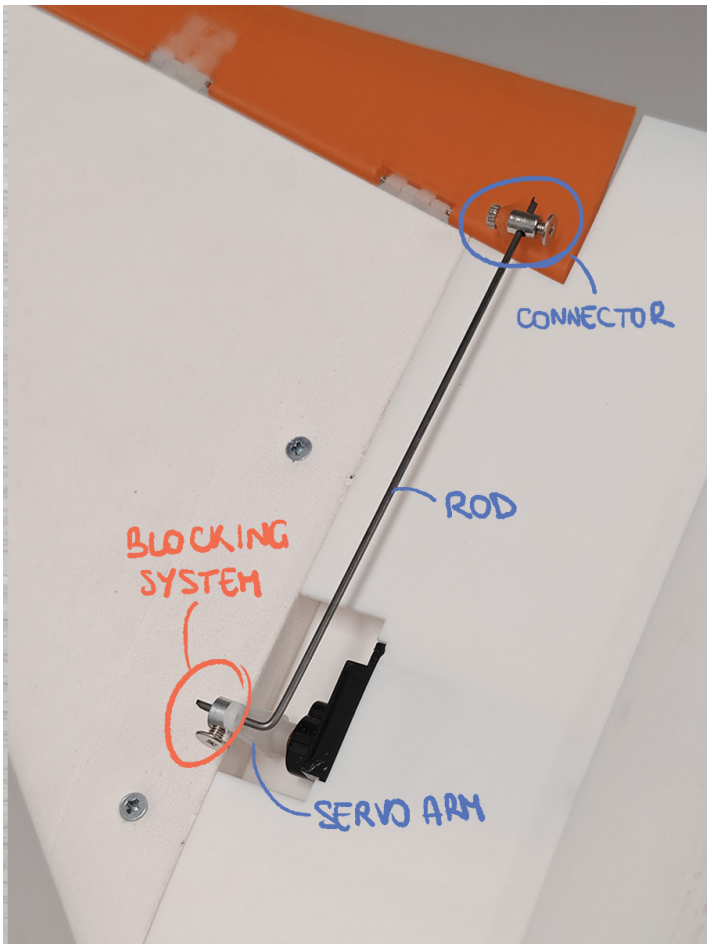


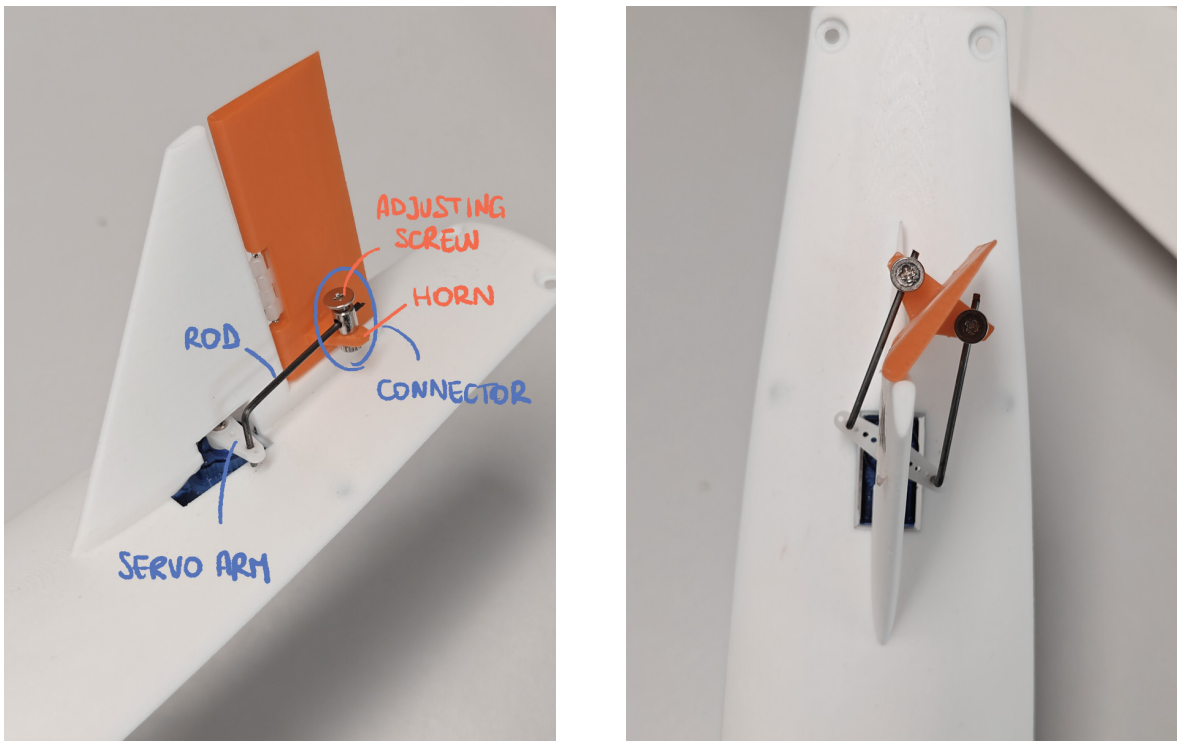
Figure 5.10: Elevons actuation system.

The elevon servos are press-fitted into the cavities prepared in the left and right lower fuselage sections. The tight fit already limits movement of the servo body, while two additional mounting screws, supplied with the servos, secure each unit directly to the printed PLA structure.

The control horns also required an iteration during the assembly process. Initial functional checks showed that the first geometry limited the available movement of the elevons. The final horn was moved closer to the elevon hinge line and made slightly taller, while its thickness was reduced. These changes increased the available control-surface excursion while also reducing the amount of material required for the horn.

The rudder uses the same general linkage principle, but with a symmetric arrangement. The servo is mounted directly to the back top fuselage using its supplied mounting screws and a double-sided servo arm protrudes from the upper fuselage near the base of the fin. Two separate 1.5 mm steel rods connect the servo arm to two control horns located on opposite sides of the rudder. Each rod uses the same adjustable connector adopted for the elevons, allowing the linkage position to be set before tightening the

M3 screws.



(a) Side view with notes.

(b) Top view.

Figure 5.11: Rudder actuation system.

After installation, the servos were actuated to verify the movement of the three control surfaces and to check for interference throughout their available range. This check also led to the control-horn modification described above. The final configuration allowed the elevons and rudder to move correctly while keeping the linkage simple and mechanically adjustable.

5.2 Avionics Installation and Wiring

Once the main structure and control surfaces were assembled, the avionics components could be installed in the positions defined during the CAD design process. The reasons behind the final layout were discussed in Chapter 3; this section focuses instead on how the individual components were physically mounted and connected inside the prototype.

Due to the limited internal volume of the glider, most of the mounting solutions were kept simple and made use of supports and cavities already included in the CAD model. Particular attention was given to keeping the components accessible and removable when possible, since several of them may need to be disconnected during assembly or

maintenance. The installation of the servos has already been discussed in Section 5.1.4 and is therefore not repeated here.

FCC and Battery Installation

The Flight Control Computer (FCC) is positioned close to the center of gravity on the elevated support introduced in Chapter 3. The support raises the board above the lower fuselage, leaving part of the volume underneath available for other components. An opening was also included in the supporting surface so that the FCC rests on a limited contact area rather than directly on a completely solid platform.

The FCC does not provide dedicated mounting holes that could be used to screw it directly to the printed structure. For this prototype, a simple removable fastening method using zip ties was therefore preferred. This avoids the need for a more complex 3D-printed mounting mechanism and allows the board to be removed without modifying the component itself. The mounting solution can also be changed in future iterations without requiring a significant redesign of the surrounding structure.

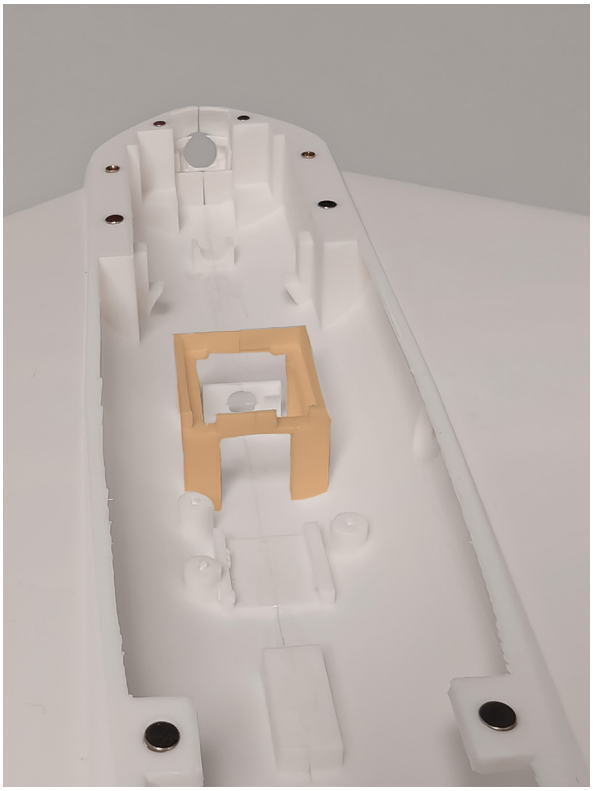


Figure 5.12: Elevated support for mounting the FCC highlighted in orange.

The battery is positioned directly in front of the FCC and behind the camera. Unlike the FCC, it does not require an additional fastening system. Its cavity constrains

its movement inside the lower fuselage, while the wiring located behind it prevents significant movement towards the rear of the aircraft.

When the upper fuselage is installed, the internal surface above the battery provides an additional vertical constraint by slightly pressing against it. The battery is therefore enclosed between the surrounding geometry and the upper fuselage and cannot leave its position once the aircraft is closed.

This arrangement also keeps the battery easy to access. Once the upper fuselage is removed, the battery can be taken out directly without removing screws, adhesive or other mounting elements. This is particularly useful since the battery is one of the components that may need to be removed or replaced most frequently during operation.

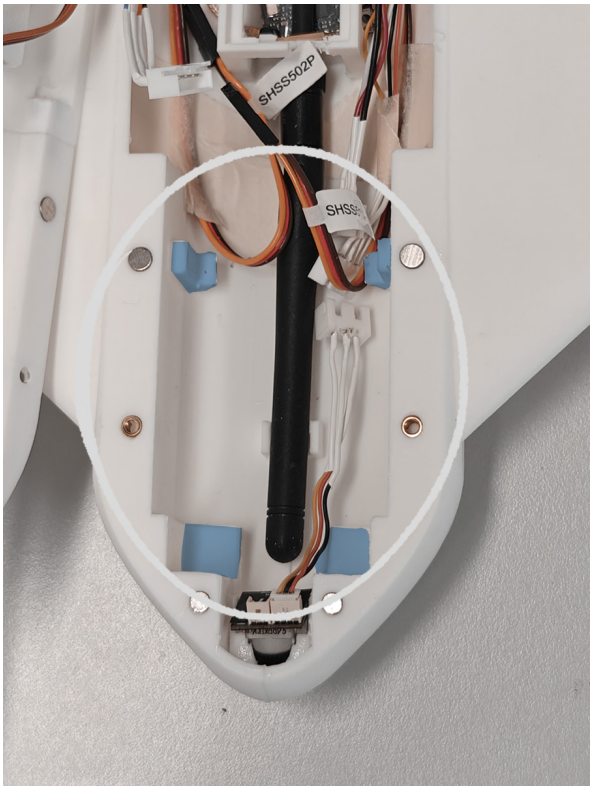


Figure 5.13: Battery cavity and its support highlighted in blue.

Pitot and AirSpeed Installation

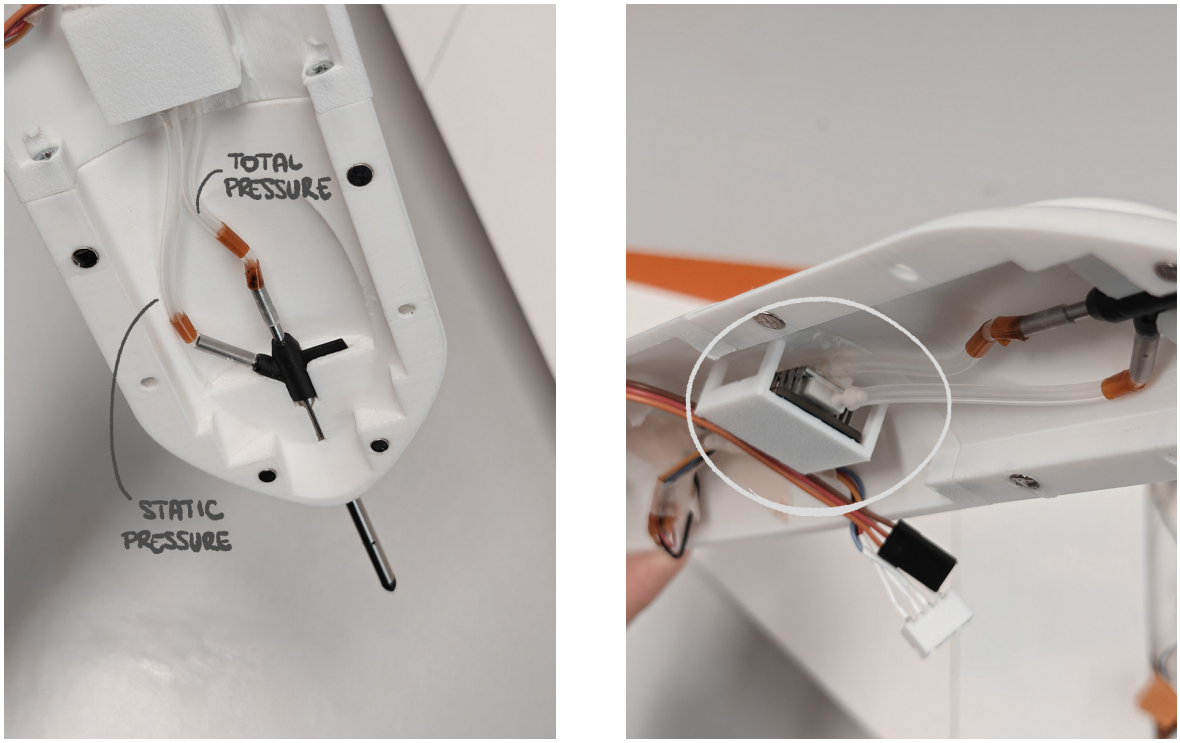
The Pitot tube is installed from the inside of the front top fuselage and is held in position through a press fit with the surrounding printed geometry. No screws or adhesive are required for this connection.

The main cylindrical body of the Pitot provides the primary support, while a second rectangular feature is enclosed by the surrounding PLA geometry and prevents the component from rotating once installed. Both pressure connections remain accessible

from inside the fuselage and are connected to the AirSpeed module through two flexible pressure tubes.

The AirSpeed module is positioned above the FCC and is also press-fitted into a dedicated support integrated into the upper fuselage. This position keeps the module close to the Pitot and allows the two pressure tubes to follow a relatively short path without requiring sharp bends. This is particularly important for the pressure lines, which should remain free from unnecessary folding or obstruction.

As discussed in Section 5.1.3, the Pitot is installed before the AirSpeed module. The Pitot first needs to be slid into its support from inside the front top fuselage, after which the pressure tubes can be connected and the AirSpeed module can be inserted into its corresponding support. The electrical connection between the AirSpeed module and the FCC is then made through its existing connector.



(a) Assembled Pitot. (b) Assembled AirSpeed reader.

Figure 5.14: Pitot and AirSpeed assembled.

Camera and Video Transmission System

The camera is installed at the front of the lower fuselage using a dedicated holder designed around its external geometry. Rather than integrating the holder directly into the fuselage, it was printed as a separate component and subsequently bonded to the

front opening using CA glue. The camera can then be fitted directly into this support.

The geometry of the holder defines the downward inclination introduced during the CAD redesign, so no additional adjustment of the camera angle is required during installation. Manufacturing the holder separately also made it easier to obtain the required fit without modifying the complete lower fuselage. In a future configuration where the lower fuselage could be manufactured as a single component, the same support geometry could potentially be integrated directly into the main structure.

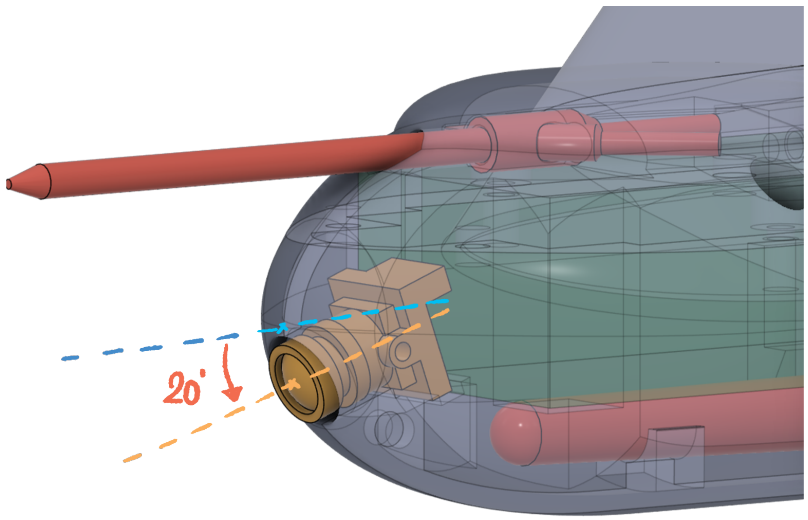
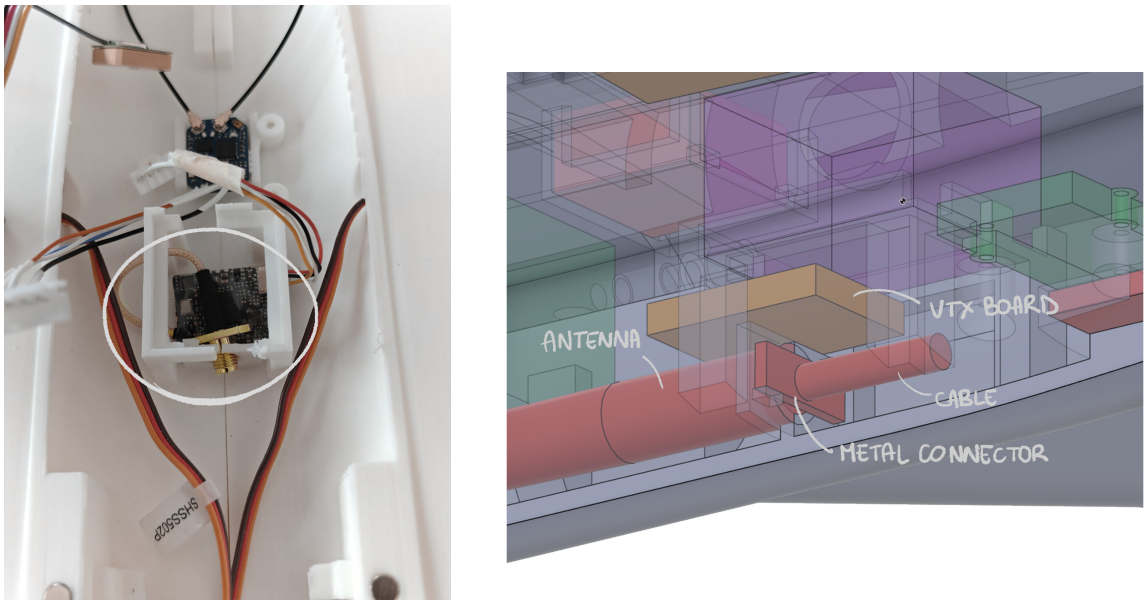


Figure 5.15: Camera downward angle.

The video transmission antenna is installed inside the front part of the lower fuselage. Its connection required a different mounting solution because the antenna needs to remain firmly positioned while still being connected to the VTX board through its original threaded connector.

A rectangular support with a central hole was therefore included in the CAD model. The threaded antenna connector passes through this opening, while the antenna is screwed onto the connector from the opposite side. The two sides of the connector capture the printed support between them, preventing the connection from moving inside the fuselage without requiring an additional fastening element.

The VTX board itself is positioned below the FCC in the space made available by its elevated support. The available internal volume limits its movement once the aircraft is assembled, although additional adhesive retention can be introduced if required.



(a) VTX board and metal connector inserted.

(b) VTX Antenna mount CAD view.

Figure 5.16: VTX and its antenna mounted.

ELRS and GNSS Installation

The ELRS system and GNSS are both installed in the rear portion of the fuselage. Their final positions and the reasons for their relocation were discussed in Chapter 3; the mounting solutions themselves were kept relatively simple.

The ELRS unit is press-fitted into a dedicated region of the lower fuselage. Its two telemetry antennas are positioned along the internal surfaces and secured using adhesive tape. Their orientation is maintained approximately towards the front and outside of the aircraft, as defined by the final avionics layout.

The GNSS board uses a different mounting method because three mounting holes are already available on the board. Dedicated supports were included in the CAD model and the unit is secured directly to them using three M2 screws with a length of 6 mm. Unlike the main structural screw connections, no threaded metal inserts are required for this installation, since the screws engage directly with the printed PLA.

The GPS antenna remains connected to the GNSS through its original cable and is positioned further towards the rear of the aircraft. It is secured to the internal surface using adhesive tape, keeping the installation simple while maintaining the antenna in its intended position.

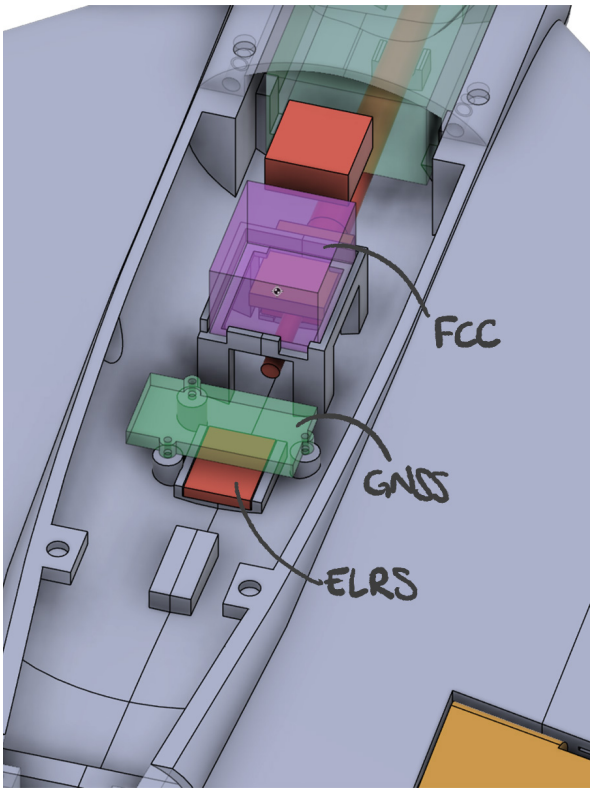


Figure 5.17: GNSS and ELRS CAD view.

Electrical Connections and Cable Management

Most of the avionics were inherited from the previous prototype with their electrical connections already installed. During the integration of the new configuration, the main objective was therefore to adapt the existing wiring to the reduced internal space while keeping the individual components easy to disconnect when required.

With the exception of the battery connection, the avionics use JST-XH connectors for their connection to the FCC. This allows the individual systems to be disconnected without permanently modifying the wiring and simplifies access when the upper fuselage or other removable components need to be taken apart. The FCC also provides four dedicated servo ports used for the control-surface actuators.

The routing of the elevon-servo cables required a small modification because of the limited space available between the servo body and the surrounding wing geometry. The lower part of the servo casing was locally opened so that the cable could leave the unit directly from the bottom rather than being compressed against the wing surface. The cables then pass into the fuselage through openings already included in the CAD geometry.

The rudder servo and AirSpeed module are both installed on the removable upper

fuselage. Their cables are routed along the internal surface of the upper structure, with enough free length left close to the FCC to allow the connectors to be reached when the fuselage is opened. The upper section can therefore be lifted sufficiently to disconnect these components before being completely removed.

The internal supports and component positions were designed while leaving additional clearance for the wiring. This reduced interference between the cables and the avionics and made it possible to close the fuselage without significantly compressing the connections.

Some cable lengths were also reduced during integration to better match the new component positions. A small number of electrical connections required resoldering after being damaged or disconnected while rearranging the avionics. These operations were performed with assistance and did not involve a redesign of the original electrical architecture.

For the current prototype, excess wiring is secured against the internal surfaces using adhesive tape. This provides a simple method of preventing loose cables from interfering with the components or the fuselage closure while still allowing the wiring to be accessed and rearranged when required.

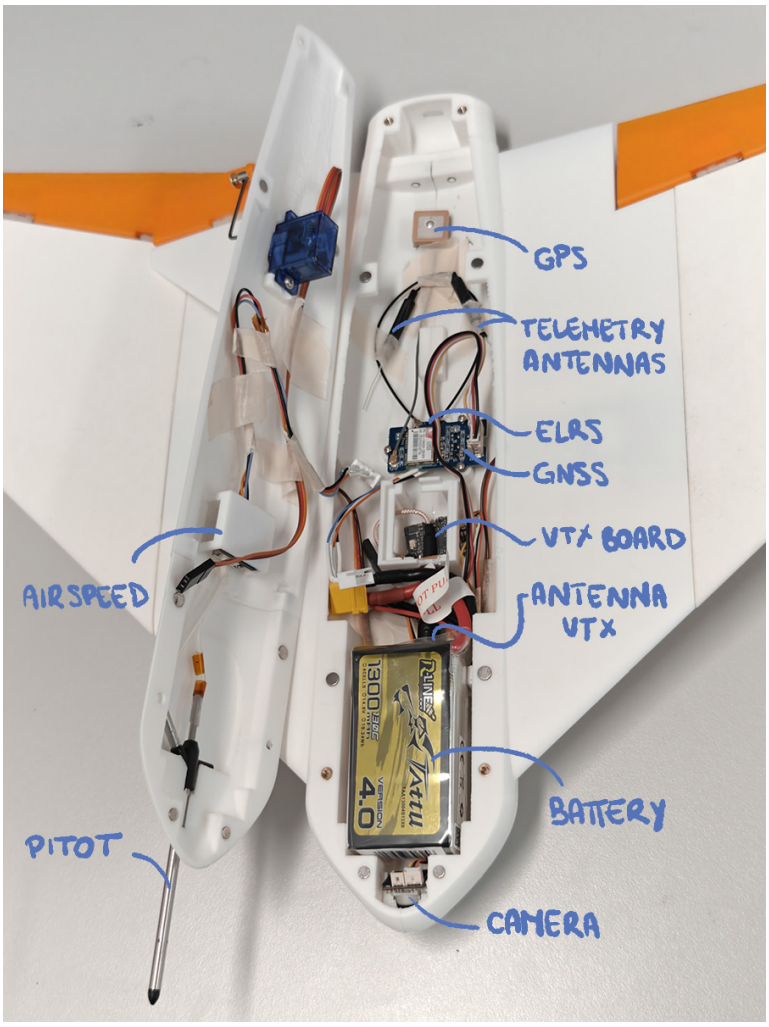


Figure 5.18: Final Assembly of Avionics inside the Space Dart.

The resulting installation keeps the main avionics accessible and individually detachable while fitting the complete system within the limited internal volume of the prototype. This was particularly useful during assembly, since individual components could be removed or repositioned without requiring the complete wiring system to be disassembled.

5.3 Final Prototype and Functional Checks

After completing the mechanical assembly and installing the avionics, the prototype was assembled in its final configuration. At this stage, the main removable connections were checked to verify that the different sections could be correctly aligned, secured and accessed when required.

Basic functional checks were also performed before proceeding to the testing phase. The three servos were actuated to verify the movement of the two elevons and the

rudder, checking that the linkages could move through their available range without interfering with the surrounding structure. The adjustable rod connections also allowed small corrections to the neutral position of the control surfaces when required.

The installation of the avionics was checked with the fuselage both open and closed to ensure that the internal components and wiring did not interfere with the assembly. Particular attention was given to the cables connected to the removable upper fuselage, since the rudder servo and AirSpeed module need to remain accessible when the aircraft is opened.

These operations were intended as integration checks rather than a complete characterization of the individual avionics components. Most of the electronic systems were inherited from the previous prototype and had already been tested during the previous work. The checks performed at this stage were therefore mainly aimed at verifying their correct installation within the new configuration.



Figure 5.19: Space Dart prototype and its back-up shell.

The completed prototype shown in Figure 5.19 represents the final configuration obtained from the CAD redesign, manufacturing and assembly processes described in the previous chapters. With the mechanical structure completed and the main systems integrated, the prototype provides the basis for the first flight-test phase of the project. The following chapter therefore proposes the setup and methodology that could be used for these tests.

Chapter 6

Proposed Flight-Test Methodology

The development, manufacturing and integration activities described in the previous chapters resulted in a complete Space Dart prototype that provides the basis for the first flight-test phase. However, the final release system and the complete flight-test setup were not finalized within the time available for this thesis, and a complete flight campaign could therefore not be carried out. For this reason, this chapter proposes a methodology that could be followed in a future test campaign to evaluate the dynamic behaviour of the manufactured glider.

The main purpose of the proposed tests is to compare the response of the physical prototype with the theoretical dynamic behaviour presented in Section 2.2.2. In particular, the test campaign focuses on the Phugoid and Dutch-roll modes, which can be excited during flight and identified from the resulting response of the aircraft.

The following sections describe the proposed flight-test setup and procedure, the manoeuvres used to excite the two dynamic modes, and the data that should be recorded during the tests. A simple approach for comparing the experimental response with the theoretical predictions is then introduced, together with the main limitations of the proposed methodology and possible future developments.

6.1 Objectives of the Flight Tests

The main objective of the proposed flight tests is to evaluate whether the dynamic behaviour of the manufactured Space Dart is consistent with the theoretical predictions presented in Section 2.2.2. The tests are therefore not intended to provide a complete aerodynamic characterization of the aircraft, but rather a first experimental validation of its dynamic response.

The proposed test campaign focuses on the Phugoid and Dutch-roll modes. These two oscillatory modes can be excited during flight through specific control inputs and their response can then be observed after the controls are returned to their neutral position. This makes it possible to compare the behaviour of the physical prototype with that predicted by the aerodynamic model.

For each mode, the main quantities considered for the comparison are the oscillation period and the damping ratio. The oscillation period describes how quickly the aircraft

completes one cycle of the motion, while the damping ratio indicates how rapidly the oscillation decreases with time. These parameters can be obtained from the recorded flight response and compared with the corresponding theoretical values already presented in Section 2.2.2.

Since the first proposed tests would be performed at relatively low altitude, the experimental results should be compared with the theoretical predictions obtained for sea-level conditions. The behaviour predicted for the final stratospheric operating condition at approximately 20 km cannot be directly validated through this initial test campaign, since the atmospheric conditions and the resulting aircraft dynamics are significantly different.

The flight tests therefore have the following main objectives:

- verify that the manufactured prototype shows the expected Phugoid and Dutch-roll responses;
- estimate the period and damping of the two modes from the recorded flight data;
- compare the experimental results with the corresponding theoretical predictions;
- identify possible differences that could be investigated in future tests or used to improve the theoretical model.

6.2 Flight-Test Setup and Procedure

The proposed flight test requires the Space Dart to be carried to a suitable altitude by a separate drone and released before starting the dynamic-mode excitation. The complete test therefore involves not only the glider itself, but also the carrier drone, the release system and the ground equipment required to control and monitor the flight.

Test Setup

The exact model of the carrier drone is not a defining element of the proposed methodology, provided that it can safely carry the Space Dart to the required altitude while maintaining a reliable connection with its pilot. The tests should be performed in a sufficiently large and unobstructed area, allowing enough space for the carrier-drone climb, the free flight of the glider and its final landing.

At least three operators are required for the proposed test. One pilot is dedicated to the carrier drone, while a second pilot controls the Space Dart after release. A third operator manages the ground equipment, including the video reception through the directional Yagi antenna and the computer used for monitoring and recording the

available flight data. This separation of tasks allows the Space Dart pilot to concentrate on the excitation manoeuvres and on the recovery of the aircraft.

Suitable weather conditions are also important for the test. In particular, strong or changing wind should be avoided, since it could affect both the safety of the operation and the dynamic response being observed. Temperature and the general atmospheric conditions should also be considered when selecting the test day.

Before each flight, a short functional check should be performed on the complete system. The main checks should include the battery charge level, correct movement of the control surfaces, operation of the manual and stabilized flight modes, radio and telemetry connections, GNSS reception, video transmission and correct operation of the selected release system.

Release System

The release system represents one of the elements of the test setup that is still under development. An initial passive solution was investigated, but it did not provide sufficient reliability for the planned flight tests. For this reason, different alternatives are currently being considered.

One possibility is the use of an off-the-shelf release device installed directly below the carrier drone. The Space Dart would be connected to the device through a cord. The device contains its own sensors and can detect a predefined sequence of rotations performed by the carrier drone, after which the cord is released. The main advantage of this solution is that the release function remains independent from the Space Dart avionics and does not require additional components to be installed inside the glider.

A second solution currently being tested is based on a thermocutter installed inside the Space Dart. In this case, the glider would be connected to the carrier through a nylon cord, which would be cut when the release is commanded. Although this solution provides direct control of the release from the glider, it introduces some additional practical problems. Cutting the cord requires a certain amount of time and electrical energy, and the thermocutter must be mounted so that the suspended weight of the glider is transferred to the structure rather than directly to the flight-control electronics. Its position would also introduce additional mass towards the rear of the aircraft, which was not included in the current mass distribution and could affect the centre of gravity presented in Section 3.5.

For these reasons, the final release solution has not yet been selected. The drone-mounted device appears attractive because it requires fewer modifications to the Space Dart itself, while the thermocutter remains under testing to evaluate its reliability.

Regardless of the final solution, the release system should provide a reliable separation while introducing as little disturbance as possible to the initial motion of the glider.

Proposed Flight Sequence

During the climb, the Space Dart would be carried with its nose pointing downwards. After release, this orientation allows the glider to enter a short dive and gain the airspeed required for flight. The Space Dart pilot would then progressively bring the aircraft to a stable, approximately horizontal glide condition before starting the dynamic test.

A release altitude in the order of 200–250 m is considered as a preliminary target for the first tests. This value has not been obtained from a detailed calculation and should therefore not be interpreted as a minimum required altitude. The actual altitude must provide enough space to complete the initial acceleration, establish a stable glide, perform the selected excitation manoeuvre, observe the resulting free response and finally recover the aircraft before landing.

Once a stable glide has been reached, the Space Dart would be operated in manual mode for the excitation manoeuvre. In this mode, the pilot can command the control surfaces without the additional coupled corrections introduced by the stabilized mode. This is important because automatic corrections during the free response could modify the natural motion that the test is intended to observe.

After the excitation input, the controls would be returned to their neutral position and the resulting motion would be allowed to develop freely. If the aircraft naturally returns towards a stable flight condition, the pilot can continue the recovery manually. If the response becomes difficult to control, the stabilized mode can be activated instead to assist the pilot in recovering the aircraft. The stabilized mode is not used as an autopilot, but introduces additional control corrections to reduce unwanted motions and help maintain a stable flight condition.

The complete proposed sequence can therefore be summarized as: carrier-drone climb, release, initial dive and acceleration, establishment of a stable glide, manual excitation, observation of the free response, recovery and final landing. The objective is to recover the prototype without damage so that additional manoeuvres and repeated flight tests can be performed.

6.3 Dynamic-Mode Excitation

The manoeuvres proposed in this section are based on standard flight-test procedures for the excitation of aircraft dynamic modes. In particular, the adopted inputs and the

general sequence of excitation followed by free response are consistent with the methodology described in *Flight Vehicle System Identification: A Time-Domain Methodology* book [13].

The dynamic behaviour of the Space Dart can be investigated by deliberately exciting the modes of interest and then observing the resulting free response of the aircraft. For the proposed tests, the excitation should be applied only after a sufficiently steady glide condition has been reached, as described in Section 6.2.

During each manoeuvre, the aircraft should remain in manual mode so that the pilot can command the required control surface independently. Once the excitation has been completed, the controls should be returned to their neutral position and the pilot should avoid any further correction for as long as the response remains safe. This free-response phase is the part of the manoeuvre used to identify the natural dynamic behaviour of the aircraft.

Only one type of manoeuvre is proposed for each flight, particularly during the first test campaign. This simplifies both the preparation of the test and the interpretation of the recorded data. If possible, the same manoeuvre should be repeated at least three times under similar conditions, either during separate flights or, if sufficient altitude remains, within the same flight. Repetition is useful to verify that the observed response is consistent and is not dominated by a single disturbance or pilot input.

Phugoid

The Phugoid is a slow longitudinal oscillation mainly characterized by an exchange between airspeed and altitude. During the motion, the aircraft alternately climbs and slows down, and then descends and accelerates, while the pitch attitude changes more slowly than in the short-period mode.

For the Space Dart, the Phugoid can be excited through a short symmetric input of the two elevons. Since the aircraft does not have an engine, the alternative use of a thrust variation is not possible. An elevator-type pulse is therefore the simplest solution for the proposed test. This type of input is also commonly used to excite the Phugoid mode.

The manoeuvre should begin from a stable glide with the aircraft approximately aligned with its flight path. The pilot should then apply a short positive pitch command by moving both elevons upward together. This produces a nose-up pitching moment and increases the pitch attitude of the glider. The exact control amplitude is not defined at this stage and should be selected during the first practical tests. It should be large enough to produce a clearly measurable response, while remaining small enough to

avoid excessive departure from the normal flight condition.

After the short input, the pilot should return the pitch command to neutral and avoid further control corrections. The initial nose-up motion causes the aircraft to gain altitude while losing airspeed. As the airspeed decreases, the aircraft should progressively lower its nose and begin descending again. During the descent, airspeed increases, leading to the next part of the oscillation. This repeated exchange between kinetic and potential energy produces the characteristic Phugoid response.

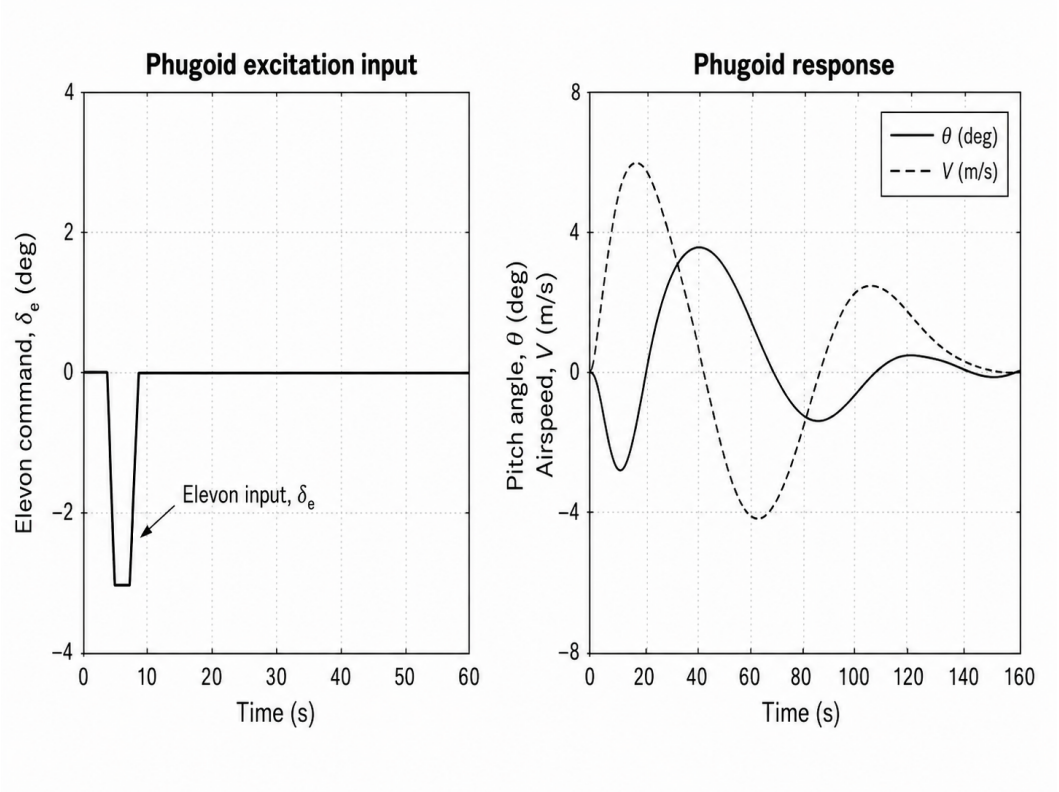


Figure 6.1: Qualitative control input and expected response during the Phugoid manoeuvre.

The pilot should leave the controls neutral for at least one complete oscillation whenever the available altitude permits it. One full Phugoid cycle is generally sufficient for an initial estimation of its dynamic parameters, while observing additional cycles would improve the quality of the comparison. If the aircraft begins to depart significantly from a safe flight condition, the free-response phase should be interrupted and the pilot should regain control, using the stabilized mode if necessary.

For the final aerodynamic configuration, the theoretical sea-level Phugoid properties presented in Section 2.2.2 are

$$T = 12.405 \text{ s}, \qquad t_{1/2} = 13.787 \text{ s}, \tag{6.1}$$

$$\omega_n = 0.508 \text{ rad/s}, \qquad \zeta = 0.098, \tag{6.2}$$

with the corresponding eigenvalues

$$\lambda = -0.050 \pm 0.506i. \tag{6.3}$$

Here, T represents the time required to complete one oscillation, while $t_{1/2}$ is the time required for the oscillation amplitude to reduce to half of its initial value. The natural frequency ω_n describes the characteristic frequency of the mode, and the damping ratio ζ indicates how rapidly the oscillation decreases with time. Since the predicted damping ratio is relatively low, the Phugoid is expected to remain visible for more than one oscillation if sufficient altitude is available.

Dutch Roll

The Dutch-roll mode is a coupled lateral-directional oscillation involving both yaw and roll. After being disturbed laterally, the aircraft does not simply rotate around the vertical axis. The yawing motion produces a sideslip, which in turn generates aerodynamic forces and moments that also produce a rolling motion. The result is an oscillation in which yaw and roll develop together.

For this mode, the proposed excitation is a rudder doublet. A doublet consists of a short rudder input in one direction, immediately followed by an approximately opposite input, after which the rudder is returned to neutral. A simple rudder doublet is commonly used to excite Dutch-roll motion and is considered sufficient for this type of test.

Starting again from a stable glide condition, the pilot should keep the elevon command as close to neutral as possible and apply the doublet using only the rudder control. For example, the pilot may first command the rudder to one side, then move it to the opposite side for a similar short duration, and finally return the stick to its central position. The exact amplitude and timing should be established during preliminary testing rather than fixed in advance.

The first rudder input produces a yawing motion and generates sideslip. The opposite input then changes the direction of the yawing motion and provides the second part of the excitation. Once the rudder is returned to neutral, the aircraft should be allowed to respond freely. Because yaw and roll are coupled, the expected response is an alternating lateral motion in which the nose moves from side to side while the aircraft also develops a corresponding oscillation in bank angle.

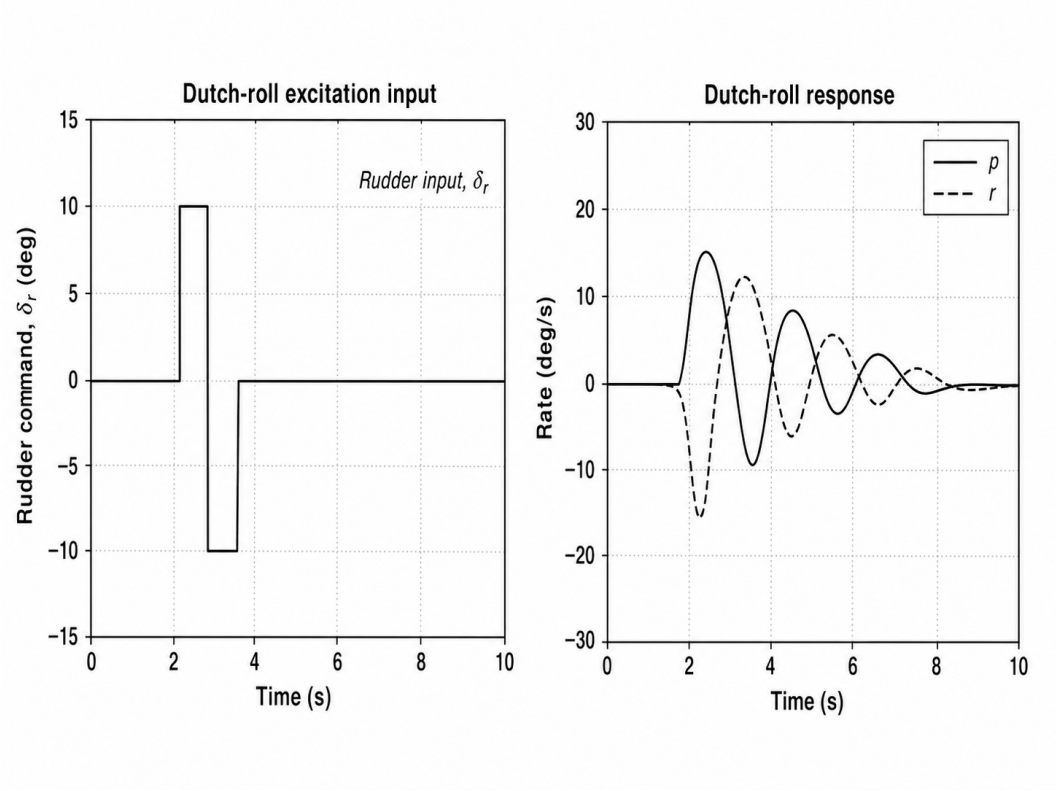


Figure 6.2: Qualitative rudder doublet and expected coupled yaw–roll response.

During the free response, the pilot should not introduce additional rudder or elevon corrections unless the aircraft begins to leave a safe flight condition. This is particularly important because simultaneous control inputs would make it more difficult to separate the natural Dutch-roll response from the effect of the pilot. Flight-test practice also recommends using independent control inputs where possible for this reason.

For the final configuration, the predicted sea-level Dutch-roll properties are

$$T = 3.180 \text{ s}, \qquad t_{1/2} = 0.349 \text{ s}, \tag{6.4}$$

$$\omega_n = 2.794 \text{ rad/s}, \qquad \zeta = 0.707, \tag{6.5}$$

with the corresponding eigenvalues

$$\lambda = -1.975 \pm 1.976i. \tag{6.6}$$

Compared with the Phugoid, the Dutch-roll motion is therefore expected to be much faster and much more strongly damped. The predicted period is only about 3.2 s, while the short value of $t_{1/2}$ indicates that the oscillation amplitude should decrease rapidly after the control input. For this reason, the useful part of the measured response may

be limited to only a few seconds.

The response should be recorded for as long as the oscillation remains distinguishable. If sufficient altitude is still available after recovery, the manoeuvre may be repeated during the same flight; otherwise, additional runs should be performed on following flights under similar conditions. As for the Phugoid test, the manoeuvre should be interrupted whenever the aircraft approaches an unsafe condition or the remaining altitude becomes insufficient for a safe recovery.

For both manoeuvres, the commanded control inputs can be obtained from the RadioMaster telemetry log and used to identify the beginning, duration and approximate magnitude of the excitation. These signals represent the commands sent to the servos and should not be interpreted directly as measurements of the physical control surface deflection. If required, the relationship between commanded servo signal and actual elevon or rudder angle can be determined separately through a bench calibration before the flight campaign.

6.4 Data Acquisition and Comparison

The dynamic response described in the previous section has to be recorded with enough information to identify the manoeuvre and observe the motion of the aircraft after the control input. The proposed data-processing approach is intentionally kept simple, since the objective of the test is to obtain a first comparison with the theoretical dynamic properties rather than perform a complete aerodynamic system identification.

The general approach adopted in this section follows the flight-test data-processing principles described in [13]. In particular, the recorded signals should first be checked for consistency and possible errors before being used to estimate the characteristics of the aircraft response.

Data Acquisition

The main source of quantitative flight data is the telemetry generated by the onboard avionics. Measurements collected by the sensors are processed by the Matek F411-WTE flight-control computer running iNav [14] [15] and transmitted to the ground through the ELRS telemetry link [16]. The RadioMaster controller [17] receives these data and stores them on its microSD card as a time-stamped log [18].

The video system operates independently from this telemetry chain. The onboard camera sends the video signal through the VTX and its dedicated antenna, while the signal is received on the ground through the directional Yagi antenna. The video can

therefore be used as an additional visual reference for the flight, but it is not intended to replace the quantitative telemetry data used for the dynamic analysis.

For the proposed tests, the useful recorded quantities include:

- time stamp, used as the common time reference for the recorded signals;
- pitch, roll and yaw angles, used to observe the attitude response of the aircraft;
- altitude and vertical speed, useful for following the vertical motion of the glider;
- Pitot airspeed, used to observe the variation in airspeed during the manoeuvre;
- GPS ground speed, position and heading, used to follow the general trajectory of the aircraft;
- commanded elevon and rudder inputs, used to identify the beginning and duration of each excitation;
- GNSS and telemetry quality information, useful for identifying periods in which the recorded data may be less reliable.

Together, these quantities provide a description of the main evolution of the flight and of the aircraft attitude during the excitation and free-response phases. However, they should not be considered equivalent to a complete flight path reconstruction. More advanced reconstruction methods generally also use linear accelerations and angular rates to estimate the aircraft states through the kinematic equations of motion [13].

The current RadioMaster logging configuration [19] provides samples at approximately 10 Hz. This corresponds to a time interval of approximately

$$\Delta t \simeq 0.1 \text{ s}. \tag{6.7}$$

For the predicted Phugoid period of approximately 12.4 s, this provides more than one hundred samples over a complete oscillation and should therefore allow the slow response to be clearly observed. The Dutch-roll period is much shorter, approximately 3.2 s, corresponding to only around thirty samples per cycle. The available sampling frequency is therefore more limiting for the Dutch-roll test, particularly because this mode is predicted to decay rapidly.

Preliminary Data Processing

Before extracting the dynamic parameters, the recorded data should first be checked and the part corresponding to the manoeuvre should be isolated. Flight-test data can

contain measurement noise, offsets, missing samples and time delays, and checking the consistency of the recorded channels before the analysis is therefore an important preliminary step [13].

For the proposed tests, the processing can remain limited to a few basic operations. First, the time interval containing the control input and the following free response should be identified from the recorded servo command. The time stamps should then be checked to verify that the sampling interval remains approximately constant and that no significant portions of data are missing.

The aircraft condition immediately before the excitation can be used as the reference condition. If necessary, a constant offset can be removed from the response so that the oscillation is considered relative to this initial condition. Obvious isolated measurement errors can also be identified before plotting and analysing the response. No advanced filtering method is defined at this stage, since the amount of processing required can only be evaluated once actual flight data are available.

The recorded control channels represent the commands sent to the servos and not a direct measurement of the physical angle of the control surfaces. If a more accurate relation between the excitation command and the actual surface deflection is required, a separate bench test can be performed before the flight campaign. In this test, different recorded servo command values can be associated with measured elevon and rudder angles. This is particularly useful because control inputs cannot generally be verified from the aircraft motion alone and therefore require an independent calibration. [13]

The Pitot airspeed and GPS ground speed should also be treated as different quantities. The Pitot system measures the velocity of the aircraft relative to the surrounding air, while GPS provides its velocity relative to the ground. The two values may therefore differ in the presence of wind and should not be expected to coincide during the complete test.

Extraction of the Dynamic Parameters

Once the manoeuvre interval has been selected, the period and damping of the response can be estimated from the oscillating signals. For the Phugoid, the pitch angle, altitude and airspeed provide complementary information about the longitudinal motion. For the Dutch roll, the roll and yaw angles can be used to observe the coupled lateral-directional response.

The oscillation period can be estimated from the time difference between equivalent peaks of the response. If more than one complete cycle is available, an average period can be calculated as

$$T = \frac{t_{n+k} - t_n}{k}, \tag{6.8}$$

where t_n is the time of a selected peak, t_{n+k} is the time of a later equivalent peak and k is the number of complete oscillation cycles between them. Using several cycles when available reduces the influence of small errors in identifying the exact position of a single peak.

The decrease in oscillation amplitude can be evaluated using the logarithmic decrement. Considering two peaks of the same sign separated by n complete cycles,

$$\delta = \frac{1}{n} \ln \left(\frac{x_0}{x_n} \right), \tag{6.9}$$

where x_0 is the amplitude of the first selected peak relative to the reference condition and x_n is the amplitude after n cycles. The corresponding damping ratio is then estimated as

$$\zeta = \frac{\delta}{\sqrt{4\pi^2 + \delta^2}}. \tag{6.10}$$

A larger value of δ therefore corresponds to an oscillation that loses amplitude more rapidly. When several usable peaks are available, the calculation can be repeated using different peak pairs to check the consistency of the estimated damping.

The half-amplitude time $t_{1/2}$ can also be obtained from the response as an additional check. It represents the time required for the oscillation amplitude to decrease to one half of its initial value. For the strongly damped Dutch-roll response, this quantity may be particularly useful if the oscillation becomes too small to identify several complete cycles.

Comparison with the Theoretical Predictions

The parameters obtained from the experimental response can finally be compared with the sea-level theoretical values presented in Section 2.2.2 and recalled in Section 6.3. Since the proposed first flight campaign would take place close to ground level, the sea-level predictions provide the appropriate reference for this comparison.

The relative difference between the experimental and theoretical oscillation period can be expressed as

$$\varepsilon_T = \frac{|T_{\text{exp}} - T_{\text{th}}|}{T_{\text{th}}} \times 100, \tag{6.11}$$

while the same approach can be applied to the damping ratio,

$$\varepsilon_\zeta = \frac{|\zeta_{\text{exp}} - \zeta_{\text{th}}|}{\zeta_{\text{th}}} \times 100. \tag{6.12}$$

The results of each test can then be summarized using a table such as Table 6.1. The experimental columns would be completed after the flight campaign.

Table 6.1: Proposed comparison between theoretical and experimental dynamic properties.

Mode	**Parameter**	**Theoretical**	**Experimental**	**Difference**
Phugoid	T [s]	12.405	–	–
	$t_{1/2}$ [s]	13.787	–	–
	ζ [-]	0.098	–	–
Dutch roll	T [s]	3.180	–	–
	$t_{1/2}$ [s]	0.349	–	–
	ζ [-]	0.707	–	–

For repeated tests, the parameters obtained from the individual manoeuvres should first be compared with each other before calculating a representative value. A similar result over several flights would provide more confidence that the measured behaviour belongs to the aircraft itself rather than to a particular pilot input or atmospheric disturbance.

The objective of this comparison is not to obtain a complete new aerodynamic model of the Space Dart, but to determine whether the main dynamic behaviour of the manufactured prototype agrees with the theoretical predictions. Significant differences between the two would indicate aspects that should be investigated through additional tests or a more detailed identification approach.

6.5 Limitations and Future Development

The methodology presented in this chapter provides a possible approach for the first flight tests of the Space Dart prototype, but several limitations should be considered before interpreting the results. Most of these are related to the fact that the complete flight campaign and some elements of the test setup could not be finalized within the time available for this thesis.

The first limitation concerns the release system. As discussed in Section 6.2, different solutions are still under evaluation and the final configuration has not yet been selected. Before starting the dynamic tests, the chosen mechanism should therefore be tested repeatedly to verify that the release is reliable and does not introduce an excessive

disturbance to the initial motion of the glider. Particular attention should also be given to any additional component installed on the Space Dart, since its mass and position could modify the centre of gravity.

The proposed release altitude of approximately 200–250 m should also be considered only as a preliminary practical estimate. A detailed altitude budget has not been calculated, and the actual required height will depend on the time needed to accelerate after release, establish the initial glide condition, perform the excitation, observe the free response and recover the aircraft safely. The first flights should therefore also be used to determine whether this altitude provides a sufficient margin for the complete test sequence.

Another limitation is associated with the available flight measurements. The current telemetry system provides the main quantities required to observe the aircraft motion, but it does not correspond to a dedicated flight-test instrumentation system. In particular, the recorded servo channels represent commanded inputs rather than direct measurements of the physical control-surface angles. A bench calibration can reduce this uncertainty by relating the recorded command to the corresponding surface deflection, but effects such as mechanical play or deformation during flight would not be measured directly.

The current logging frequency, approximately 10 Hz, should provide sufficient resolution for the relatively slow Phugoid motion. It is more limiting for the Dutch-roll response, which is predicted to have a period of approximately 3.2 s and to decay rapidly. For future tests, a higher recording frequency would therefore be useful if it can be obtained from the existing avionics or through additional instrumentation.

The mass properties also introduce some uncertainty in the comparison with the theoretical model. The complete manufactured prototype was weighed directly and has a measured mass of approximately 0.740 kg. However, the centre of gravity and moments of inertia reported in Section 3.5 were obtained from the CAD model and were not measured experimentally. The CAD configuration has a mass of approximately 0.720 kg, showing that some elements present on the real prototype are not fully represented in the model. A future test campaign would benefit from an experimental verification of the centre of gravity and, if required, of the main moments of inertia.

Finally, the proposed tests are intended to be performed at relatively low altitude and can therefore only be compared directly with the sea-level theoretical results. They cannot validate the dynamic behaviour predicted for the final operating condition at approximately 20 km. At this altitude, the atmospheric density is much lower and the theoretical analysis predicts significantly different dynamic characteristics, particularly

for the Phugoid and Dutch-roll modes. A future high-altitude campaign would therefore be necessary to verify the behaviour of the Space Dart under conditions representative of its intended stratospheric mission.

Despite these limitations, the proposed methodology provides a first practical way to compare the manufactured prototype with the available theoretical predictions. The results of these initial tests could then be used to refine the test procedure, improve the instrumentation where necessary and prepare the following stages of the Space Dart flight campaign.

The overall results obtained in this work, together with these remaining limitations and possible future developments, are summarized in the following chapter.

Chapter 7

Conclusions and Future Developments

This chapter summarizes the main results obtained during the development of the Space Dart prototype and the main limitations that remain at the end of the present work. The final section then discusses the next steps that could progressively bring the project closer to its intended stratospheric application.

7.1 Main Results

The main objective of this thesis was to transform the previously optimized aerodynamic configuration of the Space Dart into a complete physical prototype that could support the following experimental phase of the project.

Starting from the inherited geometry, the CAD model was substantially redesigned to accommodate the available avionics and the new control-surface arrangement. The internal architecture was reorganized to make better use of the limited available space, while keeping most of the existing electronic components. Particular attention was given to the position of the flight-control computer, battery, Pitot system, video equipment, telemetry system and servos.

The structure was also adapted to the practical requirements of additive manufacturing. The aircraft was divided into several components according to printer volume, printing orientation, assembly needs and accessibility of the internal systems. Different materials and printing strategies were selected for the fuselage, wings and moving control surfaces, and several printing iterations were required before obtaining reliable components.

The final prototype was then manufactured, assembled and integrated. The wing connections, fuselage closures, control-surface hinges and linkages were completed, and the avionics were installed in the positions defined during the CAD phase. Functional checks were carried out on the control surfaces and onboard systems, and short logging tests were also performed to verify that the available telemetry data were recorded correctly.

The completed prototype has a measured mass of approximately 0.740 kg. This value is slightly higher than the 0.720 kg obtained from the CAD model, mainly because some small assembly elements and wiring were not fully represented in the digital model.

The centre of gravity and inertia properties were instead estimated from the final CAD assembly.

The most important result of the work is therefore the realization of a complete and integrated Space Dart prototype. Although the vehicle has not yet completed a full flight-test campaign, it provides a physical platform from which the next development and validation activities of the project can begin.

A flight-test methodology was also proposed to support this next phase. The procedure focuses on the excitation and identification of the Phugoid and Dutch-roll modes, with the aim of comparing the measured dynamic response of the prototype with the theoretical predictions previously obtained for the final aerodynamic configuration.

7.2 Limitations of the Present Work

The work presented in this thesis also has several limitations that should be considered when evaluating the current state of the prototype.

The main limitation is that a complete flight-test campaign was not carried out within the available time. For this reason, the dynamic behaviour of the manufactured prototype has not yet been experimentally compared with the theoretical predictions. The methodology presented in Chapter 6 therefore remains a proposed procedure that still needs to be applied in practice.

Another open point concerns the release system. Different concepts were considered, including a drone-mounted commercial release mechanism and an onboard thermocutter, but the final solution has not yet been fully selected and validated. Since this system is necessary for the proposed carrier-drone test, its reliability and its effect on the aircraft mass distribution should be verified before the flight campaign.

The mass properties also contain some uncertainty. The total mass of the completed prototype was measured directly, but the center of gravity and the moments of inertia were obtained from the CAD model. An experimental verification of these quantities would improve the accuracy of any future comparison between measured and predicted dynamic behaviour.

No complete structural qualification was performed during this work. The design was developed through practical iterations, material selection and manufacturing experience, but the structure was not validated through a dedicated finite-element analysis or an experimental load-test campaign. The current prototype should therefore be considered a development model rather than a fully qualified flight vehicle.

The available instrumentation also introduces some limits to the proposed dynamic

tests. The current telemetry system records the main attitude, navigation and control information, but it is not a dedicated flight-test acquisition system. The sampling rate of approximately 10 Hz is suitable for observing slower motions such as the Phugoid, while it is more limiting for the faster Dutch-roll response. In addition, the recorded servo channels represent commanded inputs rather than direct measurements of the physical control-surface deflections.

Finally, the proposed first flight tests are intended to be performed at relatively low altitude. Their results can therefore only be compared directly with the sea-level theoretical predictions. They cannot provide a validation of the behaviour expected at the final stratospheric operating condition of approximately 20 km, where the atmospheric conditions and the predicted dynamic response are significantly different.

7.3 Future Developments

The next step in the development of the Space Dart should be the completion of the first flight-test campaign. Before this can be carried out, the release system should be finalized and tested repeatedly to verify that the separation from the carrier drone is reliable and does not introduce excessive disturbances to the initial motion of the glider.

The first low-altitude flights should then be used to verify the general controllability of the prototype, the effectiveness of the manual and stabilized flight modes and the reliability of the onboard communication and telemetry systems. Once these aspects have been confirmed, the Phugoid and Dutch-roll manoeuvres proposed in Chapter 6 could be performed and compared with the available theoretical predictions.

Further work could also improve the quality of the experimental data. The centre of gravity could be measured directly, and the main moments of inertia could be experimentally estimated if required. A higher telemetry sampling rate or additional recorded quantities could also improve the identification of the faster dynamic modes.

The recovery system represents another possible development. A parachute solution was considered during the design phase but was not integrated into the final prototype because of the limited internal space and the additional actuation and assembly complexity. A future configuration could reconsider this system, especially for higher-altitude tests where an independent recovery option could provide an additional level of safety.

The prototype itself will also likely require further iterations after the first flights. Manufacturing details, internal component positions, control linkages or structural connections may need to be modified depending on the behaviour observed during testing. In this sense, the current configuration should be considered an important

development step rather than the final version of the Space Dart.

In the longer term, the project could progressively move towards flights at higher altitude and conditions closer to the original stratospheric mission. Reaching this stage would require improvements in reliability, instrumentation, recovery strategy and possibly the control system, together with a better understanding of the behaviour of the vehicle under low-density atmospheric conditions.

The Space Dart is still at an early stage compared with the final concept originally imagined for the project, but the realization of a complete physical prototype makes the following steps more concrete. Future developments can now build on an actual vehicle rather than only on a theoretical configuration. With further testing and refinement, the project could gradually move from small-scale experimental flights towards the possibility of releasing and controlling the glider from the stratosphere, bringing the original idea of an interactive high-altitude flying platform closer to a real application.

Bibliography

[1] Thales Alenia Space, "Space business catalyst," https://www.thalesaleniaspace.com/it/lo-space-business-catalyst, accessed: Sep. 9, 2026.

[2] F. Ghinamo, "A micro glider for stratospheric flight: design, manufacturing and testing." Master's thesis, Politecnico di Torino, 2025, accessed: 2026-08-20.

[3] M. A. Tesi, "Definizione del database aerodinamico di un velivolo da rientro in scala," Master's thesis, Politecnico di Torino, 2026, accessed: 2026-08-20.

[4] OpenVSP, "Openvsp," https://openvsp.org/, accessed: Sep. 9, 2026.

[5] Siemens, "Simcenter star-ccm+," https://www.siemens.com/it-it/products/simcenter/fluids-thermal-simulation/star-ccm/, accessed: Sep. 9, 2026.

[6] SOLIDWORKS, "Solidworks," https://www.solidworks.com/, accessed: Sep. 9, 2026.

[7] Autodesk, "Autodesk fusion," https://www.autodesk.com/, accessed: Sep. 9, 2026.

[8] UltiMaker, "Fdm vs fff: Understanding 3d printing technologies," https://ultimaker.com/learn/fdm-vs-fff-understanding-3d-printing-technologies/, Feb. 2025, accessed: 2026-08-20.

[9] Snapmaker, "Anatomy of a 3d printer: The ultimate parts diagram and guide," https://www.snapmaker.com/blog/parts-of-3d-printer/, Apr. 2026, accessed: 2026-08-20.

[10] Bambu Lab, "Bambu lab wiki," https://wiki.bambulab.com/it/home, 2026, accessed: 2026-08-20.

[11] ——, "Pla aero," https://eu.store.bambulab.com/products/pla-aero, 2026, accessed: 2026-08-20.

[12] ——, "Studio settings for rc models," https://wiki.bambulab.com/en/knowledge-sharing/studio-settings-for-rc-models, 2024, accessed: 2026-08-20.

[13] R. V. Jategaonkar, *Flight Vehicle System Identification: A Time-Domain Methodology*, 2nd ed., ser. Progress in Astronautics and Aeronautics. American Institute of Aeronautics and Astronautics, 2015, vol. 245.

[14] INAV Flight, “Welcome to inav,” https://inavflight.github.io/docs/welcome/, accessed: Sep. 9, 2026.

[15] ——, “Blackbox,” https://inavflight.github.io/docs/core-features/blackblox/, accessed: Sep. 9, 2026.

[16] EdgeTX, “Sensor configuration options,” https://manual.edgetx.org/v2.10/color-radios/model-settings/telemetry/sensor-configuration-options, accessed: Sep. 9, 2026.

[17] RadioMaster, “Pocket radio quick start guide,” https://cdn.shopify.com/s/files/1/0701/8066/7584/files/Pocket_A1.8.pdf?v=1770617495, accessed: Sep. 9, 2026.

[18] EdgeTX, “Special functions,” https://manual.edgetx.org/color-radios/model-settings/special-functions, accessed: Sep. 9, 2026.

[19] ——, “Model settings,” https://manual.edgetx.org/color-radios/model-settings, accessed: Sep. 9, 2026.

Appendix A

Appendix A: Geometry details

Table A.1: Geometric parameters of the inherited V1 configuration and the final V1_4 aerodynamic configuration. Bold values indicate parameters modified with respect to V1.

Parameter	**V1**	**V1_4**
Wing		
Wingspan, b	0.688 m	0.688 m
Mean aerodynamic chord, MAC	0.199 m	0.199 m
Root chord, c_{root}	0.297 m	0.297 m
Tip chord, c_{tip}	0.021 m	0.021 m
Leading-edge sweep, Λ_{LE}	44.4°	**42.3°**
Trailing-edge sweep, Λ_{TE}	10°	**6°**
Dihedral, Γ	−6°	**+4°**
Twist, Θ	−6°	−6°
Airfoil	NACA 1207	NACA 1207
Vertical stabilizer		
Height, z_V	0.090 m	**0.080 m**
Root chord, $c_{V,\text{root}}$	0.200 m	**0.100 m**
Tip chord, $c_{V,\text{tip}}$	0.100 m	**0.040 m**
Leading-edge sweep, $\Lambda_{V,\text{LE}}$	48.0°	**53.1°**
Trailing-edge sweep, $\Lambda_{V,\text{TE}}$	0°	0°
Airfoil	NACA 0007	NACA 0007
Fuselage		
Length, L_{fus}	0.300 m	**0.345 m**
Maximum width, w_{max}	0.075 m	0.075 m
Maximum height, h_{max}	0.050 m	0.050 m
Rudder		
Spanwise extension	10–100% fin height	**15–100% fin height**
Root chord	0.070 m	**0.030 m**
Tip chord	0.070 m	**0.030 m**

Continued on next page

Table A.1 – continued

Parameter	**V1**	**V1_4**
Elevons		
Spanwise extension	10–80% half-span	**22.5–73% half-span**
Root chord	0.080 m	**0.047 m**
Tip chord	0.040 m	**0.0192 m**

Note: Some V1_4 dimensions were not explicitly restated in the previous aerodynamic thesis and were independently verified from the corresponding OpenVSP model and CAD geometry. In particular, the final fuselage length, wing leading-edge sweep and some control-surface dimensions were checked directly from the geometric models.

Appendix B

Appendix B: Slicer Settings

B.1 Wings

Table B.1: Additional slicer settings used for the wings

Parameter	Value	Default / Notes
FILAMENT		
Nozzle temperature	245°C	Always set to 245°C; other settings at default
COOLING		
Minimum fan speed threshold	80 s layer time	Default: 100 s
Maximum fan speed threshold	30% fan speed	Default: 100%
Auxiliary fan, first layer	20%	
SETTINGS OVERRIDES		
Nozzle length	0.2 mm	Enabled
Z hop when retract	0 mm	Enabled

Table B.2: Main slicer settings used for the wings

Parameter	**Value**	**Default / Notes**
QUALITY		
Layer height	0.20 mm	
Seam position	Nearest	Important
Slice gap closing radius	0 mm	
Avoid crossing walls	Enabled	Very important
STRENGTH		
Wall loops	2	
Sparse infill density	10%	
Sparse infill pattern	Gyroid	
SPEED		
Initial layer	50 mm/s	Default
Initial layer infill	50 mm/s	
Outer wall	50 mm/s	Default: 200 mm/s
Inner wall	100 mm/s	Default: 300 mm/s
Sparse infill	100 mm/s	Default: 270 mm/s
Internal solid infill	100 mm/s	Default: 250 mm/s
Top surface	50 mm/s	Default: 200 mm/s
Slow down for overhangs	Unchecked	
Travel speed	200 mm/s	Default: 500 mm/s
Normal printing acceleration	3000 mm/s^2	Default: 10000 mm/s^2
Travel acceleration	3000 mm/s^2	Default: 10000 mm/s^2
Initial layer travel acceleration	1000 mm/s^2	Default: 6000 mm/s^2
Outer wall acceleration	1000 mm/s^2	Default: 5000 mm/s^2
Slow down by height	Unchecked	
SUPPORT		
Supports	Enabled	
Type	Tree (Auto)	
Style	Default	
Threshold angle	30°	
Remove small overhangs	Active	
OTHERS		
Brim type	Outer brim only	
Brim width	5 mm	
Slicing mode	Even-odd	

B.2 Top Back Fuselage

Table B.3: Main slicer settings used for the fuselage top back

Parameter	Value	Default / Notes
QUALITY		
Layer height	0.20 mm	All other quality settings at default
STRENGTH		
Wall loops	3	
Sparse infill density	30%	
Sparse infill pattern	Grid	
SPEED		
Initial layer	50 mm/s	Default
Initial layer infill	105 mm/s	Default
Outer wall	150 mm/s	Default: 200 mm/s
Inner wall	250 mm/s	Default: 300 mm/s
Sparse infill	250 mm/s	Default: 270 mm/s
Slow down for overhangs	Active	
Slow down by height	Active	Very important
Starting height	15 mm	
Speed at starting height	150 mm/s	
Ending height	300 mm	
Speed at ending height	80 mm/s	
SUPPORT		
Supports	Enabled	
Type	Tree (Manual)	
Style	Tree Slim	
Threshold angle	45°	
On build plate only	Unchecked	Important
Remove small overhangs	Active	
Branch distance	10 mm	Default: 5 mm
OTHERS		
Brim type	Outer brim only	
Brim width	10 mm	
Brim-object gap	0.07 mm	Default: 0.10 mm

B.3 Top Front Fuselage

Table B.4: Main slicer settings used for the fuselage top front

Parameter	Value	Default / Notes
QUALITY		
Layer height	0.20 mm	All other quality settings at default
STRENGTH		
Wall loops	3	
Sparse infill density	30%	
Sparse infill pattern	Gyroid	
SPEED		
Initial layer	50 mm/s	Default
Initial layer infill	105 mm/s	Default
Outer wall	150 mm/s	Default: 200 mm/s
Inner wall	250 mm/s	Default: 300 mm/s
Sparse infill	250 mm/s	Default: 270 mm/s
Slow down for overhangs	Active	
Slow down by height	Active	Very important
Starting height	15 mm	
Speed at starting height	150 mm/s	
Ending height	200 mm	
Speed at ending height	40 mm/s	
SUPPORT		
Supports	Enabled	
Type	Tree (Auto)	
Style	Default	
Threshold angle	30°	
Remove small overhangs	Active	
Top Z distance	0.17 mm	Default: 0.20 mm
OTHERS		
Brim type	Outer brim only	
Brim width	15 mm	
Brim-object gap	0.07 mm	Default: 0.10 mm

B.4 Bottom Back Fuselage

Table B.5: Main slicer settings used for the fuselage bottom back

Parameter	Value	Default / Notes
QUALITY		
Layer height	0.20 mm	All other quality settings at default
STRENGTH		
Wall loops	3	
Sparse infill density	30%	
Sparse infill pattern	Grid	
SPEED		
Initial layer	50 mm/s	Default
Initial layer infill	105 mm/s	Default
Outer wall	150 mm/s	Default: 200 mm/s
Inner wall	250 mm/s	Default: 300 mm/s
Sparse infill	250 mm/s	Default: 270 mm/s
Slow down for overhangs	Active	
Slow down by height	Active	Very important
Starting height	15 mm	
Speed at starting height	150 mm/s	
Ending height	300 mm	
Speed at ending height	80 mm/s	
SUPPORT		
Supports	Enabled	
Type	Tree (Manual)	
Style	Tree Slim	
Threshold angle	45°	
On build plate only	Unchecked	Important
Remove small overhangs	Active	
Branch distance	10 mm	Default: 5 mm
OTHERS		
Brim type	Outer brim only	
Brim width	15 mm	
Brim-object gap	0.07 mm	Default: 0.10 mm

B.5 Bottom Left/Right Fuselage

Table B.6: Main slicer settings used for the fuselage bottom left and right

Parameter	Value	Default / Notes
QUALITY		
Layer height	0.20 mm	All other quality settings at default
STRENGTH		
Wall loops	3	
Sparse infill density	30%	
Sparse infill pattern	Grid	
SPEED		
Initial layer	50 mm/s	Default
Initial layer infill	105 mm/s	Default
SUPPORT		
Supports	Enabled	
Type	Tree (Manual)	
Style	Tree Slim	
Threshold angle	45°	
On build plate only	Unchecked	Important
Remove small overhangs	Active	
Branch distance	10 mm	Default: 5 mm
OTHERS		
Brim type	Outer brim only	
Brim width	15 mm	
Brim-object gap	0.07 mm	Default: 0.10 mm

B.6 Moving Control Surfaces

Table B.7: Main slicer settings used for the elevons and rudder

Parameter	Value	Default / Notes
QUALITY		
Layer height	0.20 mm	All other quality settings at default
STRENGTH		
Wall loops	2	Default
Sparse infill density	10%	
Sparse infill pattern	Gyroid	
SPEED		
Initial layer	50 mm/s	Default
Initial layer infill	105 mm/s	Default
Outer wall	150 mm/s	Default: 200 mm/s
Inner wall	250 mm/s	Default: 300 mm/s
Sparse infill	250 mm/s	Default: 270 mm/s
Slow down for overhangs	Active	
Slow down by height	Active	Very important
Starting height	15 mm	
Speed at starting height	150 mm/s	
Ending height	300 mm	
Speed at ending height	80 mm/s	
SUPPORT		
Supports	Enabled	
Type	Tree (Auto)	
Style	Default	
Threshold angle	30°	
Remove small overhangs	Active	
Top Z distance	0.17 mm	Default: 0.20 mm
OTHERS		
Brim type	Outer brim only	
Brim width	10 mm	
Brim-object gap	0.07 mm	Default: 0.10 mm